

AD-A199 693

# METHOD FOR LONG TERM IONIZING RADIATION DAMAGE PREDICTIONS FOR THE SPACE ENVIRONMENT

R. J. Maier

August 1988

Final Report

Approved for public release; distribution unlimited.



DTIC  
 ELECTE  
 SEP 26 1988  
 S E D

AIR FORCE WEAPONS LABORATORY  
 Air Force Systems Command  
 Kirtland Air Force Base, NM 87117-6008

UNCLASSIFIED

SECURITY CLASSIFICATION OF THIS PAGE

ADA199693

REPORT DOCUMENTATION PAGE				Form Approved OMB No 0704-0188	
1a. REPORT SECURITY CLASSIFICATION UNCLASSIFIED			1b. RESTRICTIVE MARKINGS		
2a. SECURITY CLASSIFICATION AUTHORITY			3. DISTRIBUTION / AVAILABILITY OF REPORT Approved for public release; distribution unlimited.		
2b. DECLASSIFICATION / DOWNGRADING SCHEDULE					
4. PERFORMING ORGANIZATION REPORT NUMBER(S) AFWL-TR-87-136			5. MONITORING ORGANIZATION REPORT NUMBER(S)		
6a. NAME OF PERFORMING ORGANIZATION Air Force Weapons Laboratory		6b. OFFICE SYMBOL (If applicable) NTCT	7a. NAME OF MONITORING ORGANIZATION		
6c. ADDRESS (City, State, and ZIP Code) Kirtland Air Force Base, NM 87117-6008			7b. ADDRESS (City, State, and ZIP Code)		
8a. NAME OF FUNDING / SPONSORING ORGANIZATION		8b. OFFICE SYMBOL (If applicable)	9. PROCUREMENT INSTRUMENT IDENTIFICATION NUMBER		
8c. ADDRESS (City, State, and ZIP Code)			10. SOURCE OF FUNDING NUMBERS		
		PROGRAM ELEMENT NO 62601F	PROJECT NO 8809	TASK NO 11	WORK UNIT ACCESSION NO 50
11. TITLE (Include Security Classification) METHOD FOR LONG TERM IONIZING RADIATION DAMAGE PREDICTIONS FOR THE SPACE ENVIRONMENT					
12. PERSONAL AUTHOR(S) Maier, R.J.					
13a. TYPE OF REPORT Final		13b. TIME COVERED FROM Nov82 to Dec87		14. DATE OF REPORT (Year, Month, Day) 1988 August	15. PAGE COUNT 112
16. SUPPLEMENTARY NOTATION Dissertation					
17. COSATI CODES			18. SUBJECT TERMS (Continue on reverse if necessary and identify by block number)		
FIELD	GROUP	SUB-GROUP	Microelectronics	Oxide charge	
06	07		Radiation effects	Surface effects	
09	01		Hardness assurance	Total dose effects	
19. ABSTRACT (Continue on reverse if necessary and identify by block number)					
<p>The objective of the work is to predict the total dose damage from low level ionizing radiation sources for very long (5 years) exposure times. A prior effort to extrapolate annealing data to long times used linear systems theory or the convolution integral. Problems with the linear systems theory approach are: the damage is assumed to be linear even though the experimental data show a saturation effect; the annealing function, which is to be combined with the dose rate, needs to be known for a very long length of time (i.e., a 5-year observation of the annealing); and to do the integral numerically using data requires large amounts of computation. <i>K</i></p> <p>In this work, the total dose damage prediction is divided into separate predictions of positive bulk charges and of interface-states. These predictions are then to be combined. As a first approximation, interface-states are assumed to not anneal and are not further dealt with. In the prediction of positive charge, the nonlinear problem is treated by (over)</p>					
20. DISTRIBUTION / AVAILABILITY OF ABSTRACT <input checked="" type="checkbox"/> UNCLASSIFIED/UNLIMITED <input type="checkbox"/> SAME AS RPT <input type="checkbox"/> DTIC USERS			21. ABSTRACT SECURITY CLASSIFICATION UNCLASSIFIED		
22a. NAME OF RESPONSIBLE INDIVIDUAL R.J. MAIER			22b. TELEPHONE (Include Area Code) (505) 844-9901	22c. OFFICE SYMBOL NTCT	

DD Form 1473, JUN 86

Previous editions are obsolete.

SECURITY CLASSIFICATION OF THIS PAGE

UNCLASSIFIED

including the nonlinearity in the description of each trap. Since this is an electrostatic effect, the traps can be summed assuming superposition. Specifically, each filled trap experiences a constant probability per unit time of detrapping. This will obey an exponential decay law (as in radioactive decay).

To superimpose the fields from each trap, the distribution function for the detrapping rates is multiplied by the exponential and integrated over detrapping rates. This turns out to be the Laplace transform formula. Using the inverse transform on the annealing curve, we can get the distribution function. We predict the long term damage from a low level source by multiplying the distribution function by the response of the individual traps to the radiation and integrating.

In short, a method is constructed which allows predictions of the result of long term irradiations by including detailed knowledge about the trap and its nonlinear saturation. Finally, an algorithm is presented for converting the extrapolated short-term annealing data to the long term prediction which avoids a lengthy numerical convolution integral.

The remainder of the paper is devoted to explaining the error that will be suffered if the traps with decay times long compared to experimental time should follow an unexpected distribution. This is shown to result in a small yet conservative error.

TABLE OF CONTENTS

<u>Chapter</u>	<u>Page</u>
1.0 INTRODUCTION .....	1
1.1 THE PROBLEM .....	1
1.2 COMPLEX CIRCUIT TESTING .....	2
1.3 BACKGROUND .....	-
1.4 APPROACH .....	-
2.0 MATHEMATICAL METHODS .....	12
2.1 CURIE-VON-SCHWEIDLER LAW .....	12
2.2 EXTRAPOLATION ALGORITHM .....	15
3.0 PHYSICAL MODEL .....	27
3.1 INTRODUCTION TO PHYSICAL MODEL .....	27
3.2 ONE-DIMENSIONAL MODEL .....	29
3.3 SPHERICAL WELL MODEL .....	35
3.4 PHYSICAL MODEL SUMMARY .....	43
4.0 CONCLUSIONS .....	45
APPENDIX: INTEGRATION DETAILS .....	46
REFERENCES .....	99

Accession For	
NTIS GRA&I	<input checked="" type="checkbox"/>
DTIC TAB	<input type="checkbox"/>
Unannounced	<input type="checkbox"/>
Justification	
By _____	
Distribution/	
Availability Codes	
Dist	Avail and/or Special
A-1	



LIST OF FIGURES

<u>Figure</u>	<u>Page</u>
1. The incomplete gamma function, along with the associated inverse power function. ....	49
2. Simulate Co <sup>60</sup> Irradiation for $\alpha=0.1$ . ....	50
3. Simulate Co <sup>60</sup> Irradiation for $\alpha=0.25$ . ....	51
4. Simulate Co <sup>60</sup> Irradiation for $\alpha=0.5$ . ....	52
5. The error from nonannealing traps for $\alpha=0.1$ . ....	53
6. The error from nonannealing traps for $\alpha=0.25$ . ....	54
7. The error from nonannealing traps for $\alpha=0.5$ . ....	55
8. The error from extrapolating a curve with error from nonannealing traps for $\alpha=0.1$ . ....	56
9. The error from extrapolating a curve with error from nonannealing traps for $\alpha=0.25$ . ....	57
10. The error from extrapolating a curve with error from nonannealing traps for $\alpha=0.5$ . ....	58
11. The error from a trap distribution with a floor for $\alpha=0.1$ and $\kappa=1E-7$ . ....	59
12. The error from a trap distribution with a floor for $\alpha=0.25$ and $\kappa=1E-7$ . ....	60
13. The error from a trap distribution with a floor for $\alpha=0.25$ and $\kappa=1E-7$ . ....	61
14. The extrapolation error caused by a trap distribution with a floor for $\alpha=0.1$ and $\kappa=1E-7$ . ....	62
15. The extrapolation error caused by a trap distribution with a floor for $\alpha=0.25$ and $\kappa=1E-7$ . ....	63
16. The extrapolation error caused by a trap distribution with a floor for $\alpha=0.5$ and $\kappa=1E-7$ . ....	64
17. The extrapolation error caused by a trap distribution with a floor for $\alpha=0.1$ and $\kappa=1E-6$ . ....	65
18. The extrapolation error caused by a trap distribution with a floor for $\alpha=0.25$ and $\kappa=1E-6$ . ....	66
19. The extrapolation error caused by a trap distribution with a floor for $\alpha=0.5$ and $\kappa=1E-6$ . ....	67
20. The energy distributions of the traps. ....	68

<u>Figure</u>	<u>Page</u>
21. An energy level diagram showing the traps and their detrapping paths .....	69
22. The tunneling barrier profile for the one-dimensional tunneling model .....	70
23. Partial detrapping rates; shown are partial rates from the ground state (solid line), the partial rates from the excited states are identified by temperature. The levels on the right correspond to the partial detrapping by thermal emission with cross sections $1E-16$ and $7E-14$ , respectively. Trapping energy is $1.15$ eV and electric field of $1E6$ V/cm. ....	71
24. Partial detrapping rates; shown are partial rates from the ground state (solid line), the partial rates from the excited states are identified by temperature. The levels on the right correspond to the partial detrapping by thermal emission with cross sections $1E-16$ and $7E-14$ , respectively. Trapping energy is $1.75$ eV and electric field of $4E6$ V/cm. ....	72
25. The energy distributions of the traps, on a log scale. ....	73
26. A comparison between the data from Schwank (Ref. 5) and computations using the 1D model, made for a trap depth parameter of $1E7$ $cm^{-1}$ , using trap energy distribution #3, and temperature $375$ K vs. $100^{\circ}C$ . ....	74
27. A comparison between the data from Schwank (Ref. 5) and computations using the 1D model, made for a trap depth parameter of $1E7$ $l/cm$ , using trap energy distribution #1, and temperature $375$ K vs. $100^{\circ}C$ . ....	75
28. A comparison between the data from Schwank (Ref. 5) and computations using the 1D model, made for a trap depth parameter of $2E6$ $l/cm$ , using trap energy distribution #3, and temperature $375$ K vs. $100^{\circ}C$ . ....	76
29. A comparison between the data from Schwank (Ref. 5) and computations using the 1D model, made for a trap depth parameter of $1E7$ $l/cm$ , using trap energy distribution #3, and an electric field of $2E6$ V/cm vs. $10$ volts across $450$ Å. ....	77
30. Additional data from Schwank (Ref. 23) adding annealing curves for $10V$ at $125^{\circ}C$ and $20$ V at $100^{\circ}C$ .....	78
31. A comparison between the data from Schwank (Ref. 5) and computations using the 1D model, made for a trap depth parameter of $1E7$ $cm^{-1}$ , using trap energy distribution #2, and temperature $375$ K vs. $100^{\circ}C$ . ....	79
32. A comparison between the data from Schwank (Ref. 5) and computations using the 1D model, made for a trap depth parameter of $1E7$ $l/cm$ , using trap energy distribution #2, and an electric	

	field of 2E6 V/cm vs. 10 volts across 450 Å. ....	80
33.	The tunneling barrier energy, for a trap energy of 2 eV, for the spherical well model with vertical lines at 2, 4 and 8 Å to show the beginning of the barrier. ....	81
34.	The tunneling barrier energy, for a trap energy of 0.8 eV. for the spherical well model with vertical lines at 2, 4 and 8 Å to show the beginning of the barrier. ....	82
35.	A comparison between the data from Schwank (Ref. 5) and computations using the spherical well model, radius 2 Å and cross section 1E-16, made for a trap depth parameter of 2E6 cm <sup>-1</sup> , using trap energy distribution #3, and temperature 375 K vs. 100°C. ....	83
36.	A comparison between the data from Schwank (Ref. 5) and computations using the spherical well model, radius 2 Å and cross section 1E-16, model, made for a trap depth parameter of 1E7 cm <sup>-1</sup> , using trap energy distribution #2, and an electric field of 2E6 V/cm vs. 10 volts across 450 Å. ....	84
37.	Partial detrapping rates for zero field. ....	85
38.	Partial detrapping rates for 2.5 V across 450 Å. ....	86
39.	Partial detrapping rates for 5 V across 450 Å. ....	87
40.	Partial detrapping rates for 7.5 V across 450 Å. ....	88
41.	Partial detrapping rates for 10 V across 450 Å. ....	89
42.	Detrapping rates for 10 V across 450 Å at 275 K. ....	90
43.	Detrapping rates for 10 V across 450 Å at 375 K. ....	91
44.	Detrapping rates for 20 V across 450 Å. ....	92
45.	The energy distributions of the traps, on a log scale. ....	93
46.	Spherical well annealing curves for: tunneling depth parameters, 2E6, 4.5E6 and 1E7, the five trap energy distributions, 10 V across 450 Å, and 375 K. ....	94
47.	Spherical well annealing curves for: tunneling depth parameters, 2E6, 4.5E6 and 1E7, the five trap energy distributions, 20 V across 450 Å, and 375 K. ....	95
48.	Spherical well annealing curves for: tunneling depth parameters, 2E6, 4.5E6 and 1E7, the five trap energy distributions, 20 V across 450 Å, and 375 K but at radius 2 Å and capture cross section 1E-16. ....	96

Figure

Page

49. A comparison between the data from Schwank (Ref. 5) and computations using the spherical well model, radius 8 Å and cross section  $7E-14$ , made for a trap depth parameter of  $1E7 \text{ cm}^{-1}$ , using trap energy distribution #5, and temperature 375 K vs.  $100^{\circ}\text{C}$ . . . . . 97
50. A comparison between the data from Schwank (Ref. 5) and computations using the spherical well model, radius 2 Å and cross section  $1E-16$ , model, made for a trap depth parameter of  $1E7 \text{ cm}^{-1}$ , using trap energy distribution #5, and an electric field of 10 volts across 450 Å. . . . . 99

CHAPTER 1.  
INTRODUCTION

1.1 THE PROBLEM

Ionizing radiation produces changes in the surface properties of semiconductor devices. In silicon devices, ionization introduces interface-states and bulk charges into the oxide passivation layer. These and other device phenomena cause parameter\* changes in transistors which will cause failure in complex circuits. The system designer's problem is to select circuits which can survive the expected ionizing environment. Selection of such circuits requires a data base of radiation failure levels for a catalogue of circuits. Currently, radiation failure levels are established by short (one hour) exposures of the circuits in question. However, following exposure the parameters anneal and do not remain stable. In the case of circuits used in a long-term ionizing environment such as a five-year space mission, appreciable annealing occurs during exposure and failure occurs at a higher (maybe much higher) radiation level than it did for the shorter exposure used to select the circuit. Failure to allow for this annealing may result in a much more expensive design, with perhaps less performance. Performing five-year experiments is impractical. Methods of accelerating the annealing can not be trusted because it is known that annealing involves both quantum mechanical tunneling (which is accelerated by voltage) and thermal emission (which is accelerated by increasing the temperature), and there is no way of

---

\* These parameters are commonly the threshold voltage and channel mobility of real and parasitic transistors.

accelerating both by the same amount. Predicting parameter changes during exposures of a year or longer, from much shorter (one week) experiments is the subject area of this paper.

A second difficulty is circuit complexity. If we were to expose a complex circuit to a short burst of radiation, and the circuit were to fail and recover later, we would expect that if the same radiation dose were delivered slowly the circuit would not fail. However, an acceptable method to restore the irradiated circuit to its original condition is not available. This prevents the above test from being used as a hardness assurance screen. A method is needed to perform the testing required to assure the hardness without destructively testing needed parts. The method proposed is a variant of lot sample testing.

## 1.2 COMPLEX CIRCUIT TESTING

First, where does the proposed method fit in to the overall problem of assuring the hardness of complex circuits? Assume that some form of lot sample testing will be necessary. In lot sample testing, the more uniform the production lot from which a sample is to be drawn, the more successful will be the quality control which results from the testing of that sample. The greatest uniformity is achieved when all the parts are from a single wafer. Less uniformity is gained from a single diffusion batch. However, a modern VLSI<sup>\*</sup> wafer may only yield a few parts and new production methods are being introduced which process only one wafer at a

---

\* Very Large Scale Integration

time. Thus, straight forward lot sampling becomes limited as a hardness assurance technique. Instead, consider the use of test transistors that are normally included on each chip to represent the circuit. Then the test transistors that were on the inked chips (those that failed wafer probe) could be bonded up as breakouts. If measurements from these transistors could be related to circuit failure a very effective method of monitoring the hardness quality of a processing line could be instituted.

The parameter changes which will cause circuit failure must be determined by experiment. For complex circuits, parameter changes which cause circuit failure are measured by subjecting the circuit along with representative test devices to the stresses of an ionizing radiation environment. The test devices are made to be representative by arranging that they be from the same die or the same wafer or at least in the same diffusion lot. To make sure that the ionizing radiation environment will simulate the parameter changes produced by exposure to a long term environment, both a short (one hour) exposure and a moderately long (one week) annealing period are used. This stress will assure that the transistors and other devices, both real and parasitic, which are in the circuit will be swept through a combination of parameter changes which include those that would occur during a long exposure. The parameter changes which are occurring in the circuit devices are tracked by the parameter changes in the nearly identical test devices and can thereby be accurately estimated. Generally, the failure modes are: an N-channel transistor goes depletion mode causing unacceptable leakage, the threshold voltages of either the N-channel or the P-channel transistor or both increase causing speed loss, an increase in mobility also causes speed

loss, and an inversion under the field oxide produces a leakage path. A minimum of an N-channel and a P-channel gate oxide transistor, and an N-channel field oxide transistor are needed to measure the oxide changes which cause the above set of failure modes. In any case, test devices are needed that will separate the causes of the parameter changes into interface states and bulk charge.\* Then a method is needed for converting short term data into a long term prediction of interface states and bulk charge. Finally, for example, the sum of the predicted unannealed interface states and bulk charges times the electronic charge ( $e$ ) and the capacitance (per unit area) gives the predicted threshold voltage shift.

This work assumes that the above sampling technique or something similar will work. To assure the hardness of a particular circuit component, the prediction of the bulk charge must be combined with the prediction of the interface states to give predictions of parameter changes. The piece of the problem addressed by this paper is to find a method for making the long term prediction of the bulk charge annealing. At this time it is best to assume that interface states do not anneal.

### 1.3 BACKGROUND

At the 1972 IEEE Conference on Nuclear and Space Radiation Effects (Refs. 1 and 2) two models for the rapid annealing of total dose effects were presented. Both models assumed hole traps at the interface. However, one model assumed thermally activated detrapping and the other

---

\*Currently the subthreshold method, sometimes along with the charge pumping method, is used for this separation.

model assumed quantum mechanical (QM) tunneling of the hole from the trap to the silicon valence band. A few years later (Refs. 3 and 4), it was shown that the early rapid annealing was due to dispersive transport of the holes from the bulk of the oxide to the interface. The earlier two models are now candidates for the long term annealing which has been observed. Experimentally, the annealing is dependent on both temperature and applied electric field (Ref. 5). A qualitative explanation requires both the QM tunneling and the thermal emission mechanisms.

The Curie-von-Schweidler law, which is an inverse fractional power of time, is a mathematical form which commonly appears in other models. The model of the dispersive transport (Refs. 6 and 7) which actually explains the rapid annealing in  $\text{SiO}_2$ , gives this asymptotically. Jonscher (Ref. 8) has shown that this form describes the relaxation of dipoles in dielectrics. It has been shown (Refs. 9 and 10), that 'Long-Time Tails' which occur in strongly chaotic systems, give this form. Examined here is a particular mathematical model which gives inverse time to a fractional power dependence description of the annealing of bulk charge.

QM tunneling and thermal emission are the known mechanisms for the release of the trapped hole. The applied bias lowers the tunneling barrier in one direction and lowers the thermal activation energy. Two models were explored; a one-dimensional (1D) model and a spherical well model. These models were computationally very complex. The models require input data consisting of; (1) the distribution of traps as a function of the distance from the interface, (2) the distribution in energy of the hole binding energy, and (3) a hole capture cross section  $\sigma$ .

needed to calculate release by thermal emission. In addition, the one-dimensional model requires a constant, which is the frequency of tunneling attempts with which to multiply the tunneling probability to get the detrapping rate, and an excitation energy for the first excited state. The assumptions made were: (1) an exponential distribution of the trap distance from the interface, with a  $1/e$  constant of  $10\text{-}50\text{\AA}$ ; (2) a capture cross section of  $10^{-16}\text{ cm}^2$ , which was estimated using the observed  $10^{-15}\text{-}10^{-17}$  range for neutral capture cross sections in silicon; (3) the frequency constant for the one-dimensional model to be  $10^{15.5}$  which was estimated using  $\Delta E=1\text{ eV}$  in the uncertainty principle  $\Delta E\Delta t \geq \hbar$ ; and (4) the distribution of binding energies was obtained from thermal activation energies published by Denchenko (Ref. 11). Neither model proved successful in predicting annealing curves with the above assumed input data. The predicted annealing was faster than the experimental data from Schwank (Ref. 5). Successful prediction required smaller values for the capture cross section and the tunneling attempt frequency constant. Adjusting the binding energy distribution makes it possible to fit any analytical curve. What is needed is a physical model which is inflexible and cannot be distorted enough to cause unreal extrapolations. Instead, the physical model must be used to understand the limits on the shape of the curves.

Interface states must be observed during the annealing of the irradiated test transistors. Schwank (Ref. 5) observed no annealing of interface states in the devices he tested, but this may not always be the case.) In the no annealing case, the interface contribution to each parameter is kept constant. Where the interface states do anneal the

mathematical algorithm can be used. However, the risk of using it has not been evaluated.

#### 1.4 APPROACH

A prior effort to extrapolate annealing data to long times used linear systems theory, i.e., the convolution integral (Refs. 12 and 13):

$$V_{th}(t) = \int_0^t D'(t-\tau)V_{th}^0(\tau) d\tau \quad (1)$$

where:  $V_{th}(t)$  is the threshold voltage shift as a function of time  
 $D'(t)$  is the dose rate as a function of time, and  
 $V_{th}^0(t)$  is the threshold voltage shift annealing curve resulting from a unit impulse of dose

The problems with this approach are: (1) that  $V_{th}$  (the threshold voltage) is assumed to be linear with dose even though it is known to have a saturation effect; (2) that the function  $V_{th}^0(\tau)$  needs to be known for the length of time desired for  $V_{th}(t)$ ; and (3) that, particularly if  $V_{th}^0(\tau)$  is experimental, the algorithm for converting  $V_{th}^0(t)$  measurements to predictions  $V_{th}(t)$  requires large amounts of computation. (The numerical convolution integral has a high number of floating point instructions).

In this work, the nonlinear problem is avoided by treating each trap separately and including the nonlinearity (which is a saturation effect) in the treatment of each trap. Because the  $V_{th}$  shift is caused by the electrostatic field from trapped charges, the traps can be added together

because of a superposition principle. Specifically, each filled trap experiences a constant probability (R) per unit time of detrapping. This will result in an exponential decay law for that trap (as in radioactive decay). Mathematically, the number of filled traps is given by

$$\frac{dn_0^+(R, t)}{dt} = -Rn_0^+(R, t) \quad (2)$$

Which has solution

$$n_0^+(R, t) = n(R)e^{-Rt} \quad (3)$$

Each trap is labeled by its detrapping rate R and the number of such traps is  $n(R)dR$ . The value of the function  $n(R)$ , the total number of traps, serves as the arbitrary constant in this differential equation solution. If there is a source of holes (a flux of holes produced by the absorption of ionizing radiation), to be trapped by the empty traps,  $n^0(R, t)$ , then:

$$\frac{dn^+(R, t)}{dt} = H[n^0(R, t)] - R[n^+(R, t)] \quad (4)$$

where H is the rate of hole trapping by empty traps, and empty and full traps must add up to total traps.

$$n^0(R, t) + n^+(R, t) = n(R)$$

For  $n^+(R, 0) = 0$ , i.e., the Cauchy problem, the solution is then

$$n^+(R, t) = n(R) [H/(H+R)] [1 - e^{-(H+R)t}] \quad (5)$$

Because the hole flux will be the same for all traps\* and because the cross section for hole capture will be largely determined by the physical size of the trap (neutral) and, therefore, will be numerically near the same value for all traps# (Ref. 14), H is to be the same for all traps. The effects of the traps are superimposed by integrating

$$N^+(t) = \int_0^\infty n(R) [H/(R+H)] [1 - e^{-(H+R)t}] dR \quad (6)$$

and for H=0 for all traps initially filled it reduces to

$$N_0^+(t) = \int_0^\infty n(R) e^{-Rt} dR \quad (7)$$

Notice for H=0, the integral is the same as the Laplace transform. If  $N_0^+(t)$  is measured for the H=0 case; and some functional form  $F(C_k, t)$  is fitted by least squares to those measurements, to determine the parameters  $C_k$ ;  $n(R)$  can then be found from the inverse Laplace transform  $L^{-1}F(C_k, t)$ . Now having an approximation for  $n(R)$ , the integral for H≠0 can be

---

\* Actually most of the holes are created in the bulk and pass through the trap layer on the way to the interface. The traps are in a layer within 100 Å of the interface. The flux of holes which pass through the traps which are closer to the interface is somewhat reduced but since in hardened oxides 95% of the holes pass through the entire layer this will be neglected.

# Most of the traps are known, from electron spin resonance experiments, to have the same structure, called the E' center.

○ n stands for the number of traps. N will be capitalized when N is the result of an integral over R.

performed and this will yield an estimate for  $N^+(t)$  for the long term irradiation case. In particular, let

$$F(C_k, t) = \frac{1}{t^\alpha} \sum_{k=0}^m \frac{C_k}{t^k} \quad (8)$$

a truncated modified Laurent expansion, be least squares fitted to the experimental  $N_0^+(t)$ , obtaining a set of parameters  $C_k$ .

$$n(R) = L^{-1}[N^+(t)] = R^{\alpha-1} \sum_0^m \frac{C_k}{\Gamma(k+\alpha)} R^k \quad (9)$$

is placed in the integral for  $H \neq 0$ , the result will be a series of incomplete Gamma functions.

$$N^+(t) = \sum_0^m C_k H^{(k+\alpha)} \gamma(1-k-\alpha, Ht) \quad (10)$$

If there was a known functional form for  $n(R)$  with only a few adjustable parameters, the problem would be solved. The mathematics for converting  $n(R)$  to  $N^+(t)$  is in Equation 6. The problem is that without annealing data out to five years, assurance that a theoretical form is correct is difficult. The needed theoretical form has some necessary characteristics. In addition to fitting the experimental data, it must have very few adjustable parameters. This is because forms like Equation 8, given enough  $C_k$ 's, will fit a wide variety of data curves but when the form is plotted beyond the range of the data, extrapolating, the curve

will shoot off in most any direction. If the fit is to be used to extrapolate, it must be simple, like a straight line. The form  $N_0/t^\alpha$  has two adjustable parameters and it is a straight line on log-log paper. When radiation is present, a third parameter  $H$  is needed to put the irradiation rate into the form. In this paper, the form  $N_0/t^\alpha$ , the Curie-von-Schweidler law, (Ref. 8) is assumed to be the correct form and that extrapolation with this form will be in the right direction. Much of the paper is devoted to showing that this form must closely approximate the real annealing curve. The other assumptions are the exponential decay law and the proportionality of  $H$  to the irradiation rate  $\dot{\gamma}$ . The exponential decay law is not really an assumption as it is the unavoidable consequence of the probability interpretation of quantum mechanics as it is in radioactive decay.

This approach allows us to include specific knowledge<sup>\*</sup> about the trap in a model to predict the result of long term irradiations. The nonlinear saturation is included. Also included is a method of extrapolating the annealing curve so that long term predictions can be obtained from shorter term annealing curves. Finally, the approach gives an algorithm for converting the extrapolated annealing data to the long term prediction which doesn't involve a lengthy numerical convolution integral.

---

\* Summarized in the number of traps which have the anneal rate  $R$ ,  $n(R)$

CHAPTER 2.  
MATHEMATICAL METHODS

2.1 CURIE-VON-SCHWEIDLER LAW

The introduction showed that a Curie-von Schweidler law results from commonly occurring material conditions. These conditions are: an exponential decay law (as in radioactive decay); and a power law distribution of decay rates. Specifically; rewriting Equation (3) in terms of a variable  $x$  that  $R$  is dependent on,

$$n^+(x,t) = n(x,0)e^{-R(x)t} \quad (11)$$

and when a distribution of decay rates is introduced the function which describes the time dependence of the remaining undecayed states is given by Equation 7 which is here rewritten for convenience.

$$N(t) = \int_0^{\infty} n(R)e^{-Rt} dR \quad (7)$$

where:  $n(R)dR$  is the number of sites with decay rate  $R$  in the interval  $dR$ .

This is the Laplace transform. Any Laplace transform pair could be used here even a discrete numerical transform could be used. However, the Laplace transform pair of interest here is;

$$N(t) = N_0/t^\alpha \quad (12a) \quad \text{if } n(R) = N_0R^{\alpha-1}/\Gamma(\alpha) \quad (12b)$$

If  $n(R)$  is to be a distribution, it must be integrable. To make the above power law,  $R^{\alpha-1}$ , integrable (it goes to  $\infty$  as  $R$  goes to  $\infty$ ) it must be truncated at a very large value of  $R$ . Examples of the parameter ( $x$ )

could be; the energy of the state from which the decay occurs by thermal excitation, and the distance that a defect site is from an interface where QM tunneling occurs between defect site and interface.

In the case of QM tunneling, the probability of barrier penetration for a constant barrier height, is given by

$$P(x) = e^{-Bx} \quad (13)$$

If this probability is multiplied by the frequency of penetration attempts, the rate of penetration obtained is

$$R(x) = fe^{-Bx} \quad (14)$$

If the traps have an exponential distribution as a function of depth, from the interface into the oxide, given by

$$n(x,0)dx = N_0 e^{-\beta x} dx \quad (15)$$

And if the value of  $x$  found from Equation 14:

$$x = [\ln f/R]/B \quad \text{and} \quad dx = -dR/RB \quad (16)$$

is substituted into Equation 15, then

$$n(R)dR = \frac{N_0 f^{-\alpha} R^{\alpha-1}}{B} dR \quad R \leq f \quad (17)$$

Where  $\alpha = \beta/B$

Which is the same functional form as Equation 12b. Since  $n(x,0)$  is undefined for  $x$  less than zero,  $n(R)$  must be truncated at  $R=f$ . Note, in Equations 4 through 7 any function  $x = F(y)$ ,  $dx = F'(y)dy$  could be substituted for  $x$  and Equation 8 would be unchanged.

There are two detrapping mechanisms known, QM tunneling and thermal emission. Can thermal emission be modeled using the Curie-von Schweidler law? The rate of emission is given by,

$$R(E) = \nu e^{-E/kT} \quad R \leq \nu \quad \text{and} \quad dR = -R/kT \quad (18)$$

where  $\nu$  is a frequency term and  $R_{\max}^{-\alpha}$

Then substituting into

$$n(R)dR = \frac{R^{\alpha-1}dR}{R_{\max}^{\alpha}} \quad (19)$$

which is normalized to one trap by substituting  $1/R_{\max}^{\alpha}$  for  $N_0$ .

$$n(E)dE = \frac{\alpha}{kT} e^{-\alpha E/kT} dE \quad (20)$$

Thus, if the distribution of trap energy levels is exponential, then the annealing will follow the inverse fractional power law. There is reason to believe the exponential distributions will occur. If the trap results from the distortion of a bond by high temperature processing, let  $\alpha = T/T_p$ . Then

$$n(E)dE = \frac{1}{kT_p} e^{-E/kT} P dE \quad (21)$$

and  $n(E)$  is not dependent on the annealing temperature and  $\alpha$  is about  $30^\circ \text{K}/1273 \text{ K}$  or 0.236. H. Scher and E. W. Montroll (Ref. 7) give  $t^{-\alpha}$  as the jump time distribution for hopping in selenium and F. B. McLean and G. A. Ausman Jr. (Ref. 6) extended that theory to  $\text{SiO}_2$ , with  $\alpha \approx .25$ . R. C. Hughes (Ref. 15) describes these traps as a distribution of Si-O-Si bond angles. As these bond angles must result in a Boltzmann distribution of bond energies from processing and this involves the binding energy of the electron, the above results.

In this section, it was shown that the Curie-von-Schweidler law results in a power law for the distribution of detrapping rates. The power law detrapping rate distribution in turn results from both QM tunneling through a barrier of constant height and from thermal emission from an exponential distribution of activation energies.

## 2.2 EXTRAPOLATION ALGORITHM

The extrapolation algorithm is used to convert data from an irradiation and anneal test to a prediction of what would be expected from a long irradiation. The first part of the derivation of this algorithm is contained in Equations 2 to 5 of Section 1.4. The derivation is resumed with Equation 5, which is rewritten here

$$n^+(R, t) = n(R) [H/(H+R)] [1 - e^{-(H+R)t}] \quad (5)$$

Where:

$R$  is the rate of hole detrapping by full sites

$n_0(R)dR$  is the number of traps with decay rate  $R$  in the interval  $dR$

$n(R,t)$  is the number of traps containing a trapped hole

(note that the unit of time in the above is still arbitrary)

$H$ , the rate of hole capture by empty sites, is found by multiplying the flux of holes impinging on a trap by the trap cross section. Since the flux is proportional to the dose rate so is  $H$ . Equation 5 is integrated over  $R$  to parallel Equation 7 giving

$$N(t) = \int_0^{\infty} n(R) [H/(H+R)] [1 - e^{-(H+R)t}] dR \quad (22)$$

When Equation 12b is substituted for  $n(R)$

$$N(t) = \frac{N_0}{\Gamma(\alpha)} \int_0^{\infty} R^{\alpha-1} [H/(H+R)] [1 - e^{-(H+R)t}] dR \quad (23)$$

$$= N_0 H^{\alpha} \gamma(1-\alpha, Ht)^* \quad (24)$$

where  $\gamma(a,x)$  is the incomplete gamma function.

$$\gamma(a,x) = \int_0^x \eta^{a-1} e^{-\eta} d\eta$$

---

\* The details of the integration are in the Appendix.

This function is shown in Figure 1 for different values of  $a$ . Note that the sublinear initial slope is a result of analyzing data using this algorithm. The sublinear slope, which has been frequently observed, can be understood as the natural result of annealing. For  $Ht < 1$  the  $\gamma$  function is approximated by

$$\gamma(a, x) \approx x^a/a.$$

This approximation is very good up to  $x=.4$ . Putting this approximation in Equation 24 results in

$$H^\alpha \gamma(1-\alpha, Ht) \approx H t^{1-\alpha}/(1-\alpha).$$

Note that the value and slope are proportional to  $H$  and thereby  $\dot{\gamma}$ . For values of  $Ht > 1$

$$\gamma(a, x) \approx \Gamma(a)$$

This approximation seems to be good for  $x > 3$  and Equation 24 is

$$H^\alpha \gamma(1-\alpha, Ht) \approx H^\alpha \Gamma(1-\alpha)$$

The saturation value is proportional to  $H^\alpha$  and  $\alpha$  is normally less than .5 probably less than .1. So a large reduction in the saturation value will not result from very slow irradiation.

In the above, the annealing curve is for the case where all the trap sites were filled, with a hole, at time zero. In the real case, the traps must be filled in a finite time during which some traps anneal. During irradiation, the growth of trapped charge is described by Equation 24. At the end of the exposure the distribution of filled states is given by the integrand of Equation 23; i.e.,

$$n^+(R)dR = [N_0/\Gamma(\alpha)]R^{\alpha-1}[H/(H+R)]\{1-e^{-(H+R)\tau}\}dR \quad (25)$$

where  $\tau$  is the exposure time.

Note that while the number of trap sites with decay rate  $R$  is given by

$$n(R) = N_0R^{\alpha-1}/\Gamma(\alpha) \quad (25)$$

the fraction of trap sites with a trapped hole is found from Equation 5), i.e.,

$$[H/(H+R)]\{1-e^{-(H+R)\tau}\} \quad (26)$$

and that some of the sites have been filled and emptied before the end of the exposure. Equation 25 can be integrated to get

$$N(t) = [N_0/\Gamma(\alpha)] \int_0^{\infty} R^{\alpha-1} [H/(H+R)] \{1-e^{-(H+R)\tau}\} e^{-Rt} dR$$

$$= N_0 H^\alpha e^{Ht} [\gamma(1-\alpha, H(t+\tau)) - \gamma(1-\alpha, Ht)]^* \quad (27)$$

Where the time  $t$  is measured from the end of the exposure, i.e., the clock is reset to zero time at the end of the exposure (this is the way graphs of this function are presented). For large  $Ht$ , Equation 16 is approximated by

$$N(t) \approx N_0 [1 - e^{-H\tau}] / t^\alpha \quad (28)$$

In Figures 2, 3 and 4, irradiation curves and the resulting annealing curves ( $\tau=3600$ ) are shown. Also, the low level irradiation curves which would result are shown to the right. The annealing curves are plotted on two time scales: first, as a continuation of the irradiation curve, and second, as in Equation 27, starting at  $t = 0$ . The two curves were plotted by computing Equation 27 and plotting that result as the ordinate value at two abscissa values,  $t$  and  $t+\tau$ . These three figures show how well the algorithm represents the physics of the problem. First, the saturation is clearly shown. Secondly, during irradiation, fast traps, with a fast detrapping rate  $R$ , will detrapp and trap another hole during irradiation. In saturation, there is a small increase of the unannealed fraction with larger value of  $H$ , due to these fast traps. Following irradiation, the fast traps will decay quickly bringing the value of the unannealed fraction closer to that for smaller values of  $H$  in a time approximately equal to that of the irradiation, which is one hour in these three figures.

---

\* The details of the integration are in the Appendix.

An irradiation curve at  $H=1.E-8$  is shown on the right of Figures 3 and 4. This would be the long term irradiation curve that would result from the low radiation levels of the space environment.

For hardness assurance testing, it is important to realize that more accurate information is obtained in the same time by using a short intense irradiation followed by a longer anneal period than by using a lower level irradiation for the whole time. In an irradiation curve, the fast traps add to the slower traps thus using up some of the digits of accuracy. In an annealing curve, the value of each measurement is from mostly the traps with detrapping periods greater than the measurement time. Thus, the accuracy which results from mathematically stripping out the detrapping distribution is greater. The irradiation curve for  $H=1.E-8$  rises above the  $H=3.2E-3$  annealing curve in the figures because of the adding of these faster traps.

The above algorithm needs error limits determined for the assumptions if it is to be used with confidence. While the adjustment of  $N_0$  and  $\alpha$  will fit most experimental annealing curves with great accuracy, the use of the algorithm to extrapolate to much longer times is dependent on Equation 12b being the correct functional form for the distribution of detrapping rates. If this is not true, then a true distribution with a different proportion of traps with long trapping times would be most damaging to an application which was taking advantage of annealing to permit the use of softer parts. The case of a higher proportion of long term traps is simulated below by having a percentage of the traps not anneal at all. In this case, Equations 12a and 12b become

$$N(t) = N_0/t^\alpha + N_1 \quad (29a)$$

$$n(R) = N_0 R^{\alpha-1} / \Gamma(\alpha) + N_1 \delta(R) \quad (29b)$$

where  $\delta(R)$  is the Dirac delta function

A numerical evaluation of the fraction of filled traps which results when the nonannealing traps are included in the distribution follows. Then, the error that results when the original functional form is assumed for the distribution is analyzed. When the distribution of Equation 29b is used, the fraction of filled traps during irradiation is given by

$$N(t) = N_0 H^\alpha \gamma(1-\alpha, Ht) + N_1 (1 - e^{-Ht}) \quad (30)$$

Following irradiation, the same fraction is given by

$$N(t) = N_0 (\gamma[1-\alpha, H(t+r)] - \gamma[1-\alpha, Ht]) + N_1 (1 - e^{-Hr}) \quad (31)$$

In the next fifteen figures (less Figures 2, 3 and 4), the annealing curve which is a continuation of the irradiation curve, will be used as the background. To this background will be added on successive sets of three figures; an error curve, and the results of treating this error curve as pseudodata. Adding all the curves at once would make the figures confused. To keep the curves readable only one set of computations is added at a time and the curves can be separated by flipping back and forth.

In Figures 5, 6 and 7 the curves computed according to Equations 30 and 31 are added to this background (dashed line) and by comparing with the background curves show the error which was introduced. This error curve is plotted with  $N_0=.9$  and  $N_1=.1$  i.e. 10% of the traps are outside the distribution. To evaluate the consequences of this error, the calculation of the unannealed fraction is treated using Equations 30 and 31, for times less than a week, as though it was the experimental irradiate and anneal data from which the prediction is to be made. A least square fit is performed, fitting Equations 24 and 27 to the calculated data out to one week to obtain the parameters  $N_0$ ,  $H$ , and  $\alpha$ . Finally, using these parameters from the least squares fit in Equations 24 and 27, the annealing and the low level irradiation fraction are predicted for times longer than a week. These predictions are added to Figures 5, 6 and 7 to get Figures 8, 9, and 10. This results in a prediction\* of filled traps which is generally higher (therefore safe) than the assumed real case. Included in these figures are the plots of the fits to the pseudodata obtained by putting  $N_0$ ,  $H$ ,  $\alpha$ , and  $t$  into Equation 27. Note the way the pseudodata, Equation 31, and the fit deviate from each other at about one week. When this method is applied to real data, careful examination of the deviation of the data, taken at the longest times, from the straight line fitted, will give warning of predictions from the method which might be badly in error.

Next, consider a trap distribution where the proportion of long term traps is less than the given by  $R^{\alpha-1}$  form. Will a least square fit to the

---

\* shown as a long dashed line  $H=1.E-4$ , a dash-dot line  $H=1.E-3$ , and a dash-dot-dot line  $H=1.E-2$

first week of data under-predict the long term filled trap fraction? For example, consider the case where there is hole escape by tunneling and by thermal activation  $\kappa = \nu e^{E/kT}$ . The total rate is found by summing the rate from each competing path.

$$R = fe^{-Bx} + \kappa \quad \text{note } R > \kappa \quad (32)$$

Equation 32 can be put through the same analysis used in Equation 14, i.e.

$$n(x) = \beta e^{-\beta x} dx \quad \text{note, } n(x) \text{ is normalized} \quad (33)$$

$$x = \frac{\ln[(R-\kappa)/f]}{B} \quad dx = \frac{dR}{B(R-\kappa)} \quad (34)$$

$$\begin{aligned} n(R)dR &= \left(\frac{\beta}{B}\right) \left[\frac{R-\kappa}{f}\right]^{B-1} dR \\ &= \alpha \left(\frac{R-\kappa}{f}\right)^{\alpha-1} \end{aligned} \quad (35)$$

$$\begin{aligned} N(t) &= \alpha \int_0^{\infty} \left(\frac{R-\kappa}{f}\right)^{\alpha-1} e^{-Rt} dR \\ &= N_0 \frac{e^{-\kappa t}}{t^\alpha} \end{aligned} \quad (36)$$

$$\text{where: } N_0 = \frac{\alpha \Gamma(\alpha)}{f^{\alpha-1}} = \alpha \Gamma(\alpha) f^{1-\alpha}$$

in the case of constant radiation;

$$\begin{aligned}
N(t) &= \frac{N_0}{\Gamma(\alpha)} \int_{\kappa}^{\infty} (R-\kappa)^{\alpha-1} \left( \frac{H}{H+R} \right) [1 - e^{-(H+R)t}] dR \\
&= N_0 \frac{H}{(H+\kappa)^{1-\alpha}} \gamma[1-\alpha, (H+\kappa)t]^* \quad (37)
\end{aligned}$$

and for the case of annealing following a constant irradiation;

$$\begin{aligned}
N(t) &= \frac{N_0}{\Gamma(\alpha)} \int_{\kappa}^{\infty} (R-\kappa)^{\alpha-1} \left( \frac{H}{H+R} \right) [1 - e^{-(H+R)\tau}] e^{-Rt} dR \\
&= N_0 \frac{H}{(H+\kappa)^{1-\alpha}} e^{Ht} (\gamma[1-\alpha, (H+\kappa)(t+\tau)] - \gamma[1-\alpha, (H+\kappa)t])^* \quad (38)
\end{aligned}$$

It will turn out that the above is a very good approximation to the case in the physical model, where there is tunneling to the interface ( $e^{-Bx}$ ) and thermal emission ( $\kappa$ ).

In Figures 11, 12 and 13, the curves computed according to Equations 37 and 38 are added to this background (dashed line) and by comparing with the background curves show the error which was introduced. This error curve is plotted with  $\kappa=1.E-6$ ; i.e., at about one day the curve deviates by a factor 0.4. Again, a least square fit is performed, fitting Equations 24 and 27 to the calculated data out to one week to obtain the parameters  $N_0$ ,  $H$ , and  $\alpha$ . And again, using these parameters from the least squares fit in Equations 24 and 27, the annealing and the low level irradiation fraction are predicted for times longer than a week. These predictions are added to Figures 11, 12, and 13 to get Figures 14, 15, and

---

\* The details of the integration are in the Appendix

16. This results in a prediction of filled traps which for times  $Ht < 0.4$  is generally lower than the assumed real case. Note that the effect of this exponential in  $\kappa$  is to lower the saturation value on an irradiation curve without changing the values on the slope for  $(H+\kappa)t < 0.4$ . This will cause the prediction to underestimate in this region.

It turned out that for  $\alpha = 0.1$  there was little error in the prediction and very little difference between the pseudodata and the fit at one week. In the case of the floor at  $\kappa = 1.E-6$  there was little error for  $\alpha = 0.5$ . So the program was rerun at  $\kappa = 1.E-5$ , and the results plotted in Figures 17, 18 and 19. In the  $\alpha = 0.1$  case the pseudodata was off scale for  $H = 1.E-7$ . For  $\kappa = 1.E-5$ , the deviation from a straight line can be seen at one week and it is known that the prediction will underestimate before saturation and overestimate after.

The above is a derivation of the general algorithm. To use the algorithm, the circuits are first exposed and annealed. The value of the parameter (e.g., bulk charge; i.e.,  $N(t)$ ) is plotted on log-log scale and the slope " $\alpha$ " is found. Equation 24 is fit to the parameter data during exposure to obtain a correspondence between irradiation rate and  $H$ , and to find  $N_0$ . These estimates can be used directly or as starting values for a least square fitting routine to find the best fit to Equations 24 and 27 simultaneously to all of the data. Having  $N_0$ ,  $\alpha$ , and  $H$  for the data a prediction is made by inserting  $N_0$ ,  $\alpha$ , and  $H_p$  into Equations 24 and 27.  $H_p$  is given by

$$H_p = H \frac{\dot{\gamma}}{\dot{\gamma}_p} \quad (39)$$

i.e., the H for the expected irradiation rate can be found by noting that H is proportional to irradiation rate.

CHAPTER 3.  
PHYSICAL MODEL

3.1 INTRODUCTION TO PHYSICAL MODEL

At first, the objective of deriving a physical model was to see if data could be predicted from first principles. With each try it was necessary to include other phenomena and data. Soon it seemed as though the model was being fit to the data by the choices of what to include. Clearly, such a model using other questionable data and made up from physical phenomena chosen to predict data would not be verified by its prediction of that class of data. The verification of that model's ability to predict annealing over a five to ten year period, would have to await a five to ten year experiment. All that could be achieved was to use physical principles to constrain the possible mathematical forms the real data could be expected to follow. What was desired was some mathematical form,  $f(\alpha, \beta, \gamma; t)$ , which would follow the data accurately out to ten years and the numerical values of  $\alpha$ ,  $\beta$ , and  $\gamma$  could be determined from early data. All that can be expected, however, is to learn some things about the function  $f$ .

In this section, each of the possible physical processes by which detrapping can occur is analyzed to determine what they mean to the shapes of the plots of  $n(R)$  and  $N^+(t)$ . Only two physical processes are known to effect detrapping; Quantum mechanical (QM) tunneling and thermal emission. The data from Schwank (Ref. 5) showed dependence on electric field and temperature. The height of a tunneling barrier is modified by the

electric field but tunneling is temperature independent. The maximum energy of a barrier can also be modified by an electric field, but this requires a description of the shape of the trap energy well. It was shown in the previous section that QM tunneling (with no electric field) to the silicon interface almost exactly gives the Curie-von Schweidler law. Tunneling to the  $\text{SiO}_2$  valence band or thermal emission introduces a floor  $\kappa$  to the annealing rate as in Equation 32. Negative biases have a floor which can be dominated by either the tunneling to the oxide valence band or thermal emission. In the positive bias case, the tunneling to the silicon valence band transitions smoothly to the tunneling to the oxide in a way that results in anneal rates higher than those produced by Equation 32.

The model is based on the facts; (1) that the traps are within  $100\text{\AA}$  of the interface (Ref. 16), (2) that distributions of activation energies between 0.8 and 1.8 eV obtained by temperature accelerated annealing rates (Ref. 11) as shown in Fig. 20, and (3) that these are hole traps resulting from an excess silicon center (Ref. 14). It was concluded in Ref. 17 that the traps are intrinsic to the growth process and are thus likely to have an exponential distribution. In addition, there are annealing data (Ref. 5) as a function of temperature and bias against which to test this model. The question of an exponential distribution of the trap sites has been addressed by Oldham, et al (Ref. 18). Using an analysis based on Eq. 1 and tunneling, they found that hard oxides follow an exponential distribution. The one commercial oxide they looked at seemed

constant over the first 15 Å\*. The constant distribution gives a logarithmic form (Ref. 19) for the annealing curve.

$$N^+(t) = [-A \ln(t/t_0) + C]/\gamma_0 \quad (40)$$

Actually, because the constant distribution can not be normalized without truncating (i.e., Equation 40 goes to  $\infty$  as  $t \rightarrow \infty$ ) three constants are needed for the above.

In the following, QM tunneling will be looked at in a simple one-dimensional model first. A hydrogen atom model (Ref. 20) using an analysis from (Ref. 21), was tried, but did not give useful results. The hydrogen atom model does not correspond physically to the configuration of the trap. A spherical potential well model (Ref. 21) was then tried to get a self-consistent model, but it predicts the Schwank data (Ref. 5) to be only marginally successful.

### 3.2 ONE-DIMENSIONAL MODEL

The one-dimensional model uses a 1-D barrier and a rough estimate,  $10^{15.5}$ , for the frequency constant  $f$ . Tunneling from an excited trap was also included. This excited trap level must result from a general excitation of the other electrons in the vicinity as all hole orbitals are

---

\* This is computed for a single level at 3.1 eV. For the 0.8-1.8 eV range centered at 1.25 eV used in this paper, 3.1 eV corresponds to 24 Å. It still could be an exponential distribution but  $\beta$  must be greater than  $1E-6$

occupied. Actually, this is more like phonon assisted tunneling than tunneling from an excited state. However, treating it like a short lived, therefore broad, excited state allows the use of the .41 eV activation energy given by Schwank and permits the use of the same frequency constant that was used for the ground state.

In Figure 21, the hole traps are shown with tunneling from the trap ground state and first excited level to the interface and the oxide valence band (i.e., the bonding levels). Shown is a close trap (1), where both the ground and the excited level tunnel to the interface; a medium depth trap (2), where the ground state tunnels to the interface but the excited state tunnels to the  $\text{SiO}_2$  valence band; and a deep trap (3), where both the ground and excited states tunnel to the valence band. Note that for the tunneling between the trap levels and the oxide bonding levels, the tunneling barrier is constant with depth. This is the tunneling floor for tunneling to the oxide under positive bias. The smooth transition to this floor results from the continuous barrier lowering which preceded the barrier going to zero. For the following discussion, let (g) stand for the ground state and (e) the excited state. Then, the barrier penetration paths can be labeled using Figure 21, for example (2e) is the path from excited state to the valence band.

The barrier heights for negative, positive and zero electric fields are shown in Figure 22. As the height at  $x = 0$  is arbitrary, this could be from either the ground or excited state. Note that the barrier height for the positive field goes to zero with increasing depth and then remains zero for further increases in depth. The tunneling rates have been

computed using the W.K.B. method\* (Ref. 22) as a function of trap depth.  
 Rewriting Equation 14 gives

$$R(x) = fe^{-\rho} = fe^{-\int_0^x B(x') dx'} \quad (41)$$

The barrier is given by

$$B(x) = 2\sqrt{2mH/\hbar^2} \quad (42)$$

where:  $H = E + \epsilon(x'+x)$  in eV.

$\epsilon$  is the field in V/cm

$E$  is the trap energy in eV

$m$  is the effective mass of the hole

$\hbar$  is Planck's constant  $/2\pi$

The integral is

$$\begin{aligned} \rho &= \int_0^x B(x') dx' \\ &= \kappa(2E/3\epsilon) [1 - (1 - \epsilon x/E)^{3/2}] \quad \text{for } \epsilon x > E \end{aligned} \quad (43a)$$

$$= 2\kappa E/3\epsilon \quad \text{for } \epsilon x \geq E \quad (43b)$$

where  $\kappa = 2\sqrt{2mE/\hbar^2}$

---

\*also called the classical approximation (see Born, Ref. 22) formula (4' Section 12.11)

Then the rate of detrapping by tunneling from the ground state is given by

$$R_g = fe^{-\rho} \quad (4-a)$$

and the rate of detrapping from the excited state is given by

$$R_x = fe^{-\rho_x - E'/kT} \quad (4-b)$$

where  $\rho_x$  is found using Equation 43 but with the energy of the excited level

$E - E'$  is substituted in the equation instead

$E'$  is the amount of excited energy, 0.41 eV is used in the numerical evaluations.

The total rate of detrapping is given by

$$R = R_x + R_g \quad (45)$$

These functions are displayed in Figure 23. The lower solid line curve is Equation 44a plotted for the energy and field shown. The upper short dashed curve is Equation 44a for that energy less 0.41 eV, which was the thermal activation energy quoted by Schwank (Ref. 5). The rate of detrapping by tunneling from the excited state is gotten by multiplying the upper curve by the Boltzmann factor  $e^{-0.41/kT}$ , as shown in Equation 44b, which is the probability that the trap is in the excited state. These curves for  $T = 275$  to  $400$  K are shown in broken line patterns below the upper solid line. This curve shows where the detrapping is dominated

by tunneling from the ground state and where the excited state. Also shown is the way the detrapping curve flares into the tunneling floor where tunneling is to the oxide valence band rather than the oxide-silicon interface. Finally, note that over the range one second to one year a straight line is a good approximation. However, for some E and  $\xi$  the floor will fall in the range, as shown in Figure 24, and a straight line will be a poor approximation. If the straight line approximation is good then,  $\rho \approx Bx$  and by Equation 14 we have the Curie-von-Schweidler law.

The values computed from Equation 45 can be numerically integrated using Equation 7 to predict the annealing curve. This was done for E=0.8 to 1.8 eV. The result must be averaged by integrating over the distribution of trap depth energies.

$$N^+(t) = \int_0^{\infty} D(E) \left[ \int_0^{\infty} e^{-\beta x} e^{-R(E,x)t} dx \right] dE \quad (46)$$

Where:  $D(E)dE$  is the distribution of the trap depth energies, Figures 20 and 25.

$e^{-\beta x} dx$  is the distribution of trap to interface distances

By doing the inner integral over x instead of over R a nasty singularity as R approaches the tunneling floor is avoided. The double integral was done by using Simpson's rule twice, and the results are shown in Figures 26, 27, 28 and 29, along with the measurements from Schwank (Ref. 11). The second integral is done by simply multiplying by the values in Figure 20 and adding because the values of  $D(E)$  are zero at either end, and because

$D(E)$  has been normalized. This integral has to be done for each value of  $t$  desired. Here the integral parametric in  $T, \xi, \beta$  [ $1.E7, 4.6E6$ , and  $2.E6 \text{ cm}^{-1}$ ] has been done for three different distributions  $D(E)$  [1,3,4].

In Figure 26, the computations for  $T=375 \text{ K}$ ,  $\beta=1.E7$  and for  $D(E) \#4$  are shown as the dashed line. The electric field strengths are labeled. The  $100^\circ\text{C}$  Schwank data are shown with the points marked by vertical tics and are labeled using the the applied voltage, which was across  $450 \text{ \AA}$ .  $S$   $10 \text{ V}$  is about  $2.2E6 \text{ V/cm}$ . The Schwank data for  $-10 \text{ V}$  are off scale just above the zero line. In Figure 27,  $D(E) \#1$  is substituted, and computations for  $\epsilon=2.E6$  are off scale to the right. In Figure 28,  $\beta=2.E6$  was substituted causing the three curves at the three lower values of  $\epsilon$  to be compressed toward the zero annealing line, where the  $-10 \text{ V}$  data line should be. So  $\beta=1.E7$  and the  $\#4$  distribution, as shown in Figure 26, are the closest fit among the parameters for which the calculations have been done. If  $\beta=1E7$ , the traps very close to the interface,  $10 \text{ \AA}$ . The  $\#4$  distribution was taken from an N-channel transistor while the  $\#1$  and  $\#3$  distributions came from a P-channel. In Figure 29, the data and computations are shown with temperature as a parameter.

This looked very good, almost like the computations succeeded without fitting any parameters to the data. However, the computations at high fields were too low, and later data from Schwank (Ref. 23) at an applied voltage of  $20 \text{ V}$  were just below the  $10 \text{ V}$  while the computations were off the graph. So Denchenko (Ref. 11) was contacted and he prevailed on Fang (Ref. 24) to smooth their data and extrapolate it to deeper values of energy. The results are shown as  $\#2$  in Figures 20 and 25.

Schwank's later data are shown in Fig. 30. Annealing continues to increase with temperature  $100^{\circ}\text{C}\rightarrow 125^{\circ}\text{C}$  and with applied field  $10\text{V}\rightarrow 20\text{V}$ . The calculations made with the extended energy distribution, #2, are shown in Figure 31. To see the change, contrast that with the unextended, #3 shown in Figure 26. The curve at  $4.4\text{E}6$  is off scale to the right. In Equation 46 the form  $e^{-Rt}$  was used instead of  $(1 - e^{-(H+R)\tau})e^{-Rt}$ . Thus, the computed results are for an impulse irradiation. There should be a sharp drop in Schwank's data in the first hour which are not simulated by the computation. Compare with Figures 2, 3 and 4. Recomputing required a value for H, which was not available since Schwank irradiated at the temperature of his gamma cell and then annealed at the chosen temperature. Thus, there are no data at the annealing temperature from which to derive H by fitting. Also, the comparison of the data parametric in temperature show poor simulation, Figure 32. Clearly the spread in the computed curves does not correspond with nature. The one-dimensional model treats the influence of voltage well, but, the treatment of the temperature influence is insufficient.

### 3.3 SPHERICAL WELL MODEL

The one-dimensional model did not handle temperature well. In addition, the conversion from 1D to tunneling from a point trap to a plane interface was handled by the frequency factor  $f$  whose value  $10^{15.5}$  was an approximation made without a proper error analysis. By handling the trap as a hydrogen atom, as was done by Kittel (Ref. 20) for impurity levels in silicon, a treatment of tunneling similar to 1D was obtained. The variation with temperature was modeled using thermal emission. Because of

barrier lowering, the applied field increased tunneling beyond that of the barrier shown in Figure 22, and made thermal emission voltage dependent. A treatment which could be modified to fit this case was found in Landau and Lifshitz' book (Ref. 21). This treatment was for ionization of hydrogen atoms by tunneling at low electric fields like those found in space. The modified treatment, called the hydrogen atom model, allowed high fields and a tunneling barrier between the trap and the silicon-SiO<sub>2</sub> interface. The annealing curves given by this model cut off as in Equation 36 or as when there is a floor. More than a 1.75 eV trap depth was required to get lines approximately straight on a log-log scale. The coulomb potential is subject to barrier lowering by the electric field to a much greater degree than square well potentials. Also, the hole is not orbiting around a negatively charged center, so this model is not theoretically correct. The trap is neutral when no hole is trapped. What was needed was a well, attractive near the center but otherwise free field. Because of these considerations, a spherical square well was tried.

Tunneling from a spherical potential well in the presence of an applied electric field is also covered by Landau and Lifshitz (Ref. 21, pp 294). They treated only the case where the barrier is reduced to zero by the field, whereas here the barrier is also terminated by the interface. Since the results were not predictive the detailed mathematical derivation is not included here.

The spherical well barrier is given by

$$B(x) = E(1 - \xi\eta - \frac{2}{\eta} + \frac{1}{\eta^2}) \quad (47)$$

where:  $\eta = 2\kappa x$

$$\kappa = \sqrt{2mE/\hbar^2}$$

$$\xi = \epsilon |e| m / \hbar^2 \kappa^3$$

In Figures 33 and 34,  $B(x)/E$  is plotted for different  $\epsilon$ . The spherical well is between 0 and some radius ( $a$ ). Lines have been drawn at 2, 4, and 8 Å to show ( $a$ ), the beginning of the barrier. Note that the height of the barrier at ( $a$ ) is a function of  $\epsilon$  and  $E$ . The actual lowering is  $\epsilon a$ .

This barrier was integrated numerically and inserted for  $\rho$  in Equation 41. The constant  $f$  is given by

$$f = \frac{\hbar\kappa^2}{m} \left( \frac{2\pi(BA)^2 e^{-\eta_0} \left| 1 - \epsilon\eta \frac{2}{\eta_0} - \frac{1}{\eta_0^2} \right|}{\eta_0} \right) \quad (48)$$

where:  $\eta_0 = 2\kappa a$

$$B^2 = 1/(\kappa a + 1)$$

$$A \text{ is found from } \sin(\kappa a) = A e^{-\kappa a}$$

$$k \text{ is found from } \tan(\kappa a) = -k/\kappa$$

The formulae for  $A$  and  $k$  are found from matching the amplitude and derivative of  $\sin(\kappa a) = A e^{-\kappa a}$  at the spherical well boundary ( $a$ ). The value of  $f$  is between  $2E^{15}$  and  $9E^{15}$  for  $a = 1$  to 8 Å and  $E = 0.8$  to 2 eV.

Temperature dependence is introduced by including thermal emission. The rate of emission is given by (Ref. 25)

$$R_e = \sigma v_{th} N_v g e^{-E/KT} \quad (49)$$

where:  $\sigma$  is the hole capture cross section

$v_{th} = \sqrt{3KT/m}$  is the thermal velocity

$N_v = 2 \left( \frac{2\pi mKT}{h^2} \right)^{3/2}$  is the density of states in the valence band of the  $SiO_2$ .

$g = 1$  is the degeneracy of the state

$KT$  is the thermal energy.

Choosing  $\sigma = 1E-16$  which is the center of the range of capture cross sections of neutral hole traps in silicon, this reduces to

$$R_e = 4.39E13 (KT)^2 e^{-E/KT}$$

and  $R = R_e + R_t \quad (50)$

where:  $R_t = fe^{-\rho}$  is the partial detrapping rate from tunneling

Using this model with  $a = 2\text{\AA}$  and  $\sigma = 1E-16$  computations of the annealing rate were made. In Figures 35 and 36, these computations are compared with the Schwank data, parametric in electric field and temperature, respectively. Clearly the model is not producing the necessary variation of annealing slope with electric field or with temperature.

Some correction, could be achieved if a larger  $\sigma$  could be used in Equation 49. By comparing log-log plots of the irradiation data published by Schwank (Ref. 5), taken at 10 V gate bias and gamma cell temperature 30°C), to the irradiation curves in Figure 5 it could be determined from the curvature that H must be about 6E-4. Since, the flux of holes passing the traps is given by the rate they are generated per unit volume times their thickness, the probability per unit time is this flux times the trap hole capture cross section,

$$H = \sigma G t D$$

where:  $G=0.05(\text{ion pair/eV})100(\text{erg/gr-rad})2.27(\text{gr/cm}^3)/[1.6E-12(\text{ergs/eV})]$   
 $(=7E12 \text{ ion pairs /rad/cm}^3)$

$$t=450 \text{ \AA}$$

$$D= 1 \text{ Mrad/hr}=278 \text{ rad/sec}$$

This equation is solved to get  $\sigma=7E-14 \text{ cm}^2$ . Using this  $\sigma$  would increase the the variation of annealing with temperature. To increase the variation with electric field the (a) could be increased. These values of cross section and well radius were used in the computations presented in the following.

The partial rate,  $R_e$ , is plotted in Figure 37, for energies stepped from 0.8 to 2 eV step size 0.05 and a very small, approximately zero, field. The thermal emission rates,  $R_t$ , are added to  $R_e$  to give the total P in regions on the right. The sum for T=275 K, is plotted between 130 and 140 Å; 300 K between 140 and 150 Å; and so on until 400 K is plotted

between 180 and 190 Å, giving the rising step curves on the right. Actually, each thermal emission rate is constant over all  $x$ , but is plotted over the limited range to show the position of its values without obscuring the plot of the tunneling rates. Note that the tunneling rate plots are straight lines on a semi-log scale, even though this is not a constant height barrier. Equation 46 is used to convert the rate to an annealing curve. Note, for times less than about 1 hr, that the  $e^{-\beta x}$  and the tail off in the distribution of trap depth energies will emphasize the straight lines sloping down from the upper right corner. A straight line on a semi-log scale will give  $e^{-Bx}$ , which when inserted into the derivation surrounding Equation 14 will give the Curie-von Schweidler law. Later times emphasize the floor lines caused by thermal emission in this case, and given an exponential distribution of trap depths will also give the Curie-von Schweidler law. This is the most useful result of the physical model study.

A similar method of display is used for Figures 38, 39, 40 and 41, which show the detrapping rates for electric field strengths 0.56E6, 1.1E6, 1.7E6 and 2.2E6 V/cm. The purpose of showing these figures is to illustrate the manner that the dominance of the floor of the rate curves shifts from thermal emission to tunneling as the electric field is increased. This is one of the mechanisms that produces a variation of the annealing curves with electric field. However, this is inadequate as it takes 2.2E6 V/cm to assert this dominance in the  $1 \text{ hr}^{-1}$  to  $1 \text{ day}^{-1}$  range. That this mechanism failed is seen in Figure 35. Since the floor of most of the curves is dominated by thermal emission, this must change with electric field. Close examination of these curves will show that this is

increasing with electric field. Barrier lowering by the electric field has been included in the  $E$  inserted in Equation 49. This barrier lowering is shown in Figures 33 and 34. The amount of barrier lowering is the radius ( $a$ ) times the field, which is why the unrealistic value of 8 Å was chosen.

In Figures 42 and 43, the total rate  $R$  is plotted  $x=8$  to 200 Å, for temperatures 275 and 375 K, respectively. These figures show the variation of the rate with temperature and the seemingly universal shape of the rate curves, i.e., the rate will follow an approximately straight line down to a floor. This type of curve is closely approximated by Equation 32.

The model fails to produce reasonable results for either negative or very large positive electric fields. Experimentally negative fields do not anneal at all (Ref. 5). According to the physics used to derive the model there should be detrapping from tunneling to the silicon interface, thermal emission and tunneling to the valence band (the other direction into the oxide). The last two would be equal in value to a positive field of equal magnitude. Thus, the annealing should be nearly as large as the annealing from a positive field. It isn't. Secondly, as shown in Figure 30 annealing at 20 V is only moderately greater than at 10 V. Figure 44 shows how much larger the annealing rates that the model gives are compared to the preceding figures.

Truncation of the annealing curves can be caused by the combination of the truncation of the energy distribution and the flaring out to a factor of the detrapping rate. To avoid annealing curve truncation, the

additional energy distribution, shown in Figure 45, was added to the computation matrix. This is an extension of the gaussian to 2 eV. Note the value at 2 eV is only 1E-8.

Inserting these five distributions and three values, 1E7, 4.5E6 and 2E6 cm<sup>-1</sup>, of the tunneling depth parameter  $\beta$  into Equation 46 gives the annealing curves plotted in Figure 46. This curve is for 375 K and 2.2E6 V/cm field. The curves for the different values of  $\beta$  must be identified by their starting point on the left, 1E7 on the bottom. Notice how each curve truncates with the exponential  $e^{-\kappa t}$  where  $\kappa$  is the detrapping rate at the energy where the energy distribution is truncated. The point of these curves is that the energy distributions for these calculations must be extended even to contributions as low as 1E-8 to be accurate out to five years. This is not a practical quality assurance method.

The next two figures, Figures 47 and 48, locate the position of the results for 4.4E6 V/cm. In Figure 47, the curve for  $a=8\text{\AA}$  and  $\sigma=7\text{E-}14$ , only the plot of the result from distribution #5, is on scale. In Figure 48 the results of the earlier computation, at  $a=2\text{\AA}$  and  $\sigma=1\text{E-}16\text{ cm}^2$ , are shown. The results from both distributions #4 and #5 are on scale, those from #5 give a straight line and those from #4 show the  $e^{-\kappa t}$  truncation. The only way these curves could be put near enough to the 2.2E6 V/cm results to resemble the data in Figure 30 is to add traps at higher energy levels, perhaps at the 3.1 eV used by Reference 18, to the trap energy distribution.

Finally, these results are compared with data (Ref.5) in Figures 49 and 50. Clearly, more variation with voltage is needed. Increasing the well radius only in the barrier lowering used for the thermal emission calculation, while reducing it to perhaps 1 Å in the tunneling calculation might help. Perhaps, in the temperature variation comparison, Figure 50, adjusting  $\sigma$  to about  $2E-13 \text{ cm}^2$  would raise the 275 K results to match the 25°C data.

### 3.4 PHYSICAL MODEL SUMMARY

The attempt to develop a physical model showed that the annealing curves expected from basic mechanism considerations will be approximately a straight line on a log-log scale. This is the result of the way the basic phenomena interact. This attempt did not cover distributions of traps with distance from the interface that were other than exponential. The uniform distribution has been covered (Ref. 19), and produced a logarithmic annealing curve which is also an approximately straight line on a log-log scale.

To match data, the model needs further adjustments. The edge of the spherical well needs to have the top at a radius of 10 Å or more and the deep part of the well needs to be within a radius of 1 Å. Then, using the infinite adjustments available from the energy distribution of the traps and adjusting  $\sigma$ , the data (except for that taken at negative fields) can be fitted. For negative fields, as the detrapped hole must now travel clear across the 450 Å oxide film rather than 5-20 Å, retrapping is

assumed. Making these adjustments to the model and comparing to a much larger variety of data still would not lead to a useful model.

## CHAPTER 4.

### CONCLUSIONS

There exists a mathematical model based on an Curie-von Schweidler law which is mathematically convenient and is an adequate approximation for extrapolating data on device positive charge annealing taken over a one week period to a five year mission. This model:

- o Is the asymptote of various physical models
- o Is largely in mathematical closed form, which permits predictions to be made from data on a small personal computer.
- o Cannot be verified experimentally because of the five years needed for the experiments. However, a study of the basic mechanisms involved indicates it will be an accurate approximation.

An exhaustive attempt to construct a physical model using the physical phenomena tunneling and thermal emission did not lead to a model useful for making long term predictions.

APPENDIX  
INTEGRATION DETAILS

The basic trick to doing the integrals in this section is to recognize that

$$\frac{1 - e^{-(R+H)t}}{R+H} = \int_0^t e^{-(R+H)t'} dt' \quad (51)$$

Thus,

$$\begin{aligned} N(t) &= \frac{N_0}{\Gamma(\alpha)} \int_{\kappa}^{\infty} (R-\kappa)^{\alpha-1} \left[ \frac{H}{H+R} \right] [1 - e^{-(H+R)t}] dR \\ &= \frac{N_0}{\Gamma(\alpha)} \int_{\kappa}^{\infty} (R-\kappa)^{\alpha-1} H \int_0^t e^{-(R+H)t'} dt' dR \\ &= \frac{N_0}{\Gamma(\alpha)} \int_0^t H \int_{\kappa}^{\infty} (R-\kappa)^{\alpha-1} e^{-(R+H)t'} dR dt' \\ &= \frac{N_0}{\Gamma(\alpha)} \int_0^t H e^{-(\kappa+H)t'} \int_{\kappa}^{\infty} (R-\kappa)^{\alpha-1} e^{-(R-\kappa)t'} dR dt' \end{aligned}$$

This is a Laplace transform, when  $R=\kappa$ ,  $(R-\kappa)=0$

$$\begin{aligned} &= N_0 \int_0^t H e^{-(\kappa+H)t'} (1/t')^{\alpha} dt' \\ &= N_0 \frac{H}{(H+\kappa)^{1-\alpha}} \int_0^t e^{-(\kappa+H)t'} \frac{d[(H+\kappa)t']}{[(H+\kappa)t']^{\alpha}} \end{aligned}$$

And the integral is the incomplete gamma function, arguments  $1-\alpha$  and  $(H+\kappa)t$ .

$$= N_0 \frac{H}{(H+\kappa)^{1-\alpha}} \gamma[1-\alpha, (H+\kappa)t] \quad (37)$$

For  $\kappa=0$  Equation 37 becomes

$$N(t) = N_0 H^\alpha \gamma(1-\alpha, Ht) \quad (24)$$

In the Equation 38 case the same trick is used.

$$\begin{aligned} N(t) &= \frac{N_0}{\Gamma(\alpha)} \int_{\kappa}^{\infty} (R-\kappa)^{\alpha-1} \left( \frac{H}{H+R} \right) [1 - e^{-(H+R)t}] e^{-Rt} dR \\ &= \frac{N_0 H}{\Gamma(\alpha)} \int_{\kappa}^{\infty} (R-\kappa)^{\alpha-1} e^{-Rt} \int_0^t e^{-(R+H)t'} dt' dR \\ &= \frac{N_0 H}{\Gamma(\alpha)} \int_0^t \int_{\kappa}^{\infty} (R-\kappa)^{\alpha-1} e^{-Rt - (R+H)t'} dR dt' \\ &= \frac{N_0 H}{\Gamma(\alpha)} \int_0^t e^{-Ht'} \int_{\kappa}^{\infty} (R-\kappa)^{\alpha-1} e^{-R(t+t')} dR dt' \\ &= \frac{N_0 H}{\Gamma(\alpha)} \int_0^t e^{-Ht'} e^{-\kappa(t+t')} \int_{\kappa}^{\infty} (R-\kappa)^{\alpha-1} e^{-(R-\kappa)(t+t')} d(R-\kappa) dt' \end{aligned}$$

Again this a Laplace transform, replace  $R-\kappa$  with a single variable going from 0 to  $\infty$ .

$$= N_0 H \int_0^r e^{-Ht'} e^{-\kappa(t+t')} (t+t')^{-\alpha} dt'$$

$$= N_0 H e^{Ht} \int_0^r e^{-(H+\kappa)(t+t')} (t+t')^{-\alpha} dt'$$

Substitute  $t''=t+t'$ ,  $r \rightarrow t+r$ , and  $0 \rightarrow t$

$$= N_0 H e^{Ht} \int_t^{t+r} e^{-(H+\kappa)t''} t''^{-\alpha} dt''$$

The integral can now be seen to be the difference of two integrals,  $0 \rightarrow t+r$  less  $0 \rightarrow t$ .

$$= N_0 \frac{H}{(H+\kappa)^{1-\alpha}} e^{Ht} \int_t^{t+r} e^{-(H+\kappa)t''} [(H+\kappa)t'']^{-\alpha} d[(H+\kappa)t'']$$

Let  $\omega = [(H+\kappa)t'']$ ,  $d\omega = (H+\kappa)dt''$ ,  $t+r \rightarrow (H+\kappa)(t+r)$ , and  $t \rightarrow (H+\kappa)t$ .

$$= N_0 \frac{H}{(H+\kappa)^{1-\alpha}} e^{Ht} \int_{(H+\kappa)t}^{(H+\kappa)(t+r)} \omega^{-\alpha} e^{-\omega} d\omega$$

Thus

$$= N_0 \frac{H}{(H+\kappa)^{1-\alpha}} e^{Ht} \{ \gamma[1-\alpha, (H+\kappa)(t+r)] - \gamma[1-\alpha, (H+\kappa)t] \} \quad (38)$$

For  $\kappa=0$  Equation 38 becomes

$$N(t) = N_0 H^\alpha e^{Ht} [ \gamma(1-\alpha, H(t+r)) - \gamma(1-\alpha, Ht) ] \quad (27)$$

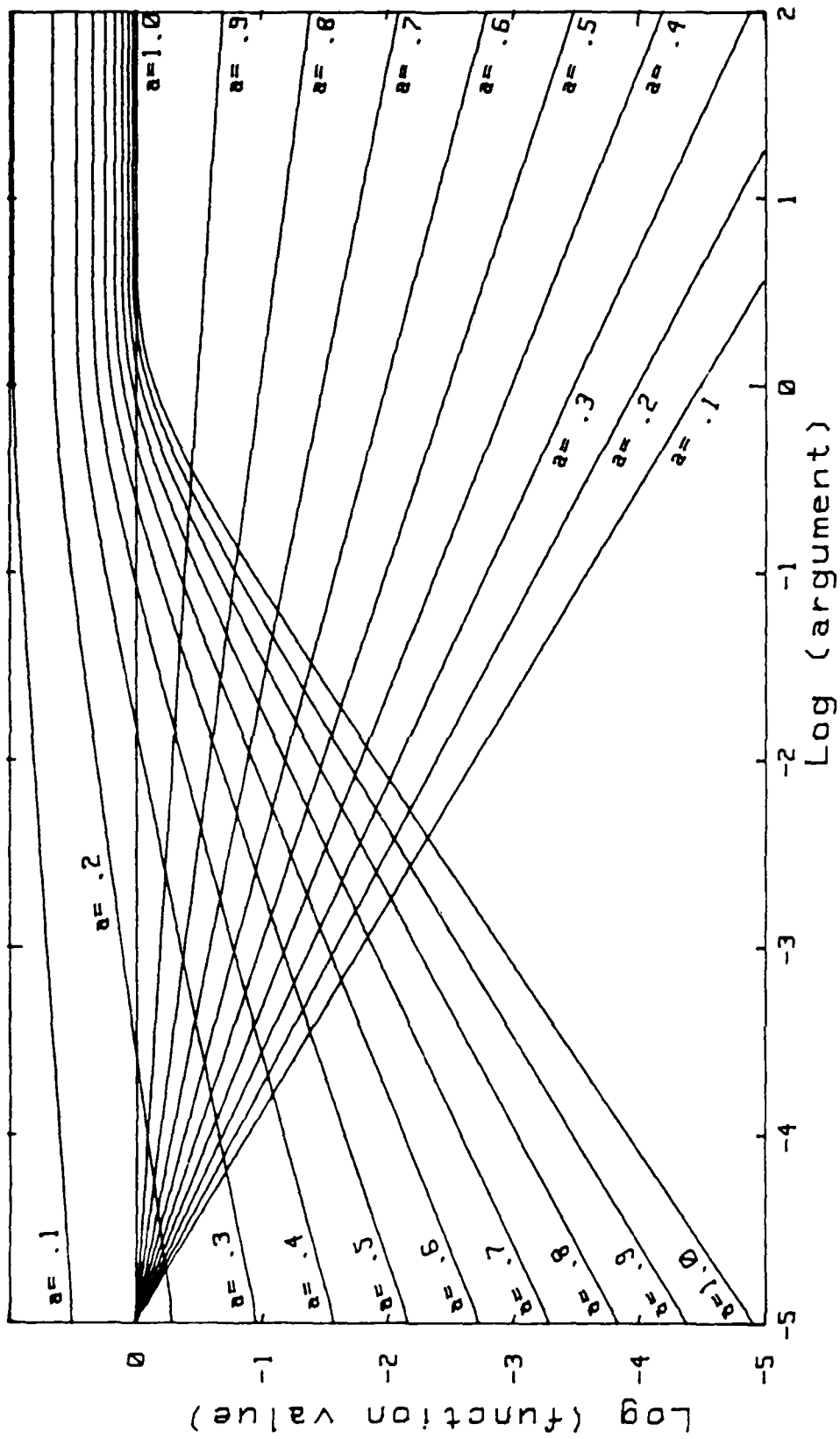


Figure 1. The incomplete gamma function, along with the associated inverse power function.

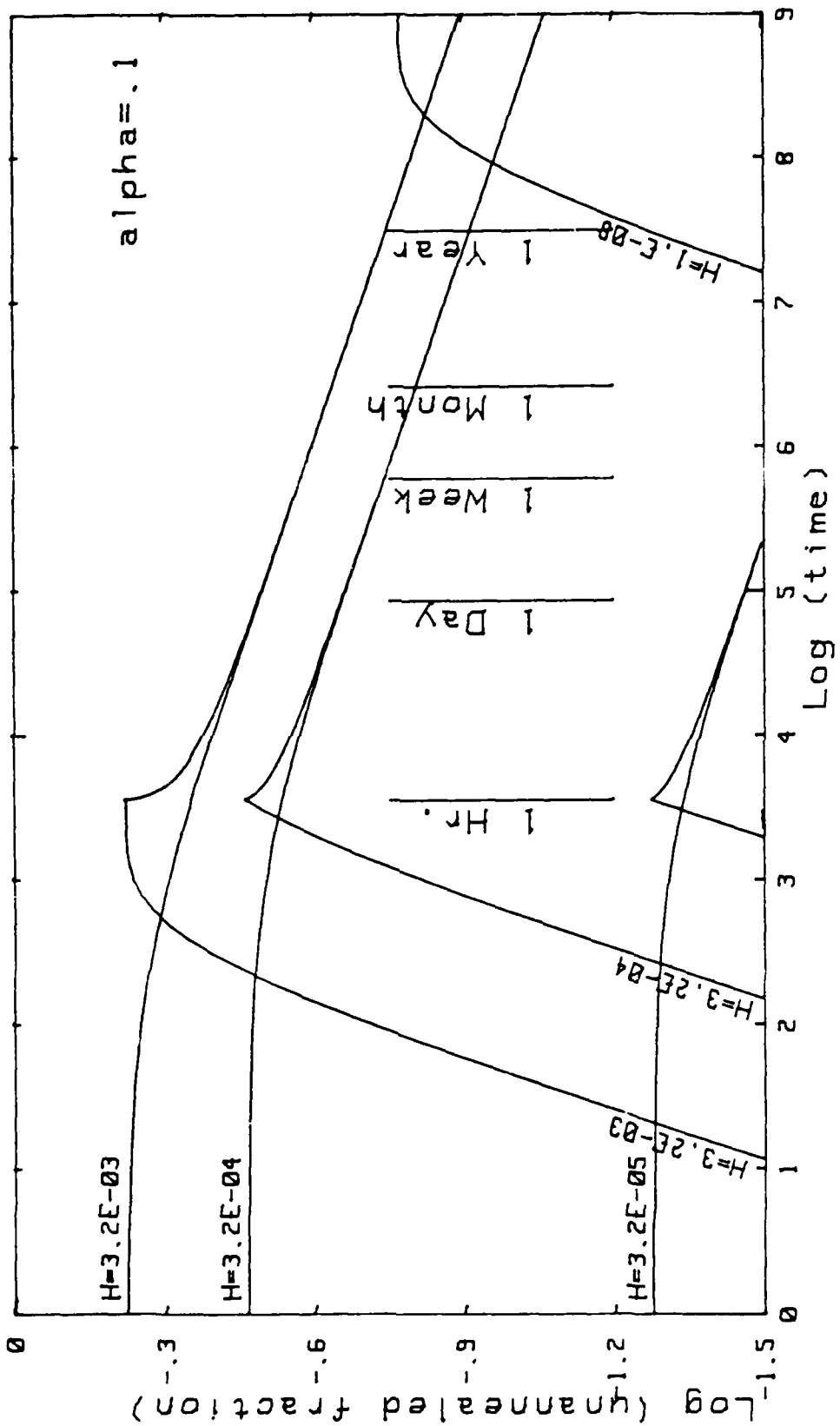


Figure 2. Simulate  $Co^{60}$  Irradiation for  $\alpha=0.1$

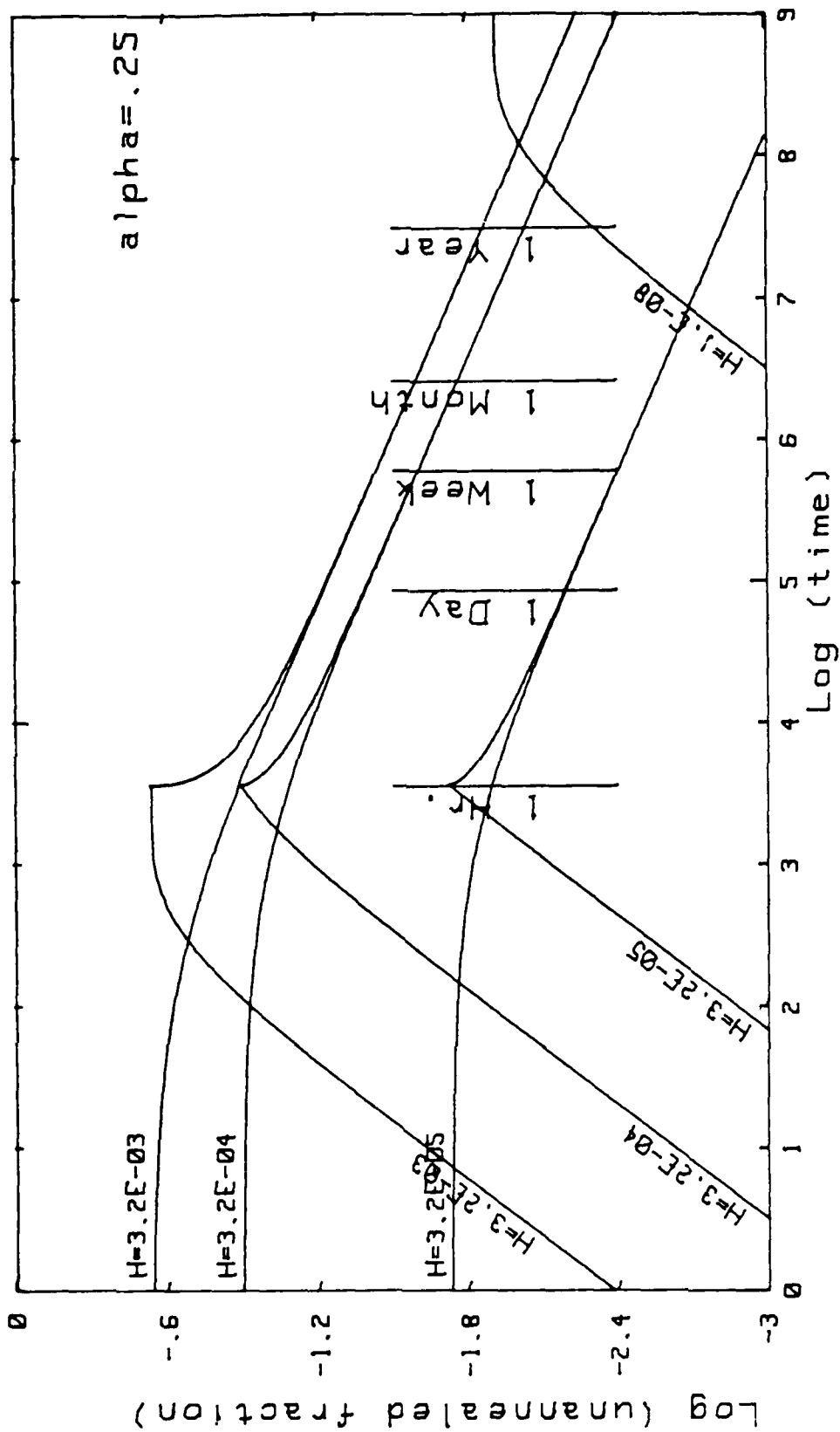


Figure 3. Simulate  $\text{Co}^{60}$  Irradiation for  $\alpha=0.25$

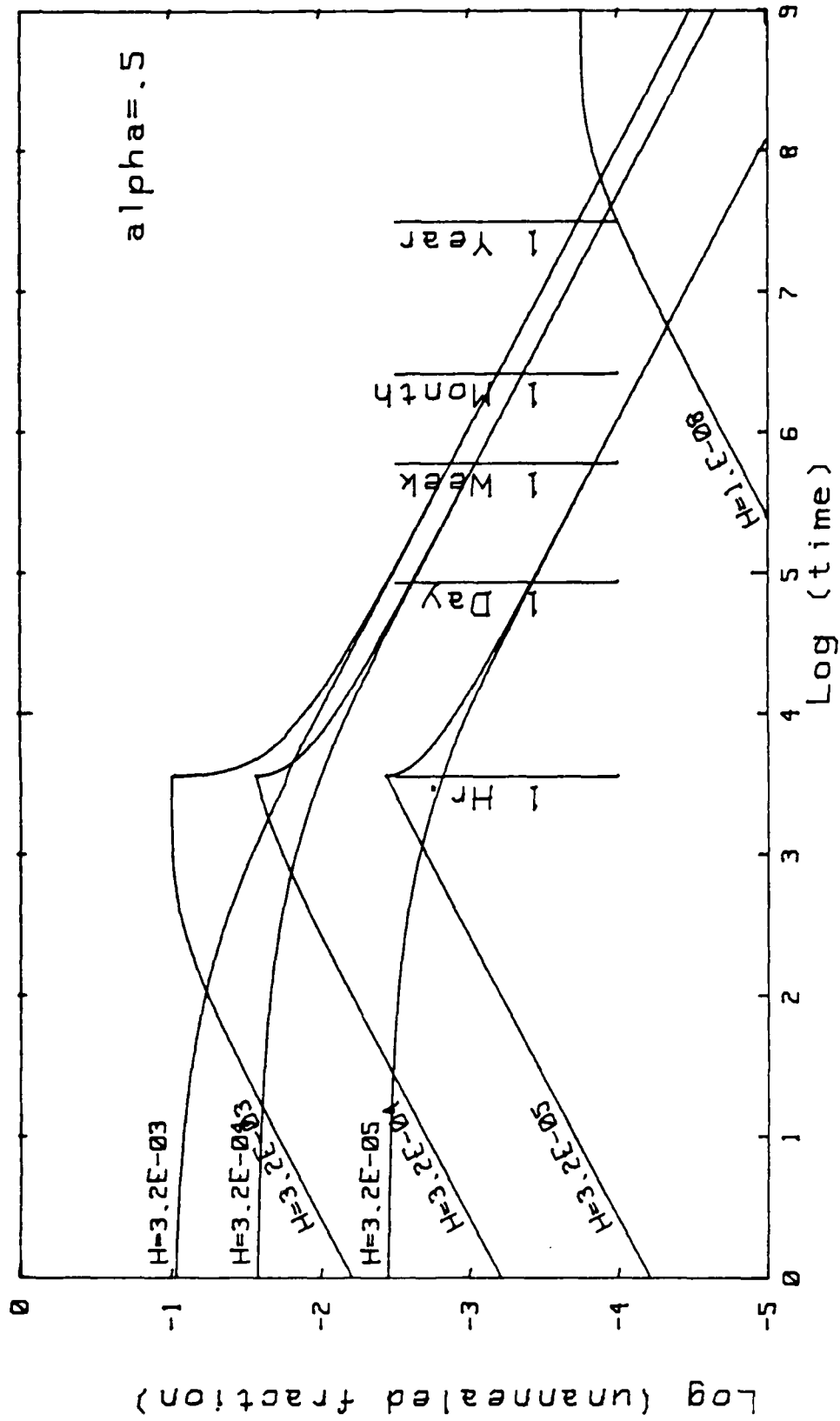


Figure 4. Simulate  $Co^{60}$  Irradiation for  $\alpha=0.5$

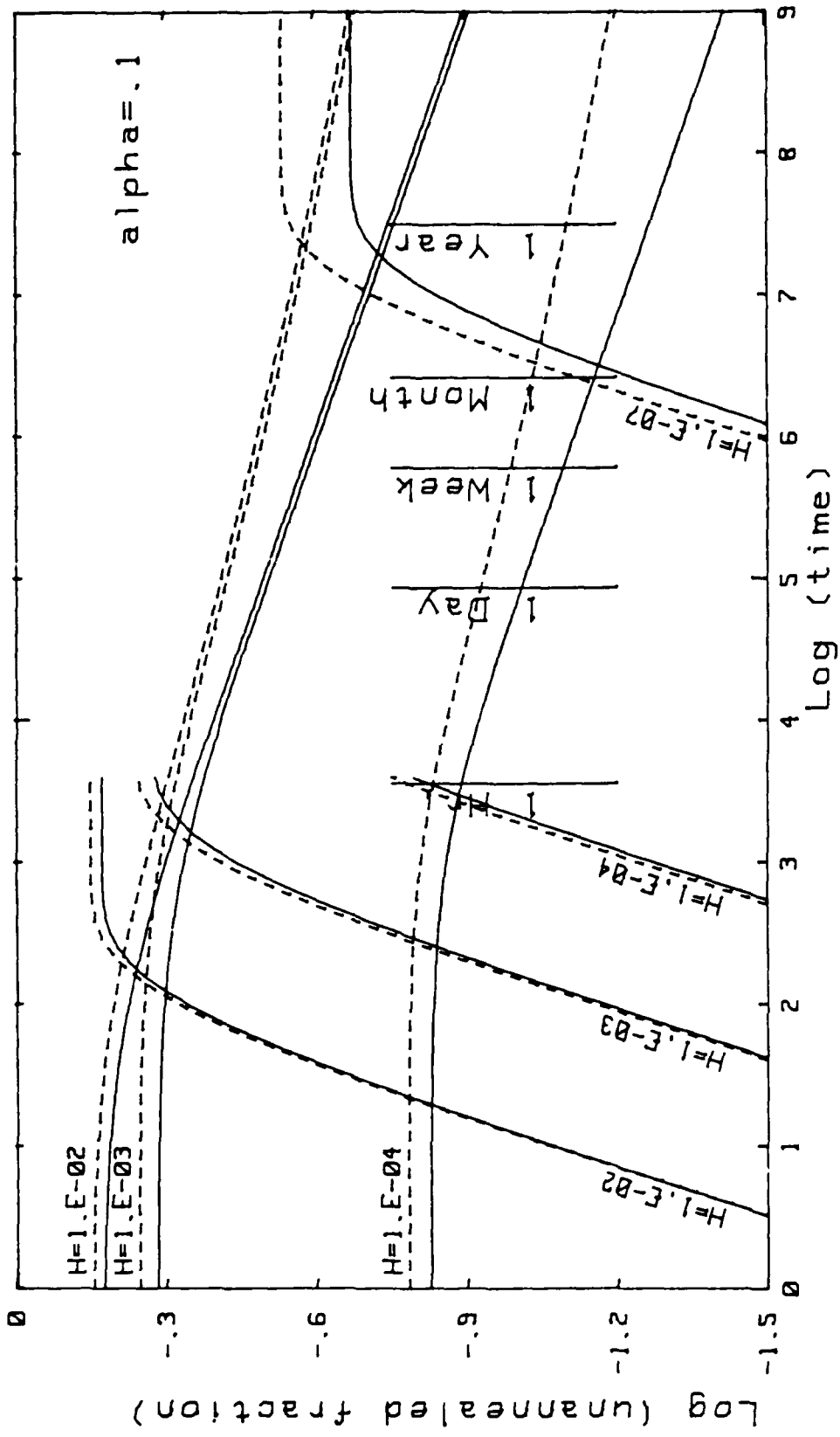


Figure 5. The error from nonannealing traps for  $\alpha=0.1$

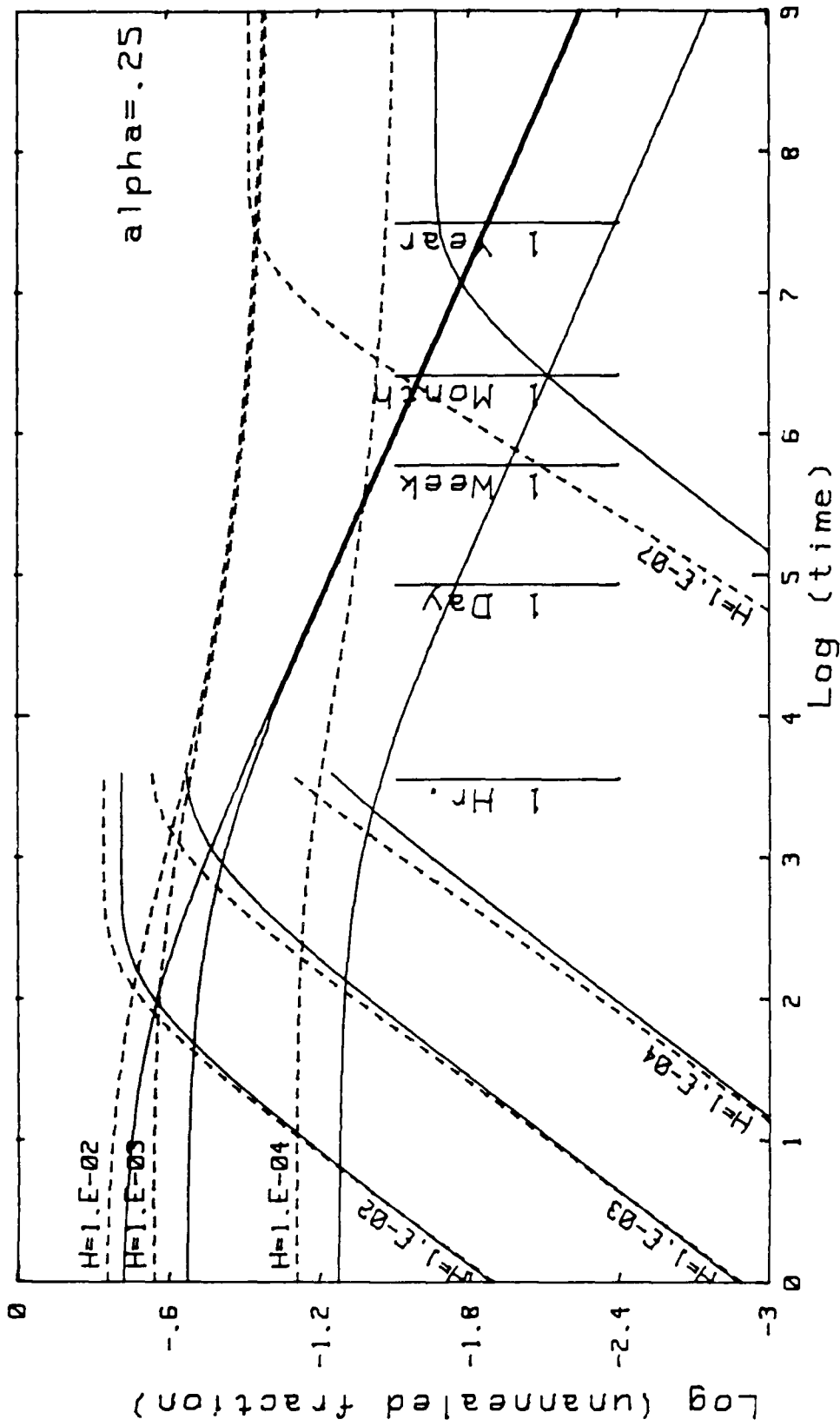


Figure 6. The error from nonannealing traps for alpha=0.25

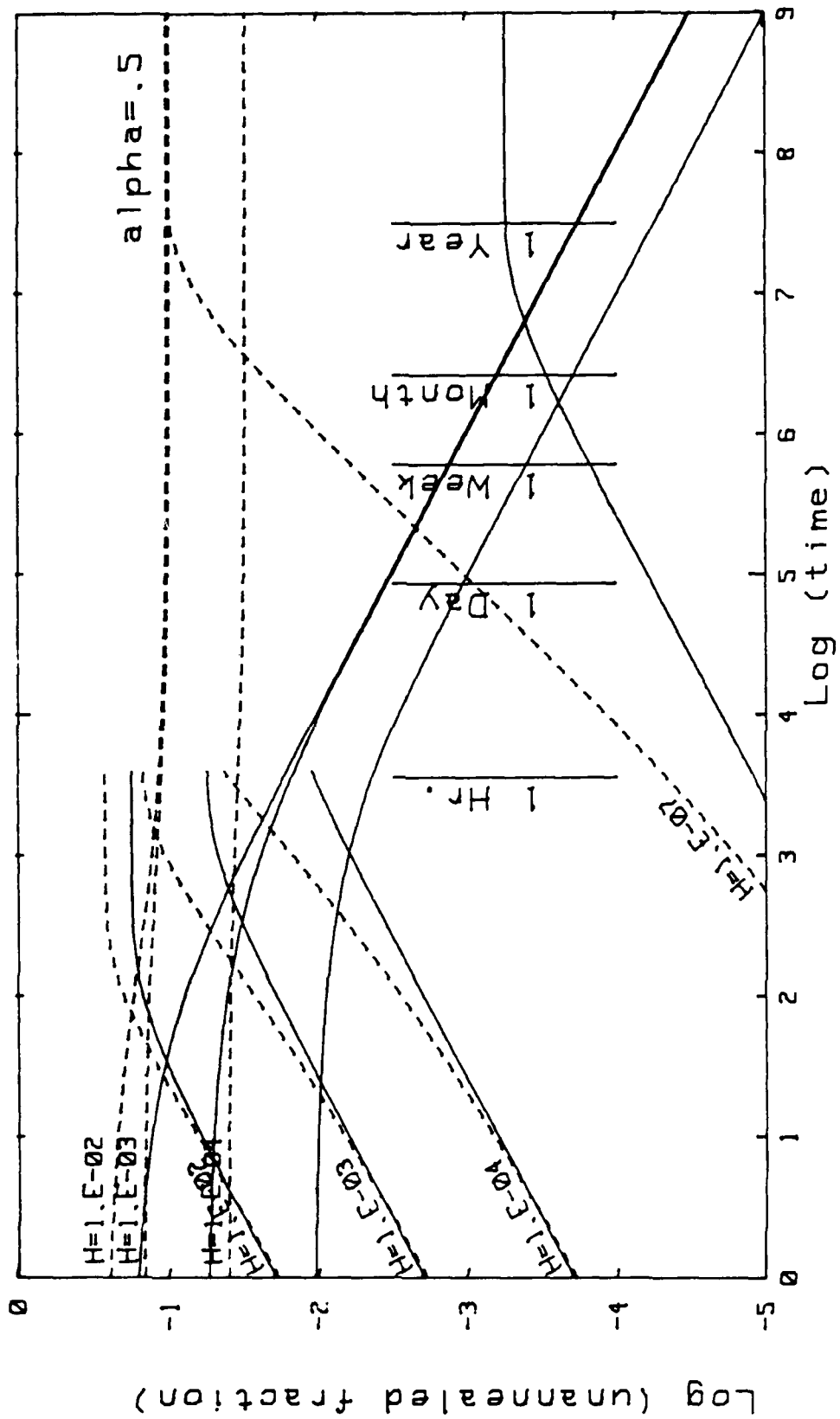


Figure 7. The error from nonannealing traps for  $\alpha=0.5$

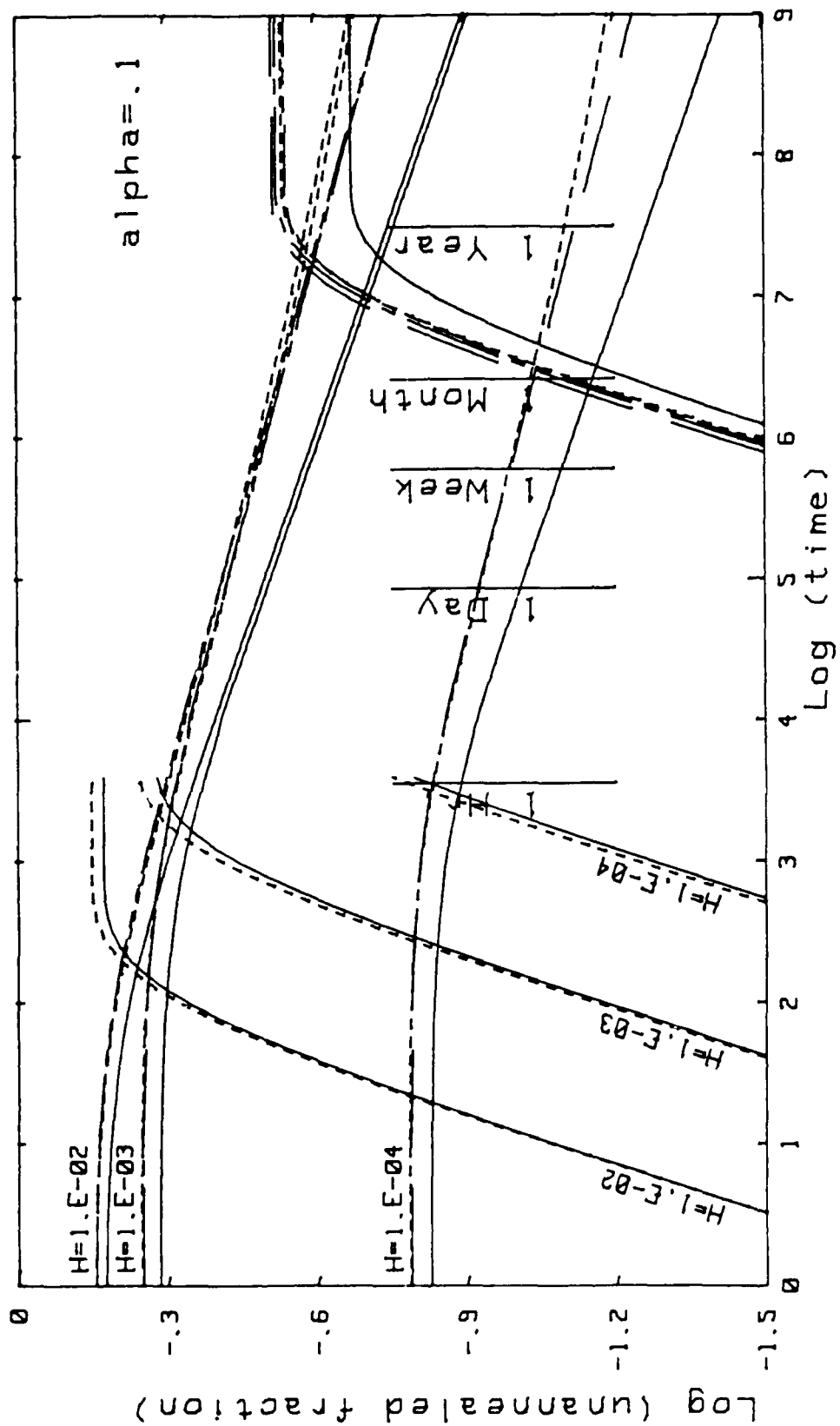


Figure 8. The error from extrapolating a curve with error from nonannealing traps for alpha=0.1

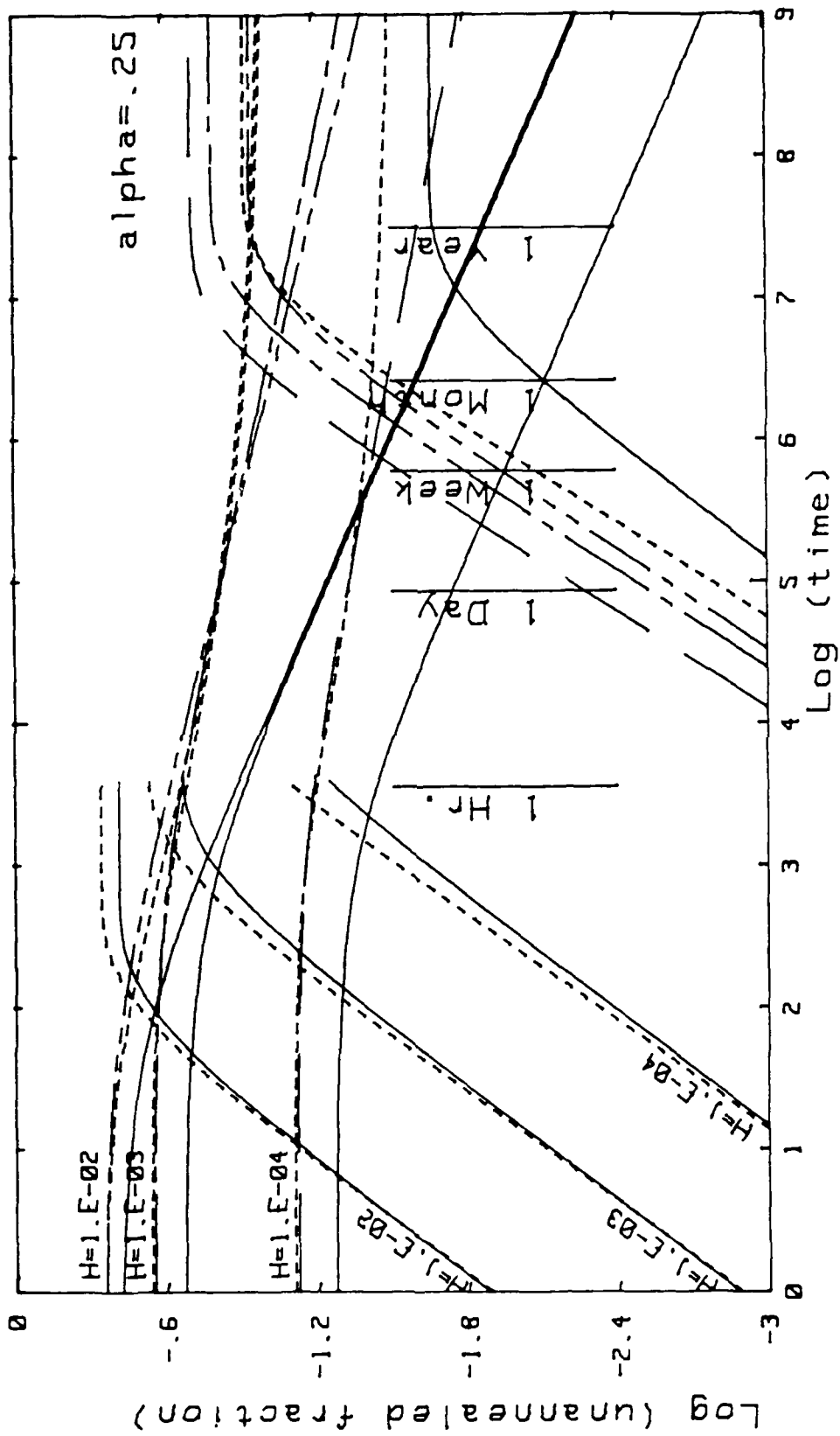


Figure 9. The error from extrapolating a curve with error from nonannealing traps for alpha=0.25

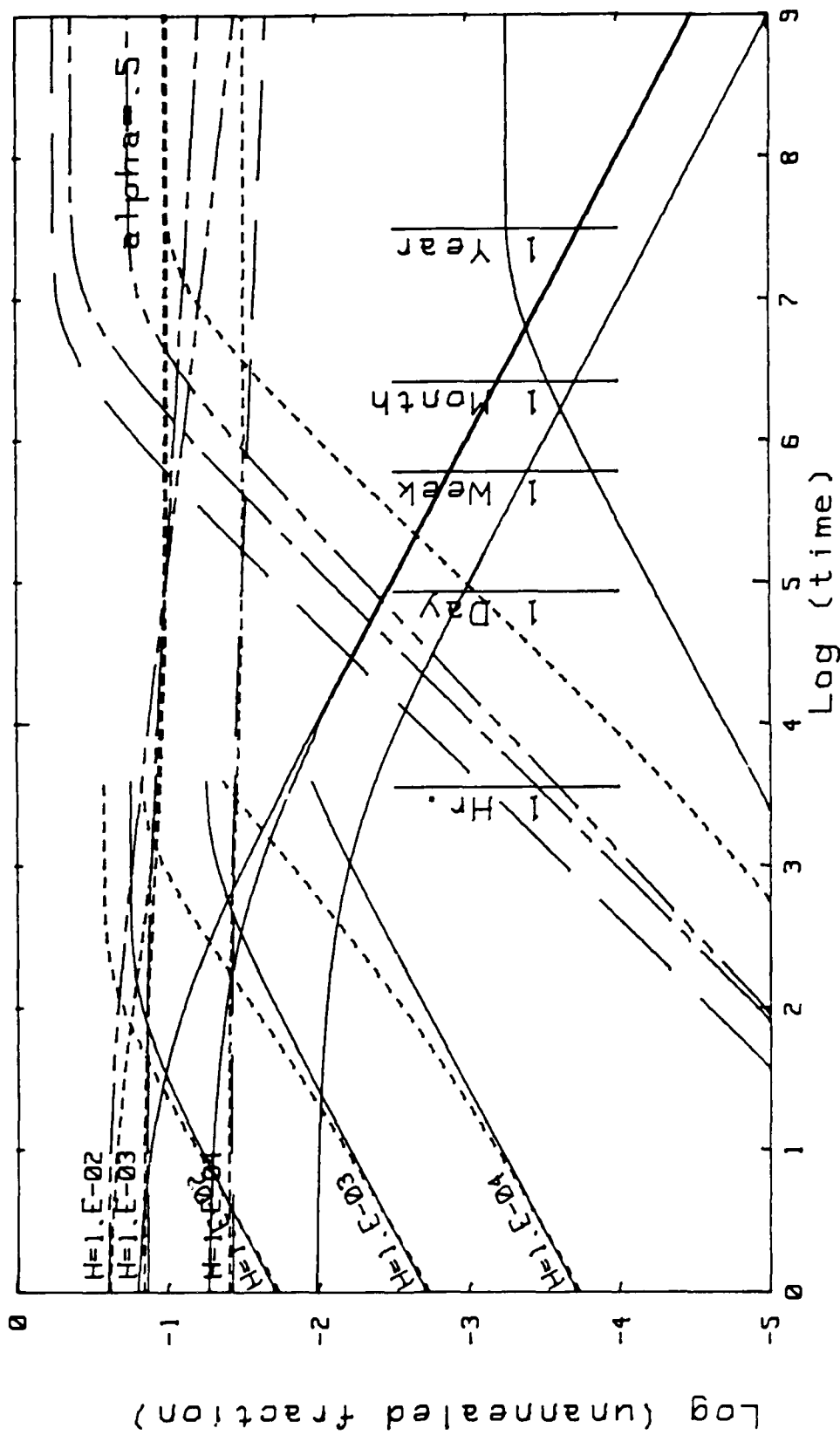


Figure 10. The error from extrapolating a curve with error from nonannealing traps for  $\alpha=0.5$

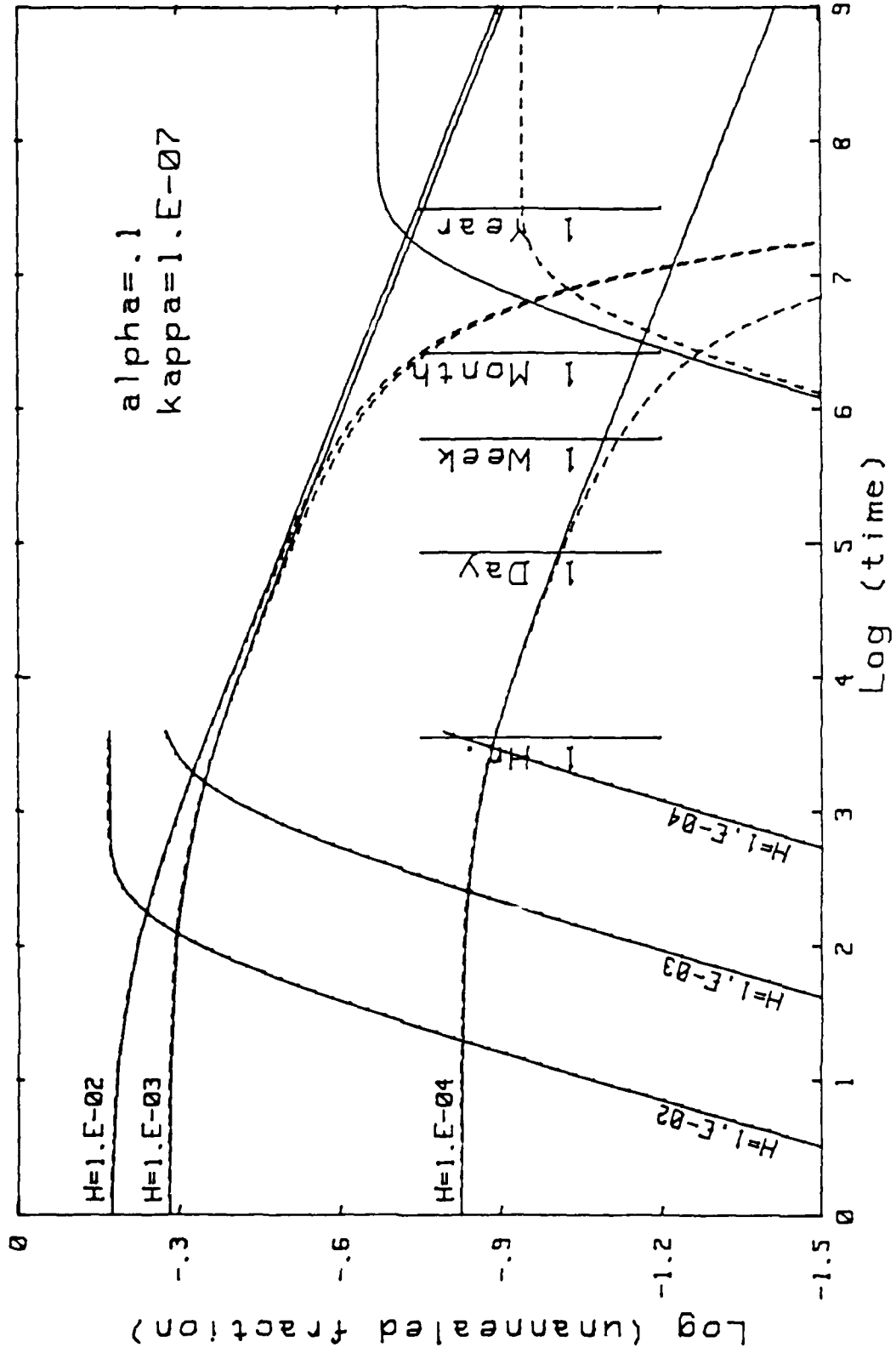


Figure 11. The error from a trap distribution with a floor for  $\alpha=0.1$  and  $\kappa=1E-7$ .

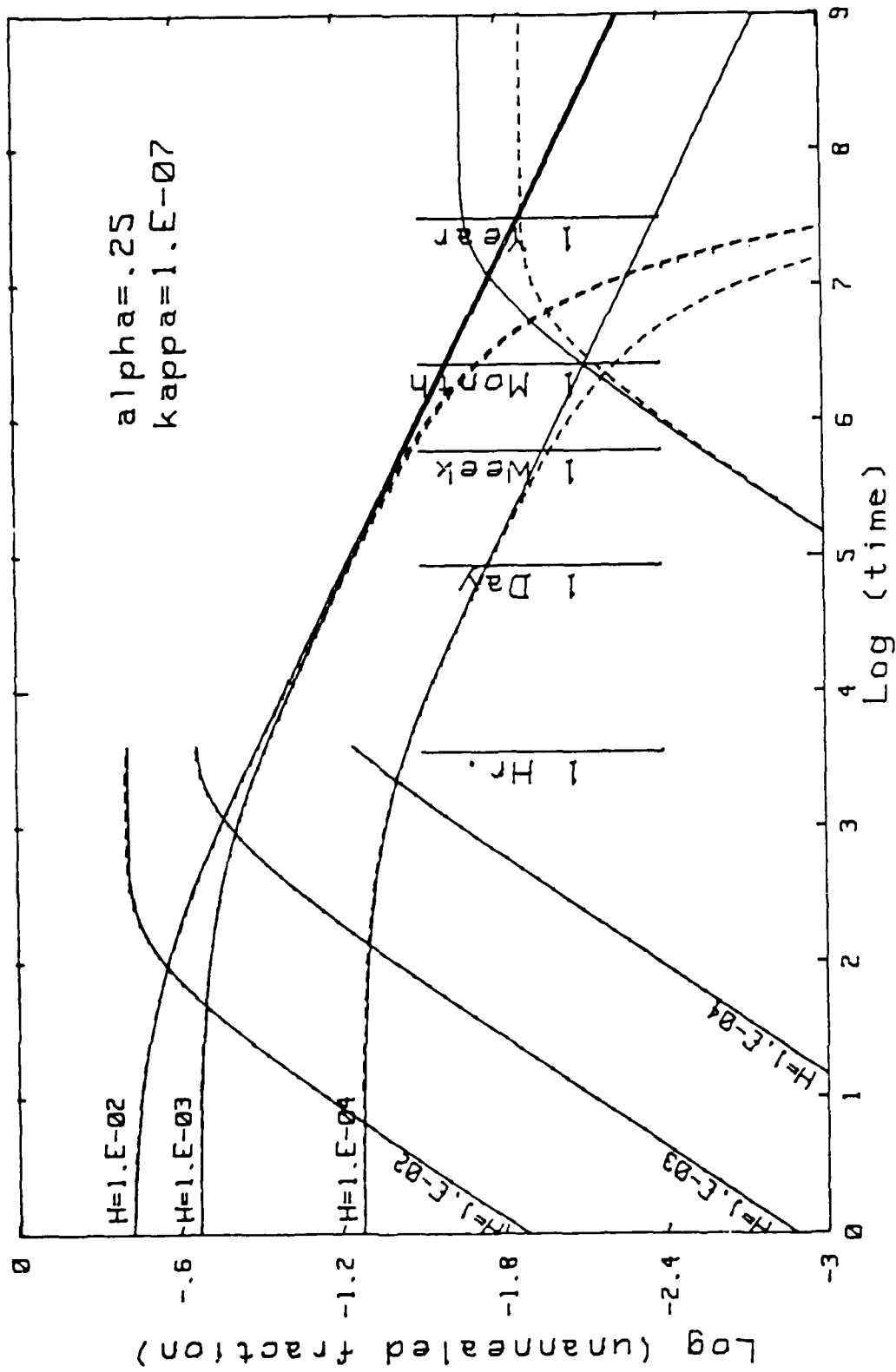


Figure 12. The error from a trap distribution with a floor for  $\alpha=0.25$  and  $\kappa=1E-7$ .

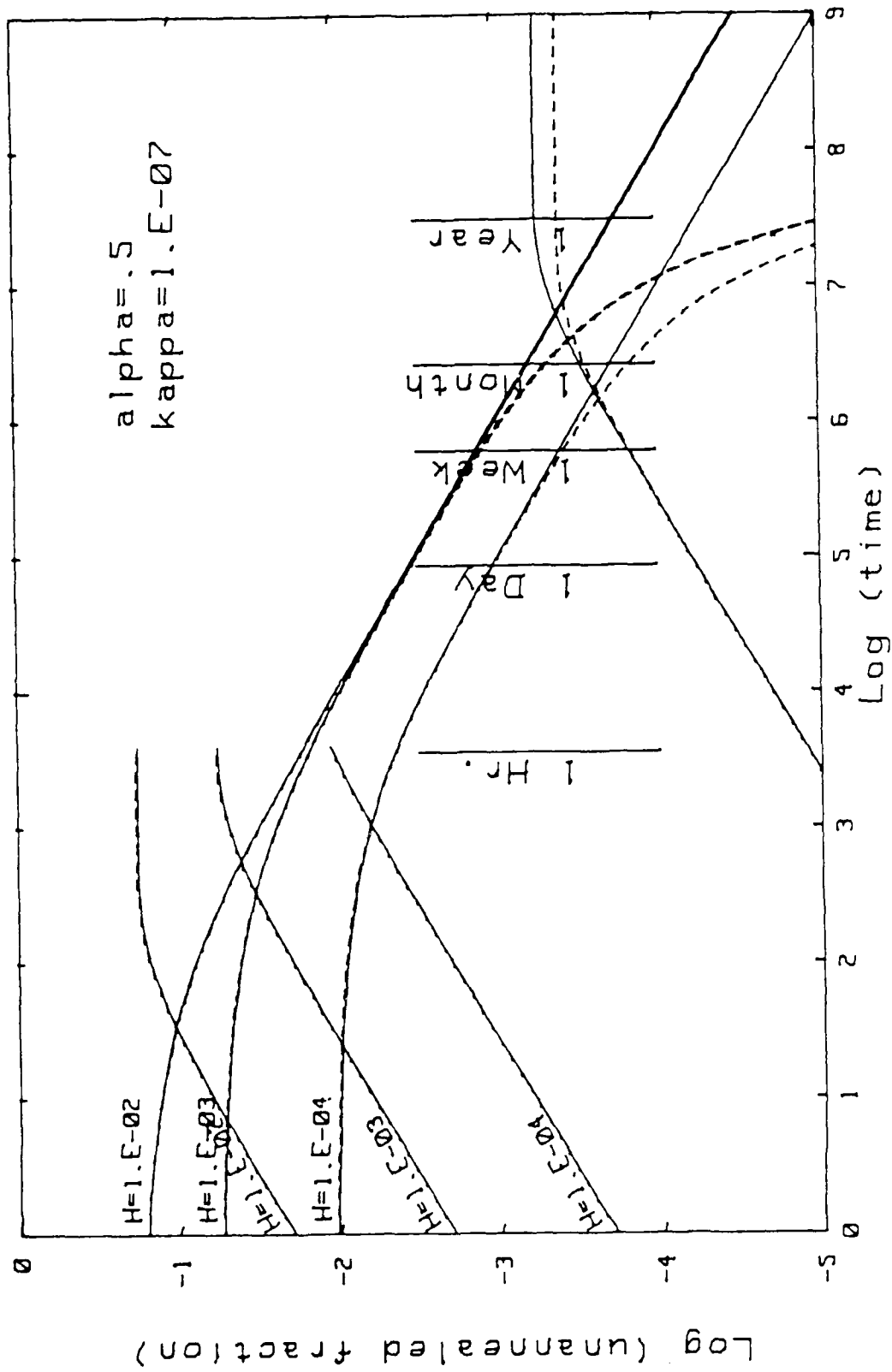


Figure 13. The error from a trap distribution with a factor for  $\alpha=0.25$  and  $\kappa=1E-7$ .



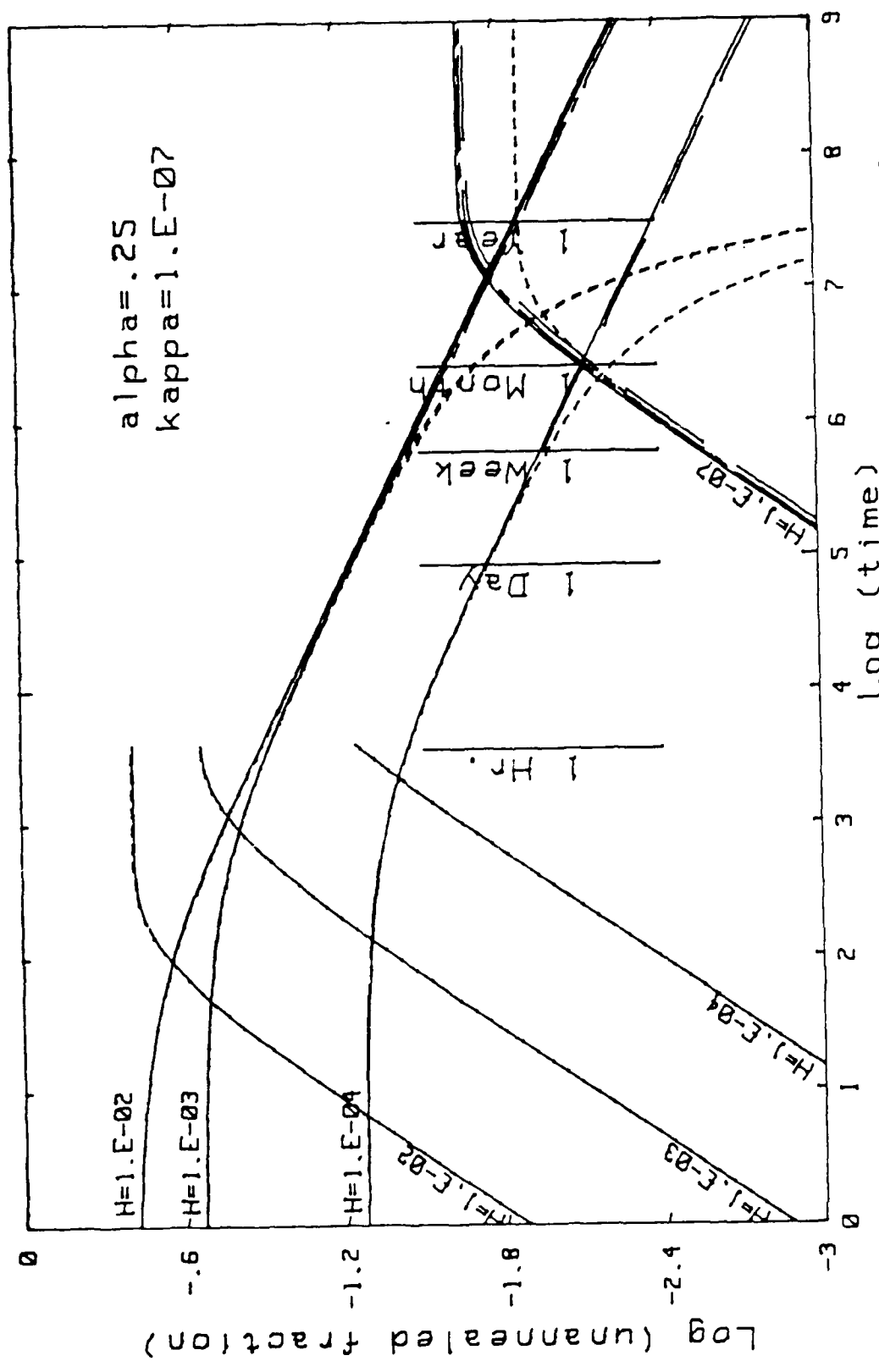


Figure 15. The extrapolation error caused by a trap distribution with a floor for  $\alpha=0.25$  and  $\kappa=1E-7$ .

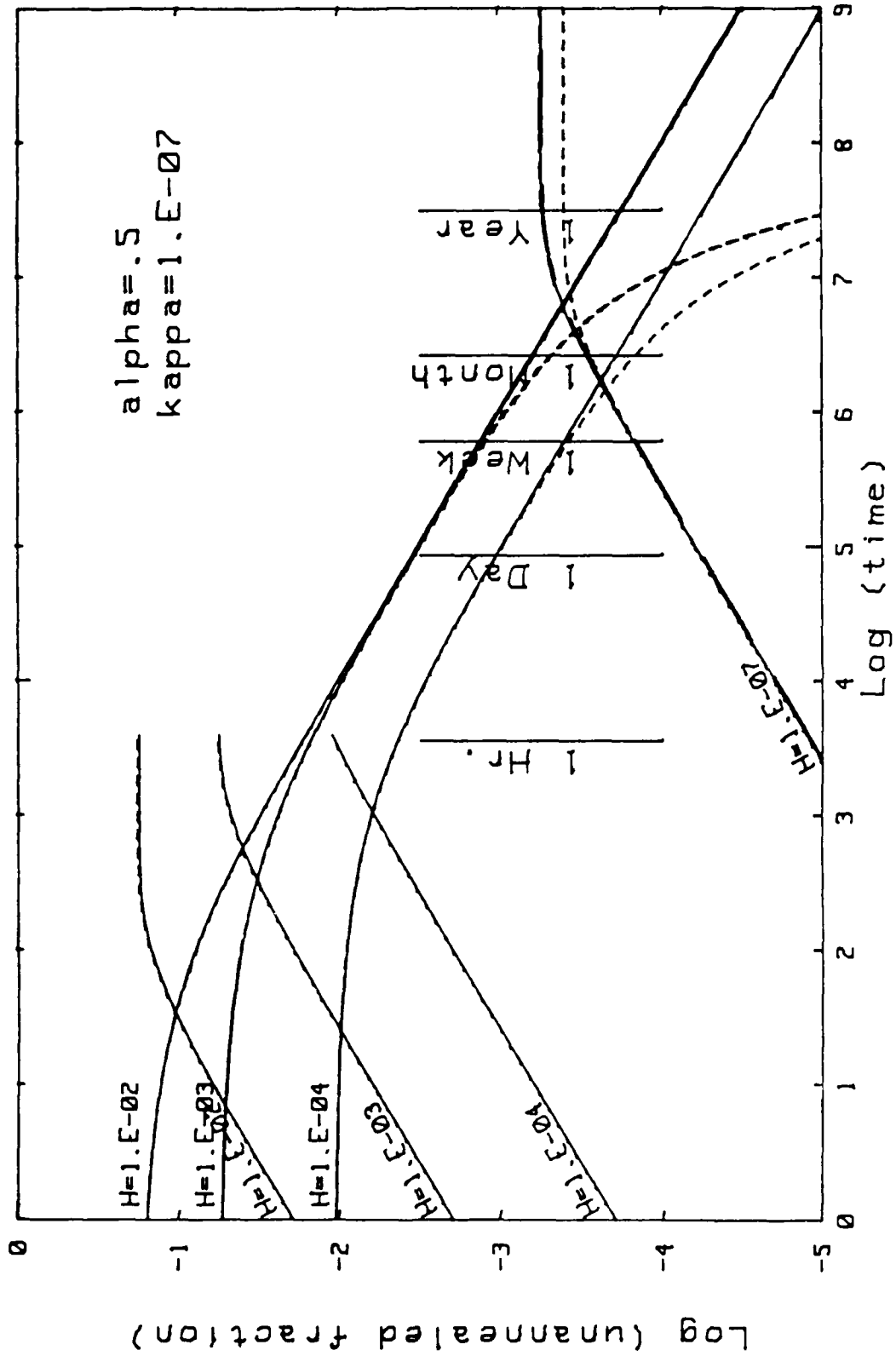


Figure 16. The extrapolation error caused by a trap distribution with a floor for  $\alpha=0.5$  and  $\kappa=1E-7$ .

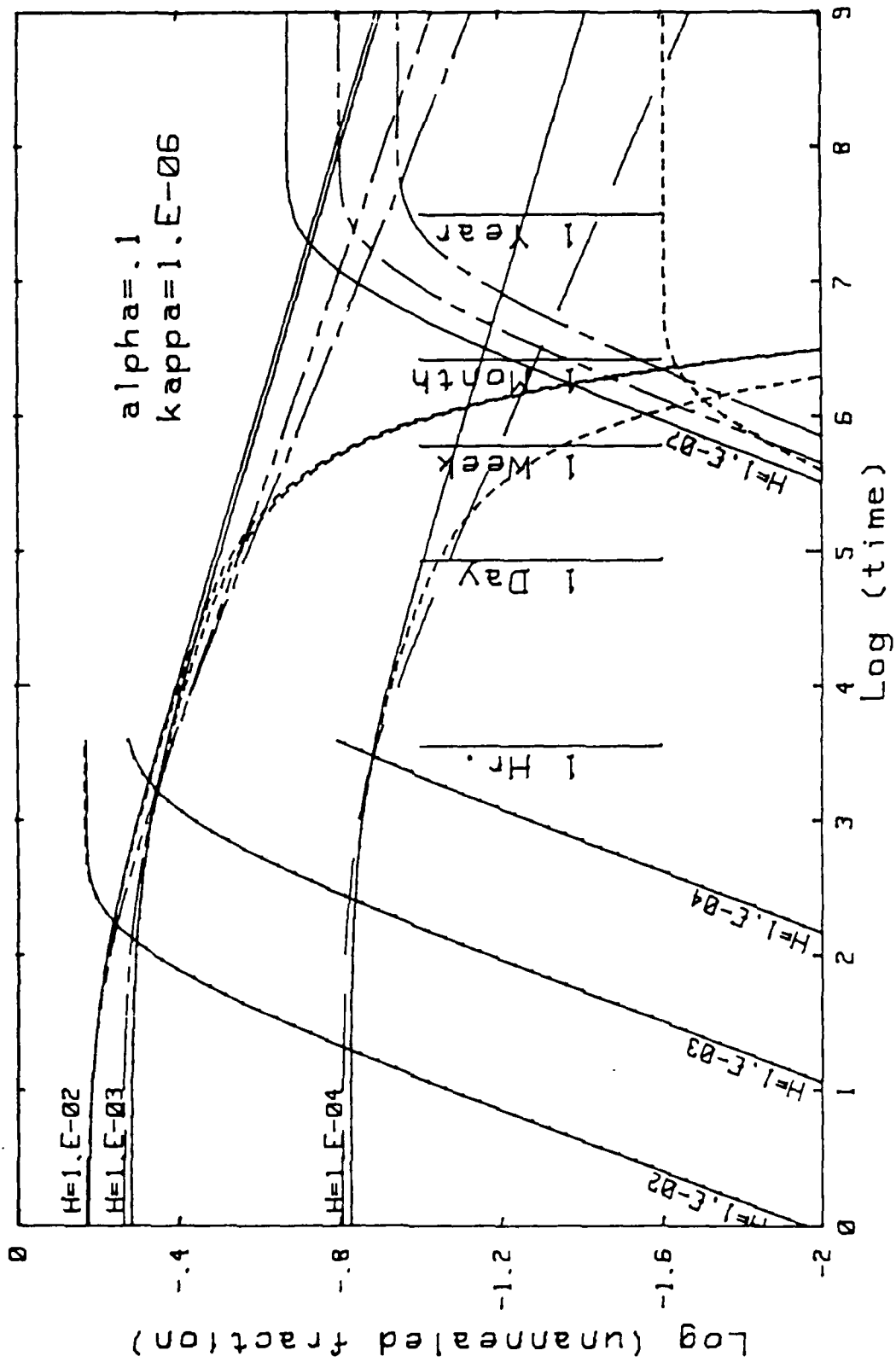


Figure 17. The extrapolation error caused by a trap distribution with a floor for  $\alpha=0.1$  and  $\kappa=1E-6$ .

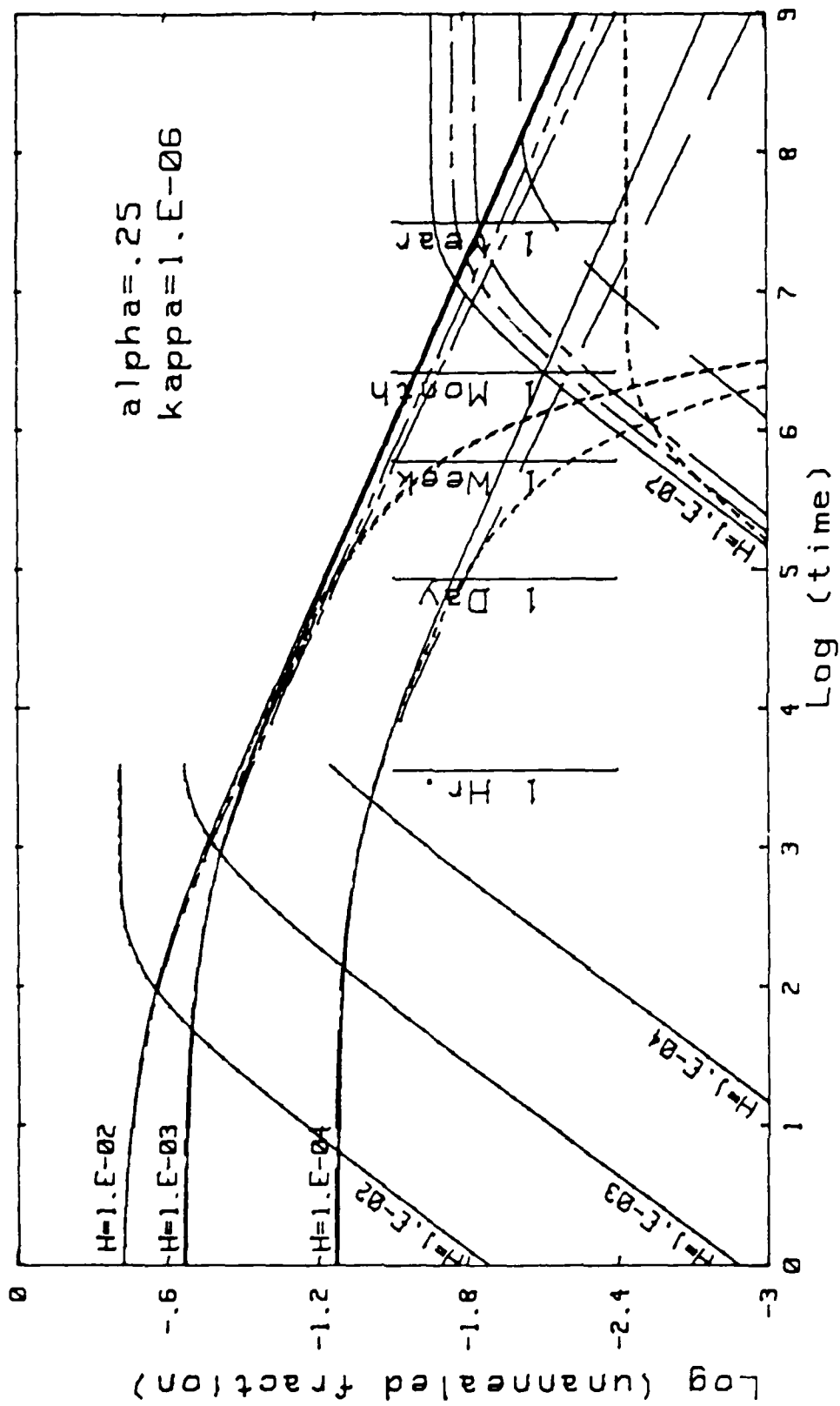


Figure 18. The extrapolation error caused by a trap distribution with a floor for  $\alpha=0.25$  and  $\kappa=1E-6$ .

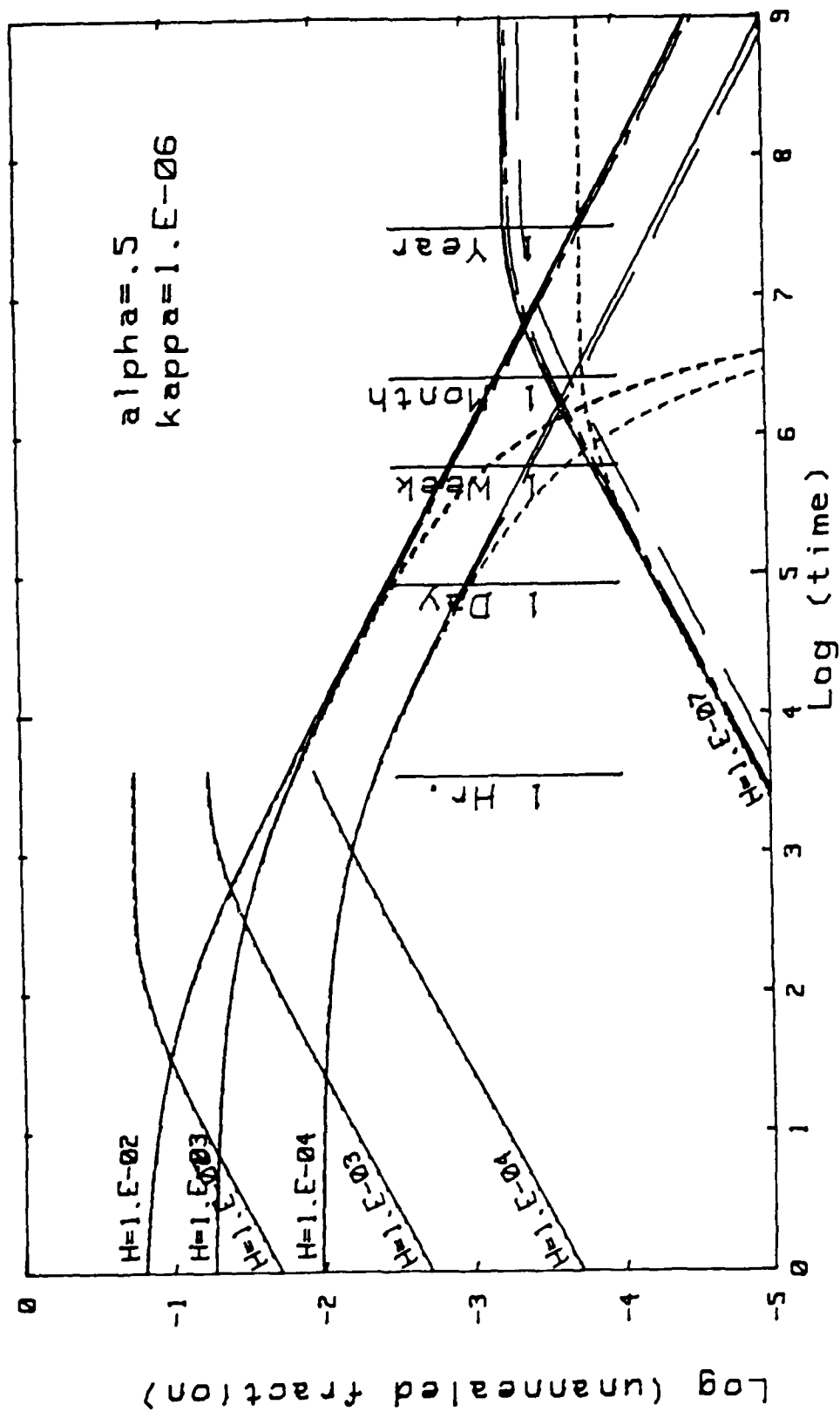


Figure 19. The extrapolation error caused by a trap distribution with a floor for  $\alpha=0.5$  and  $\kappa=1E-6$ .

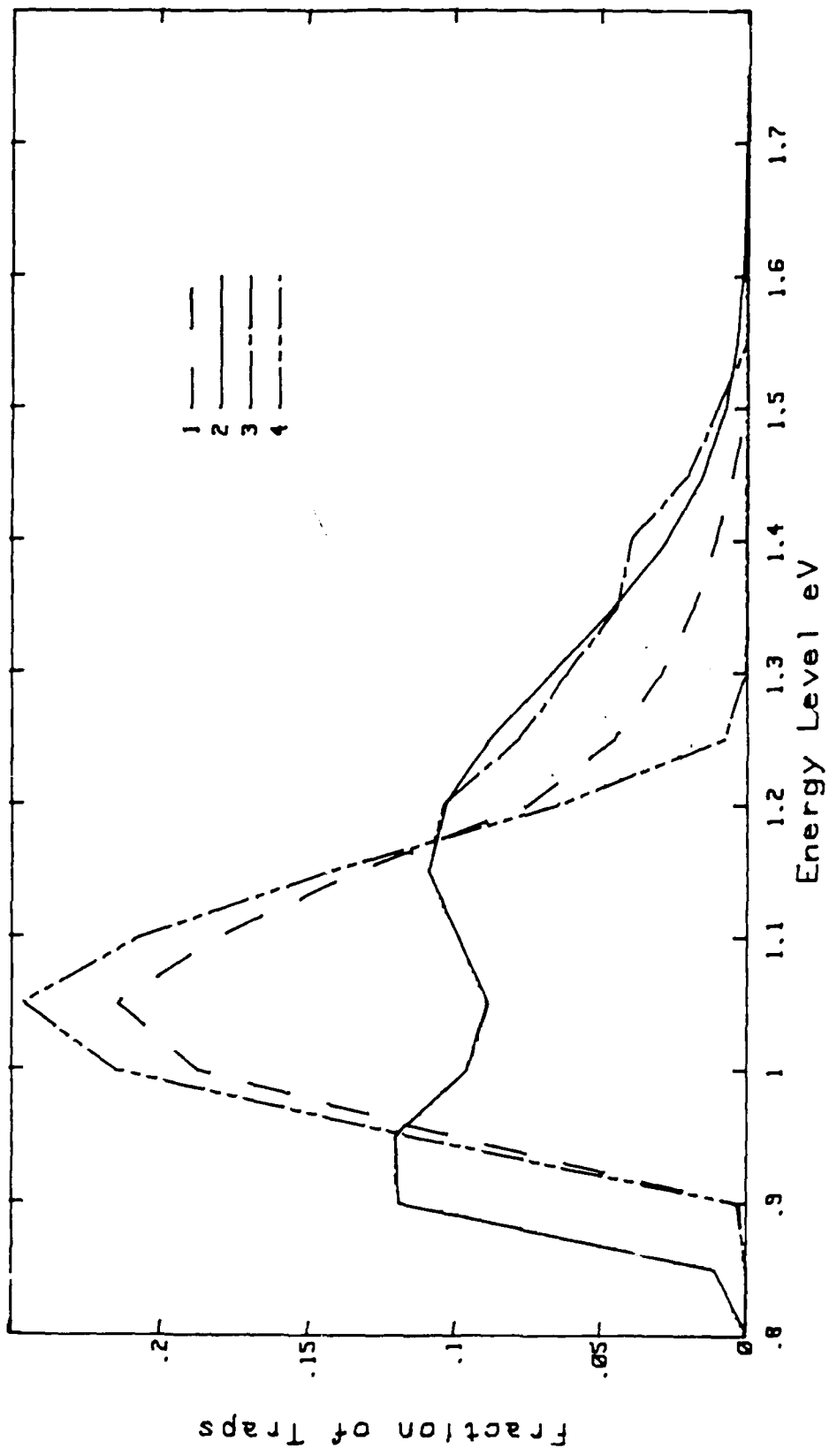


Figure 20. The energy distributions of the traps.

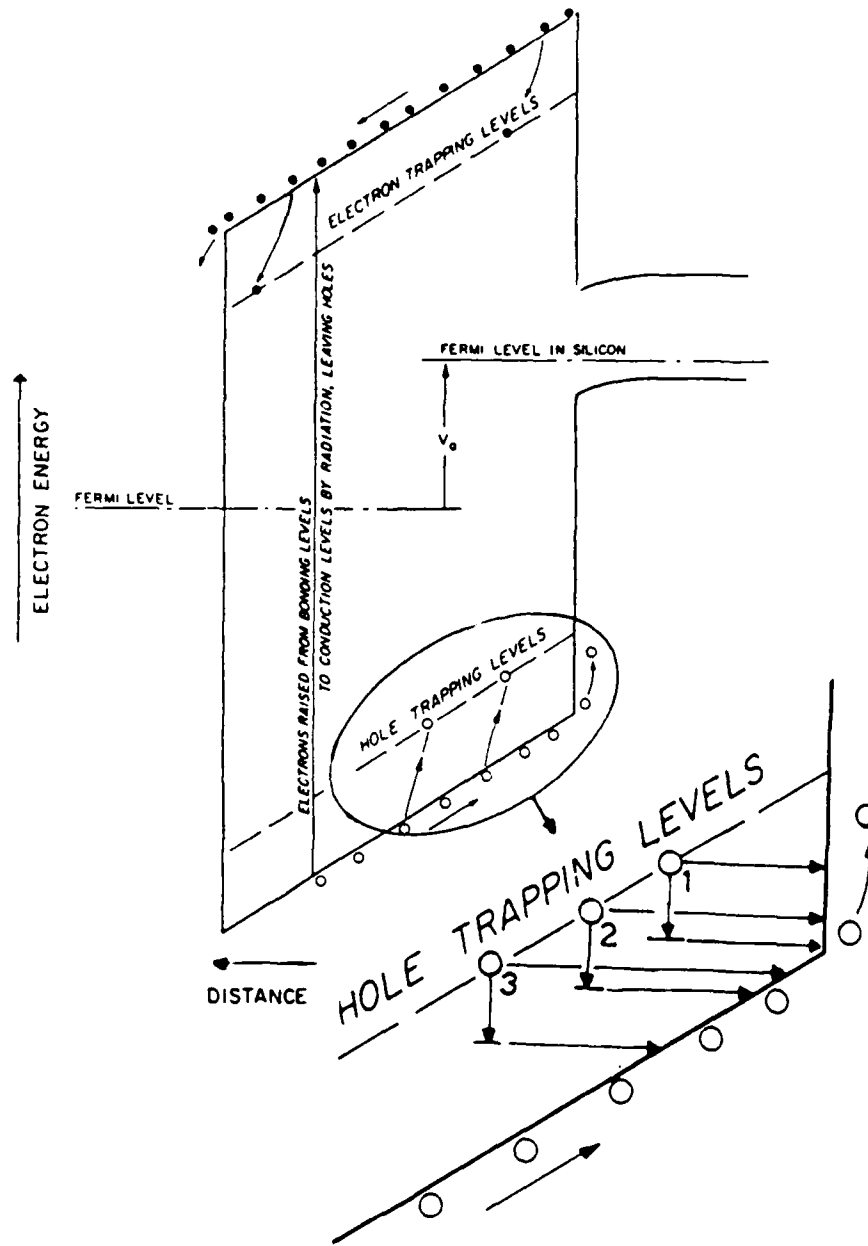


Figure 21. An energy level diagram showing the traps and their detrapping paths.

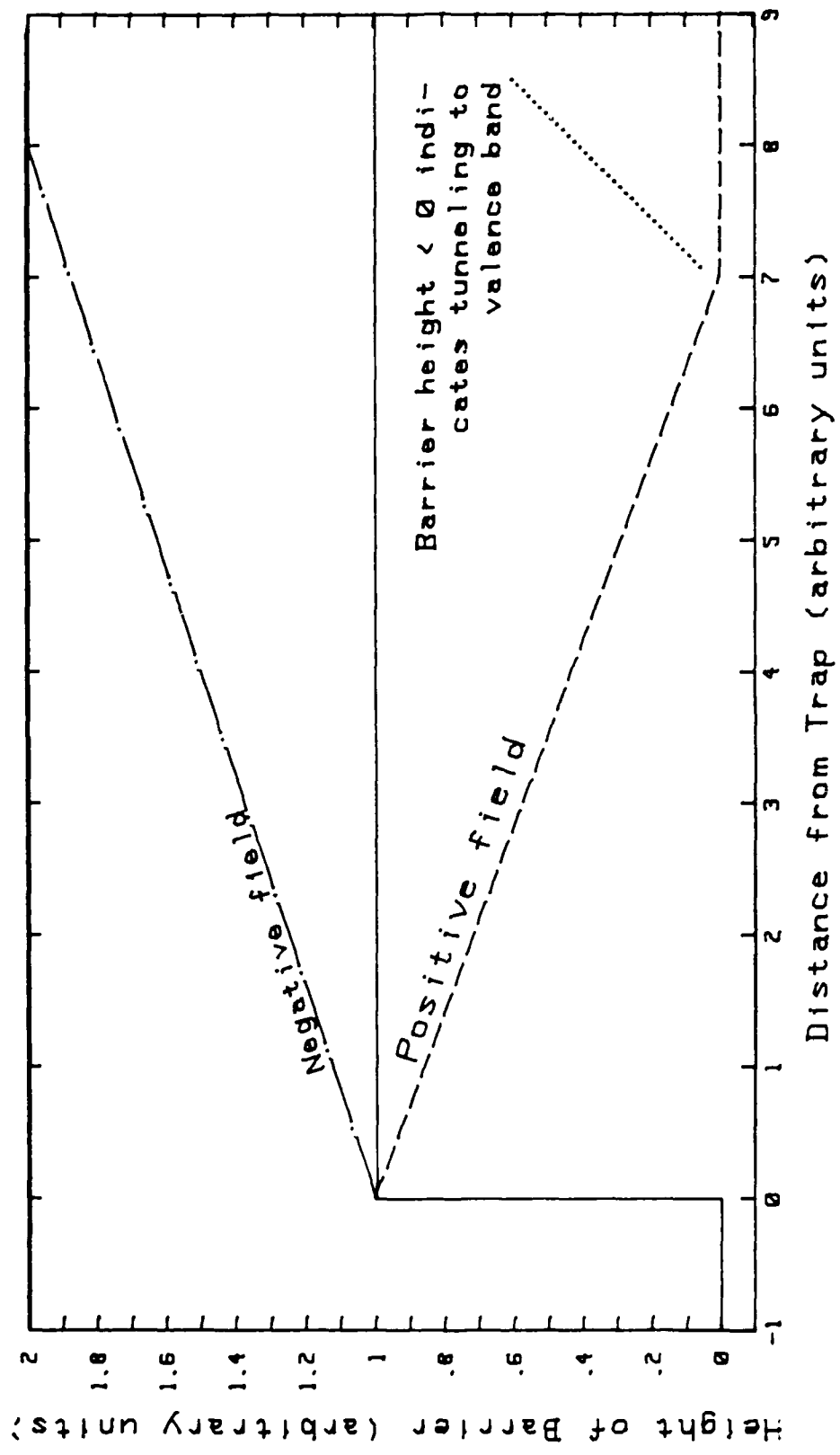


Figure 22. The tunneling barrier profile for the one-dimensional tunneling model.

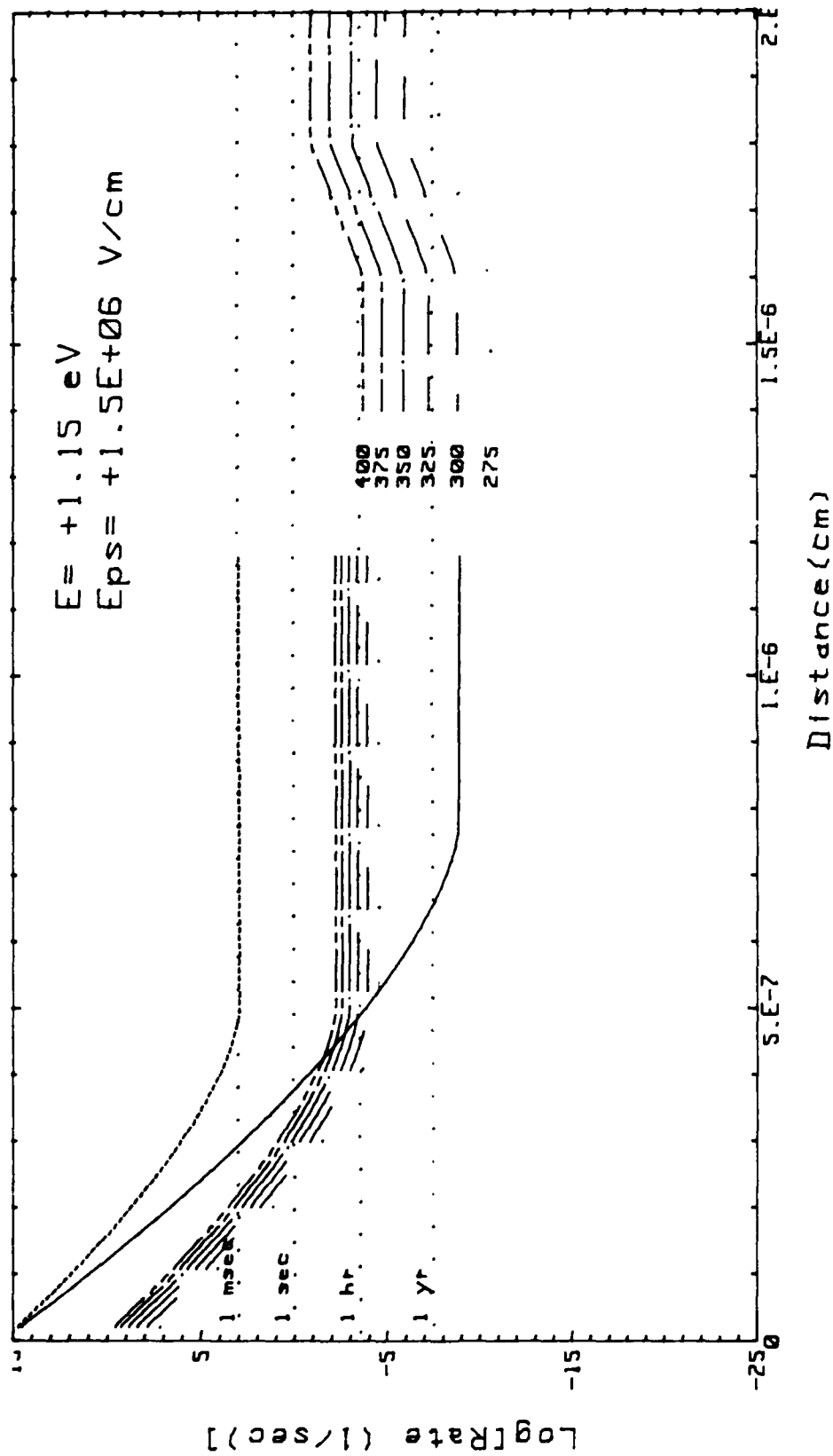


Figure 23. Partial detrapping rates; shown are partial rates from the ground state (solid line), the partial rates from the excited states are identified by temperature. The levels on the right correspond to the partial detrapping by thermal detrapping with cross sections  $1E-16$  and  $7E-14$ , respectively. Trapping energy is  $1.15 \text{ eV}$  and electric field of  $1E6 \text{ V/cm}$ .

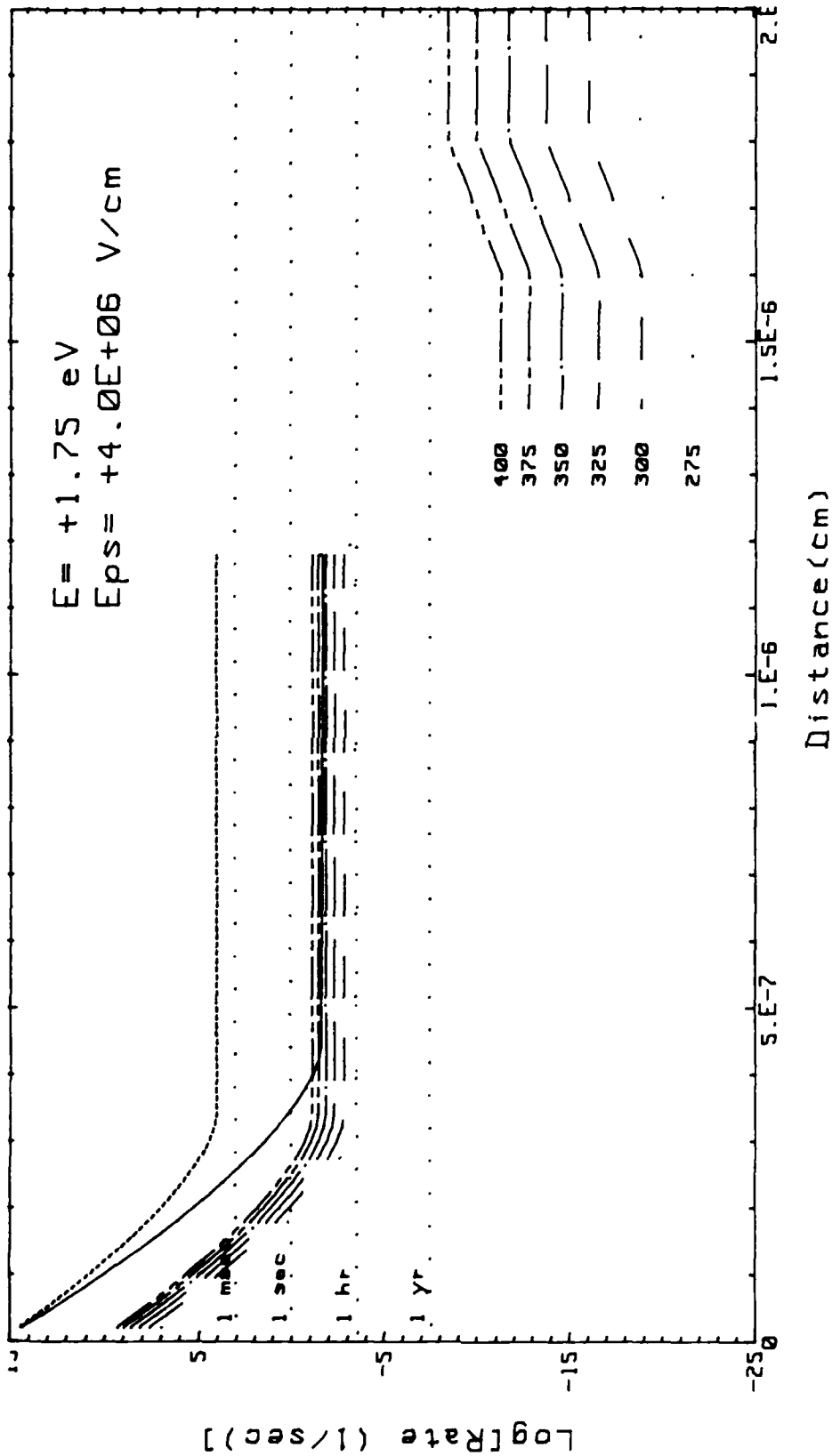


Figure 24. Partial detraping rates; shown are partial rates from the ground state (solid line), the partial rates from the excited states are identified by temperature. The levels on the right correspond to the partial detraping by thermal emission with cross sections  $1E-16$  and  $7E-14$ , respectively. Trapping energy is  $1.75 \text{ eV}$  and electric field of  $4E6 \text{ V/cm}$ .

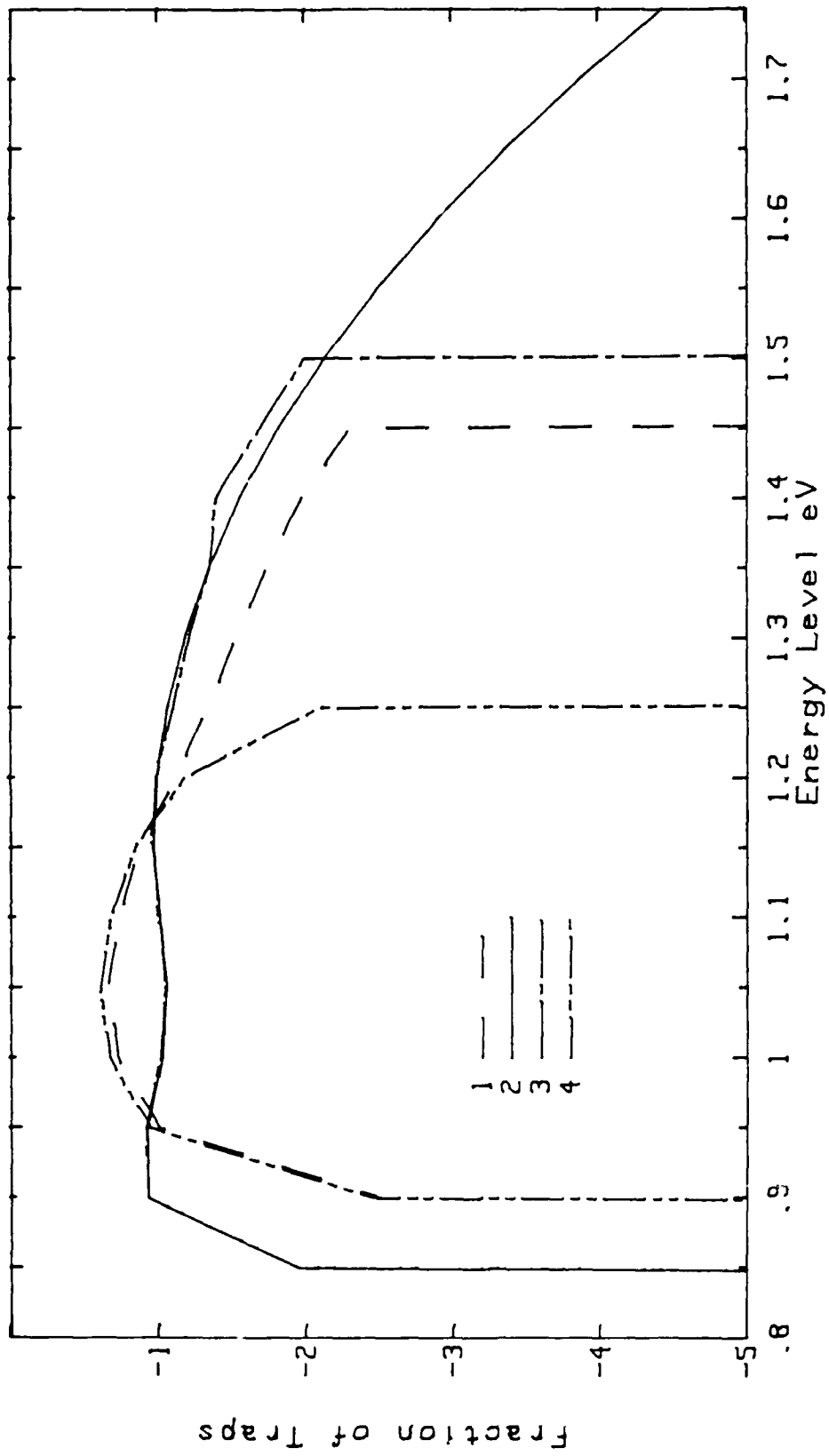


Figure 25. The energy distributions of the traps, on a log scale.

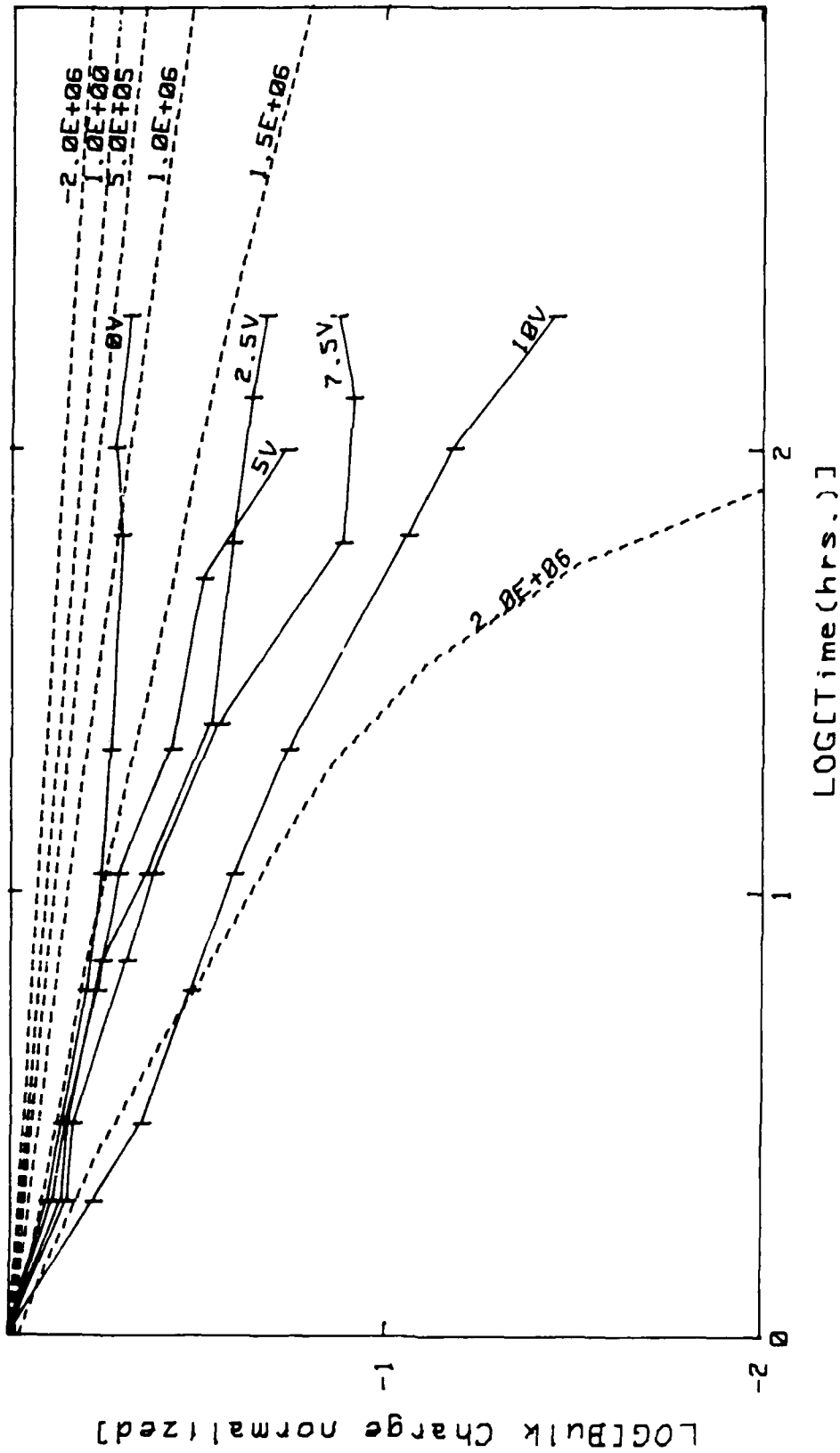


Figure 26. A comparison between the data from Schwank (Ref. 5) and computations using the ID model, made for a trap depth parameter of  $1E7 \text{ cm}^{-1}$ , using trap energy distribution #3, and temperature 375 K vs.  $100^{\circ}\text{C}$ .

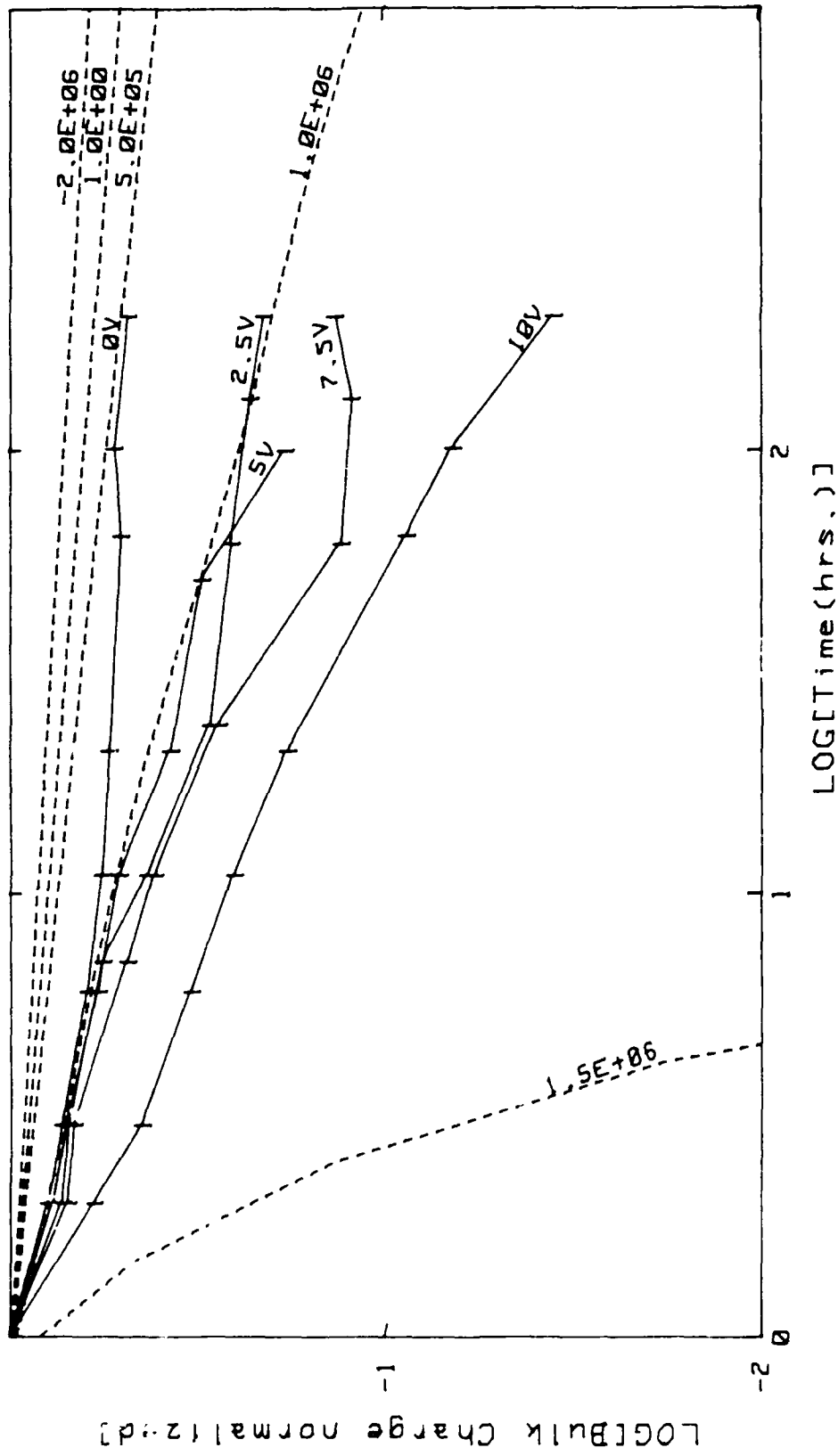


Figure 27. A comparison between the data from Schwank (Ref. 5) and computations using the 1D model, made for a trap depth parameter of  $1E7$  1/cm, using trap energy distribution #1, and temperature  $375$  K vs.  $100^{\circ}$ C.

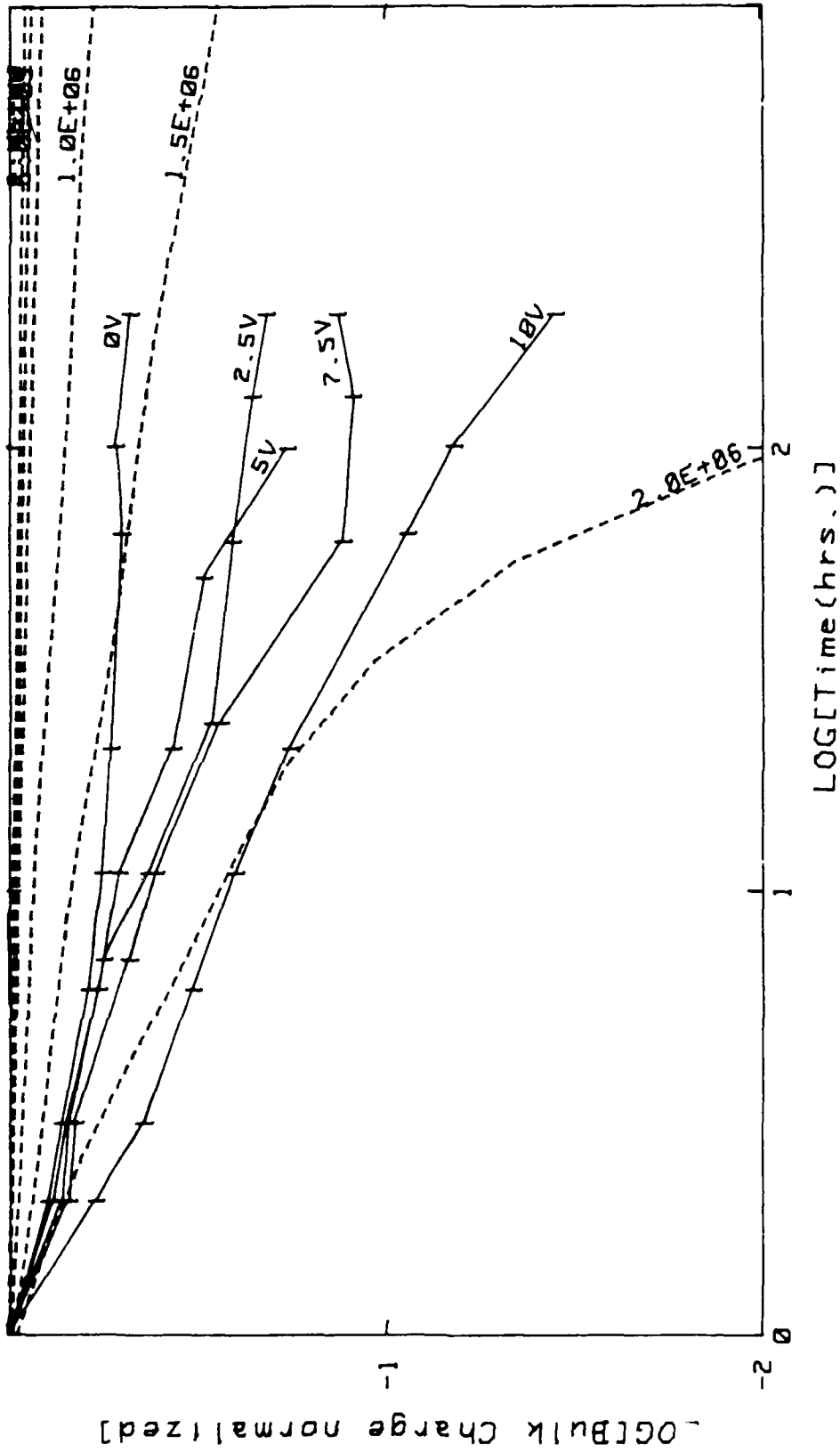


Figure 28. A comparison between the data from Schwank (Ref. 5) and computations using the 1D model, made for a trap depth parameter of  $2E6$  1/cm, using trap energy distribution #3, and temperature 375 K vs.  $100^{\circ}\text{C}$ .

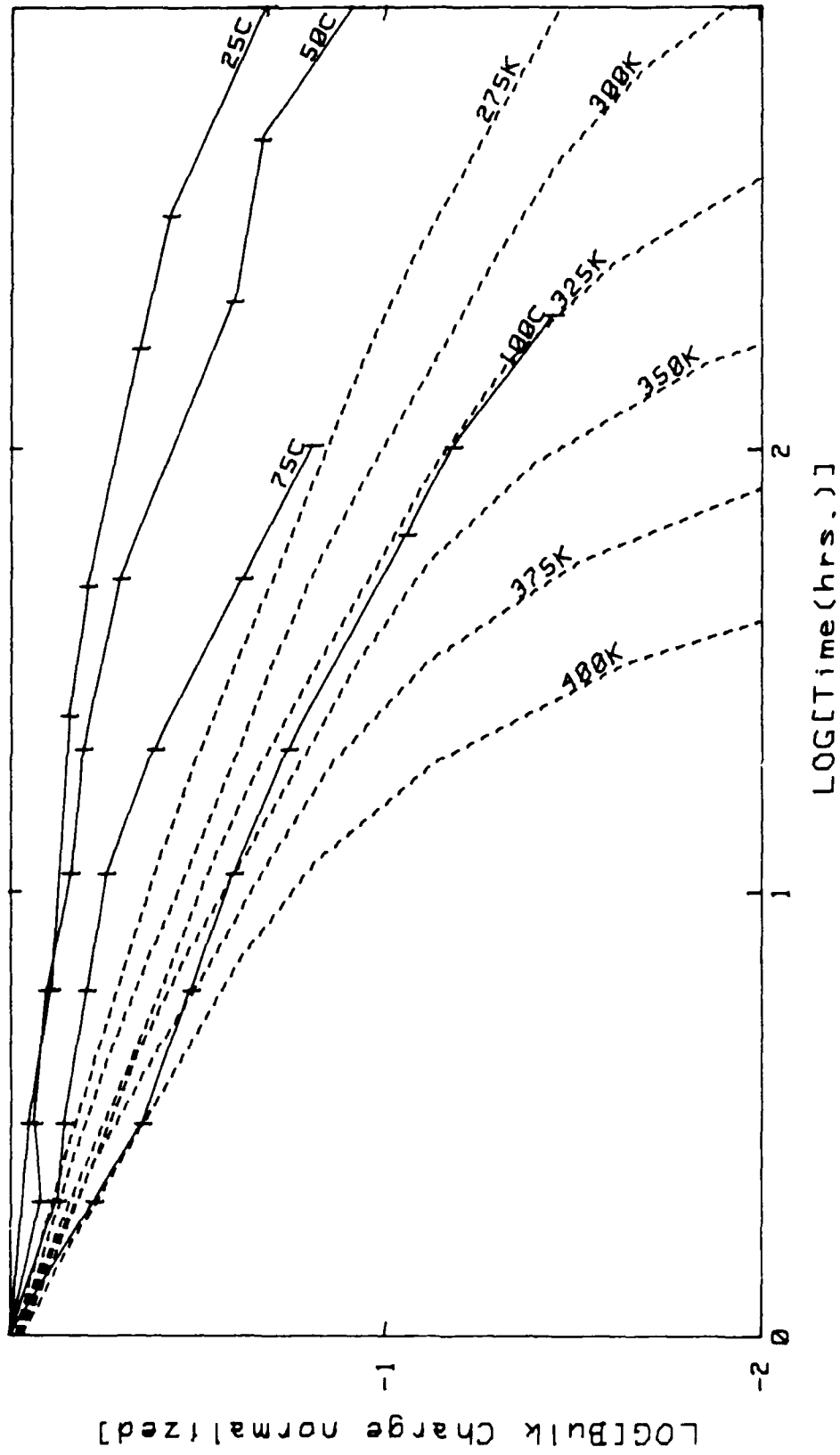


Figure 29. A comparison between the data from Schwank (Ref. 5) and computations using the ID model, made for a trap depth parameter of  $1E7$  1/cm, using trap energy distribution #3, and an electric field of  $2E6$  V/cm vs.  $10$  V across  $450$  Å.

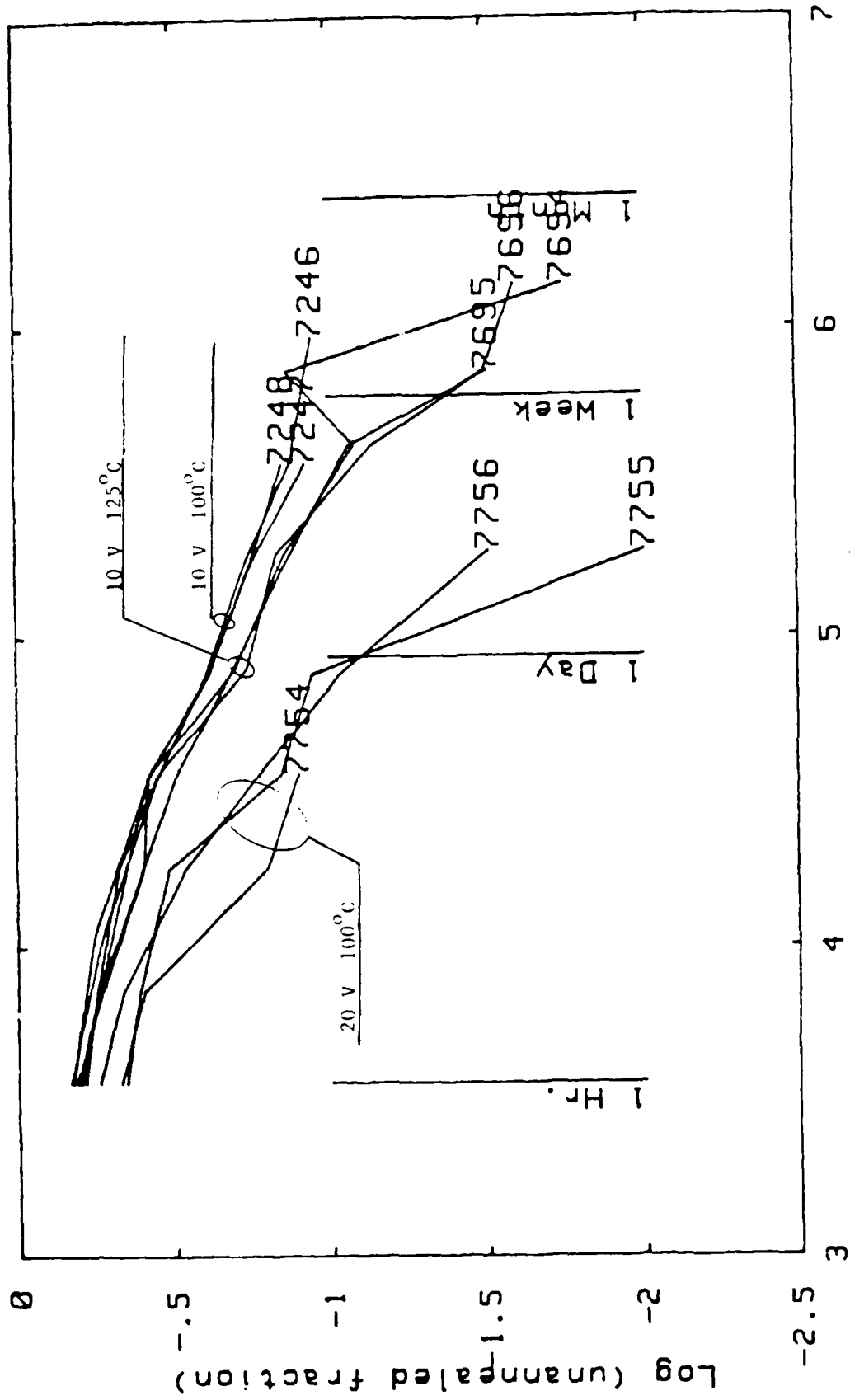


Figure 30. Additional data from Schwank (Ref. 23) adding annealing curves for 10V at 125°C and 20 V at 100°C.

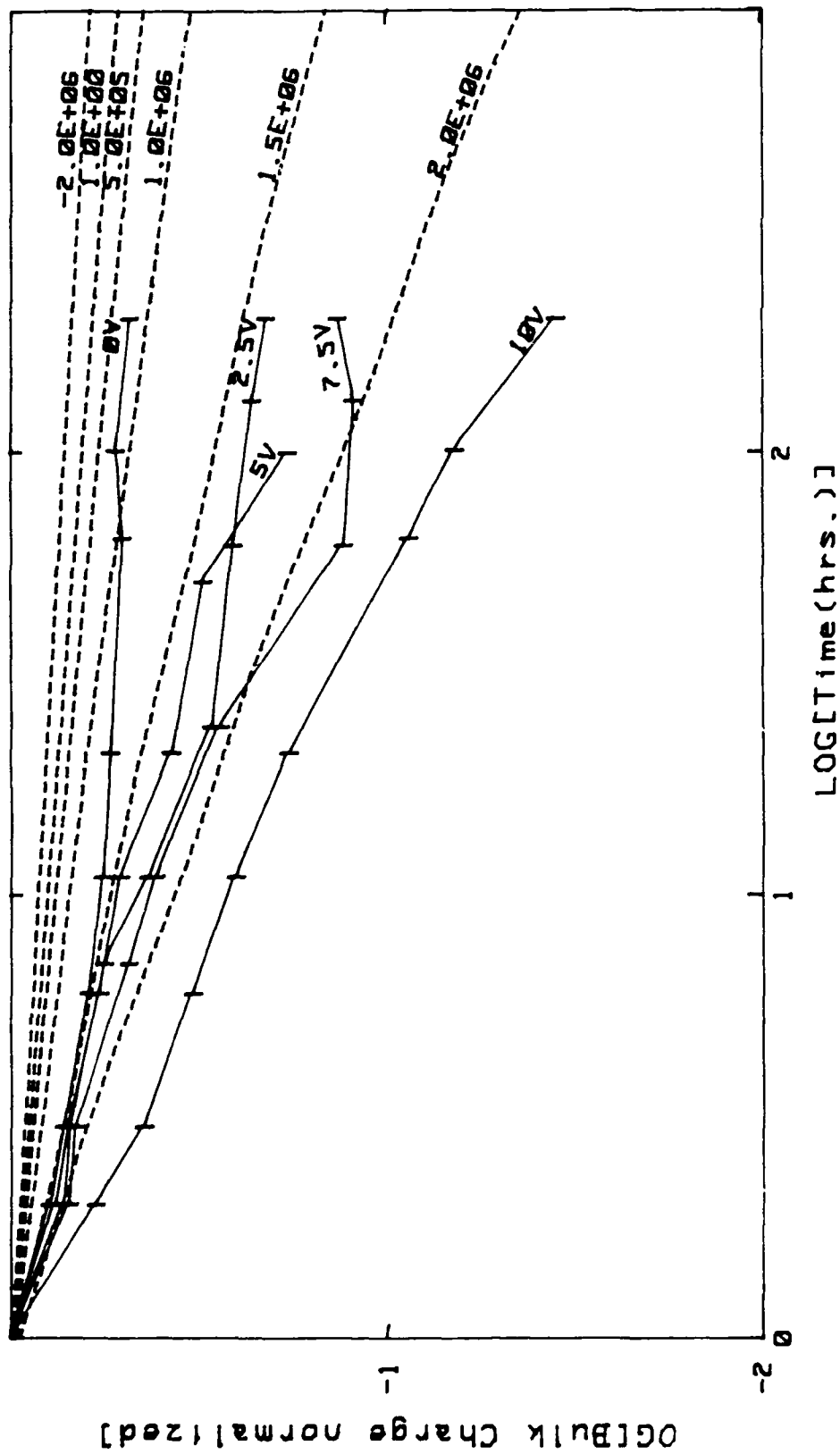


Figure 31. A comparison between the data from Schwank (Ref. 5) and computations using the ID model, made for a trap depth parameter of  $1.7 \text{ cm}^{-1}$ , using trap energy distribution #2, and temperature  $375 \text{ K}$  vs.  $100^\circ \text{C}$ .

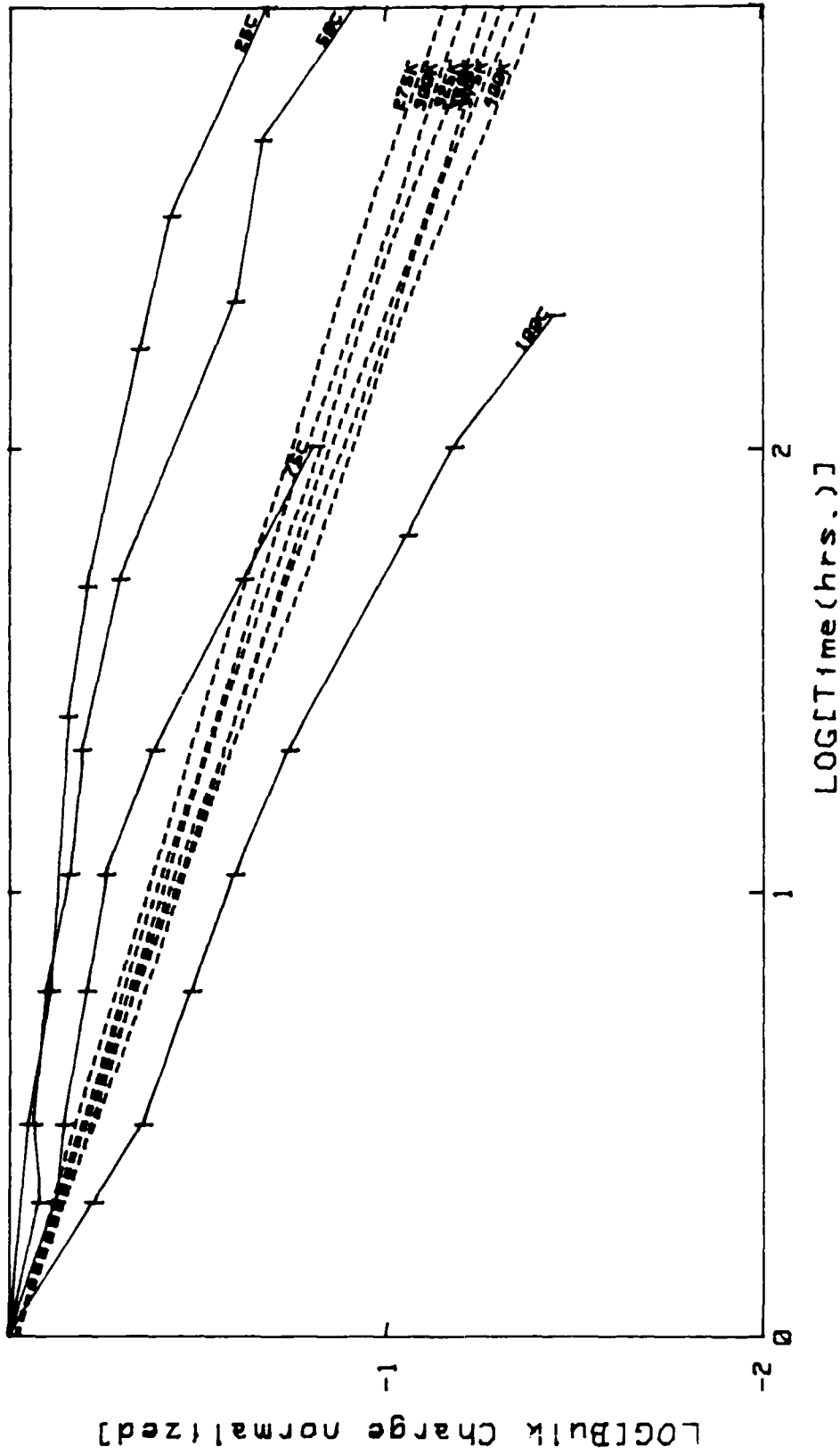


Figure 32. A comparison between the data from Schwank (Ref. 5) and computations using the 1D model, made for a trap depth parameter of  $1E7$  l/cm, using trap energy distribution #2, and an electric field of  $2E6$  V/cm vs.  $10$  V across  $450$  Å.

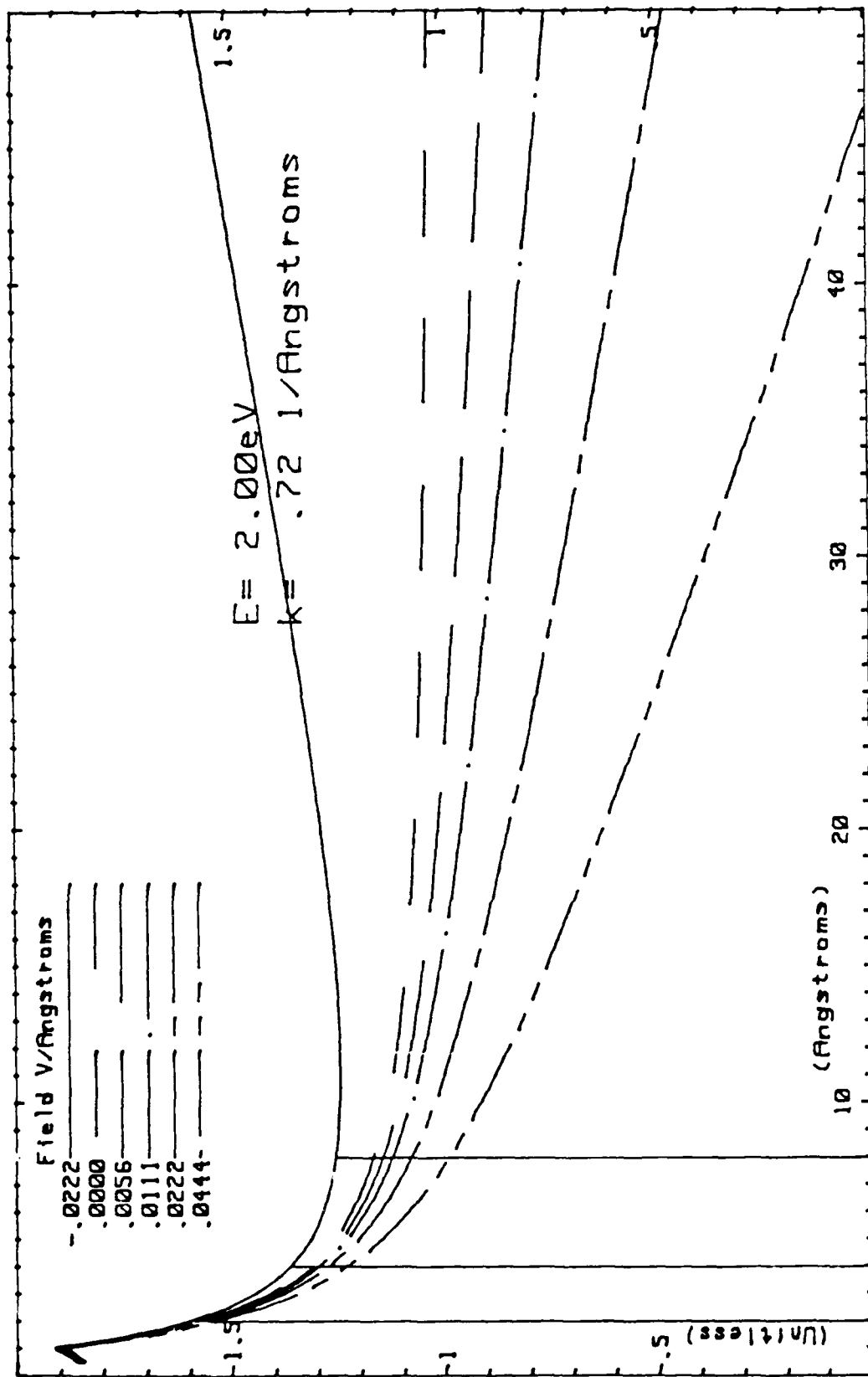


Figure 33. The tunneling barrier energy, for a trap energy of 2 eV, for the spherical well model with vertical lines at 2, 4 and 8 A to show the beginning of the barrier.

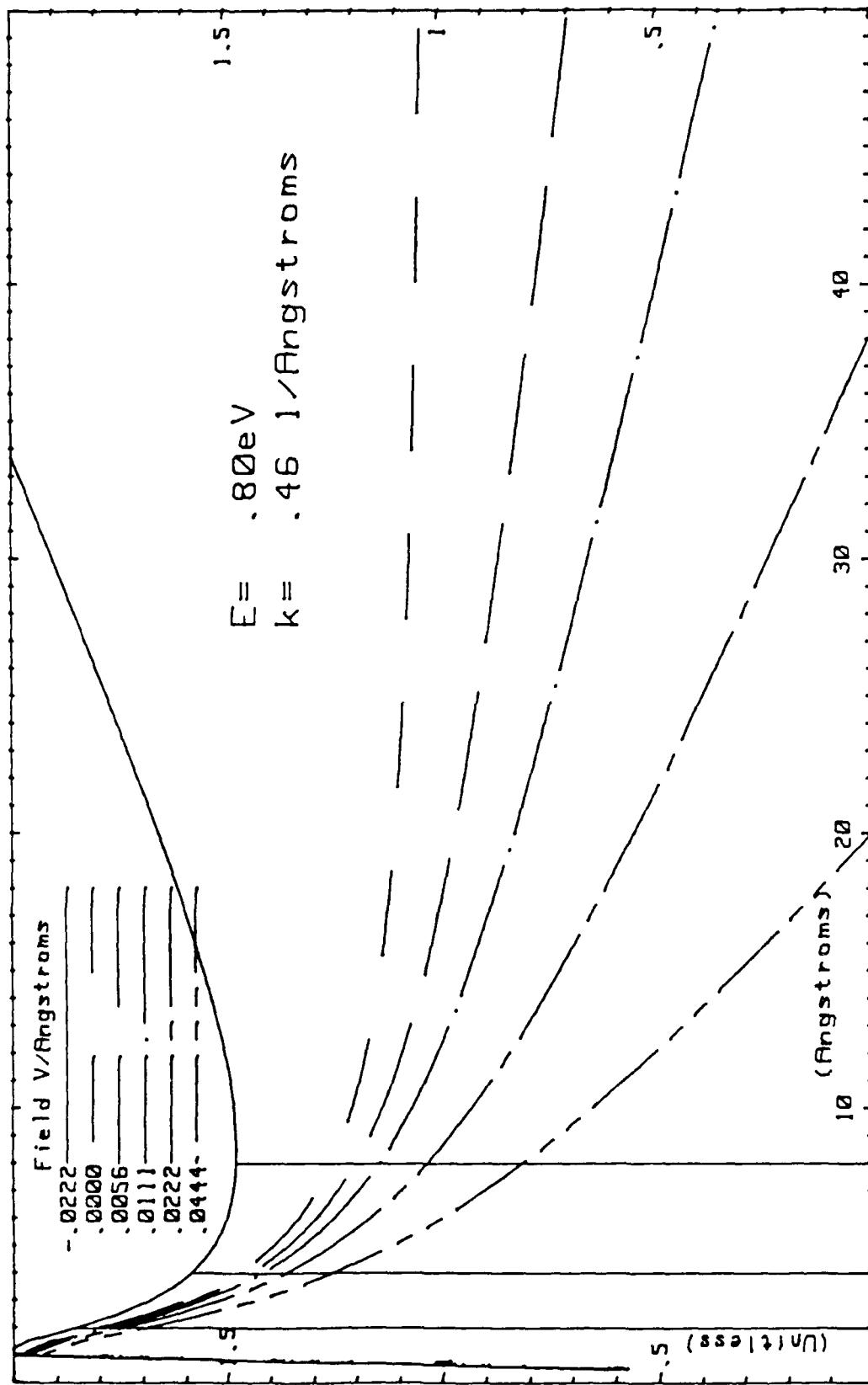


Figure 34. The tunneling barrier energy, for a trap energy of 0.8 eV, for the spherical well model with vertical lines at 2, 4 and 8 A to show the beginning of the barrier.

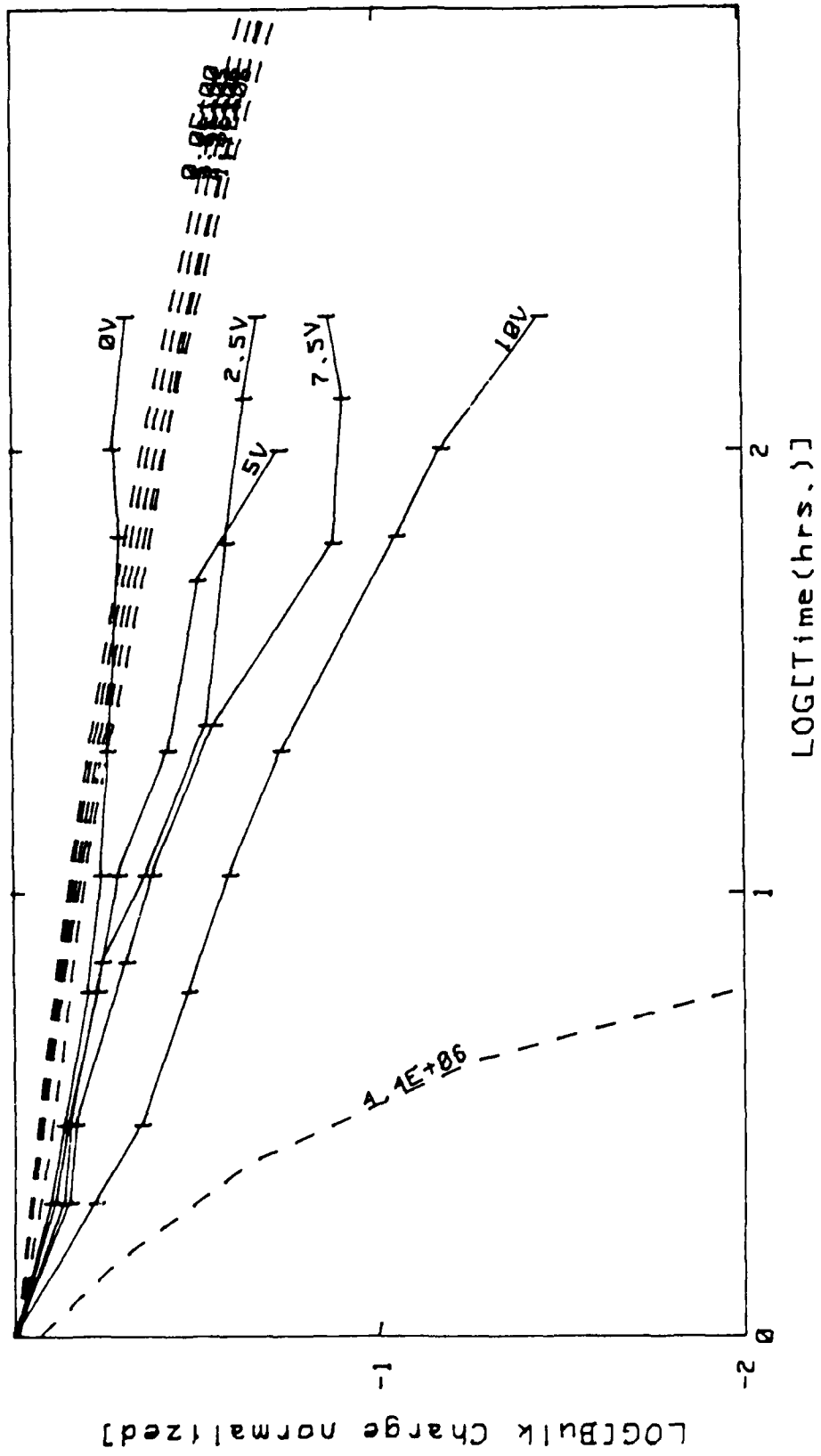


Figure 35. A comparison between the data from Schwank (Ref. 5) and computations using the spherical well model, radius 2 A and cross section 1E-16, made for a trap depth parameter of  $2E6 \text{ cm}^{-1}$ , using trap energy distribution #3, and temperature 375 K vs.  $100^\circ\text{C}$ .

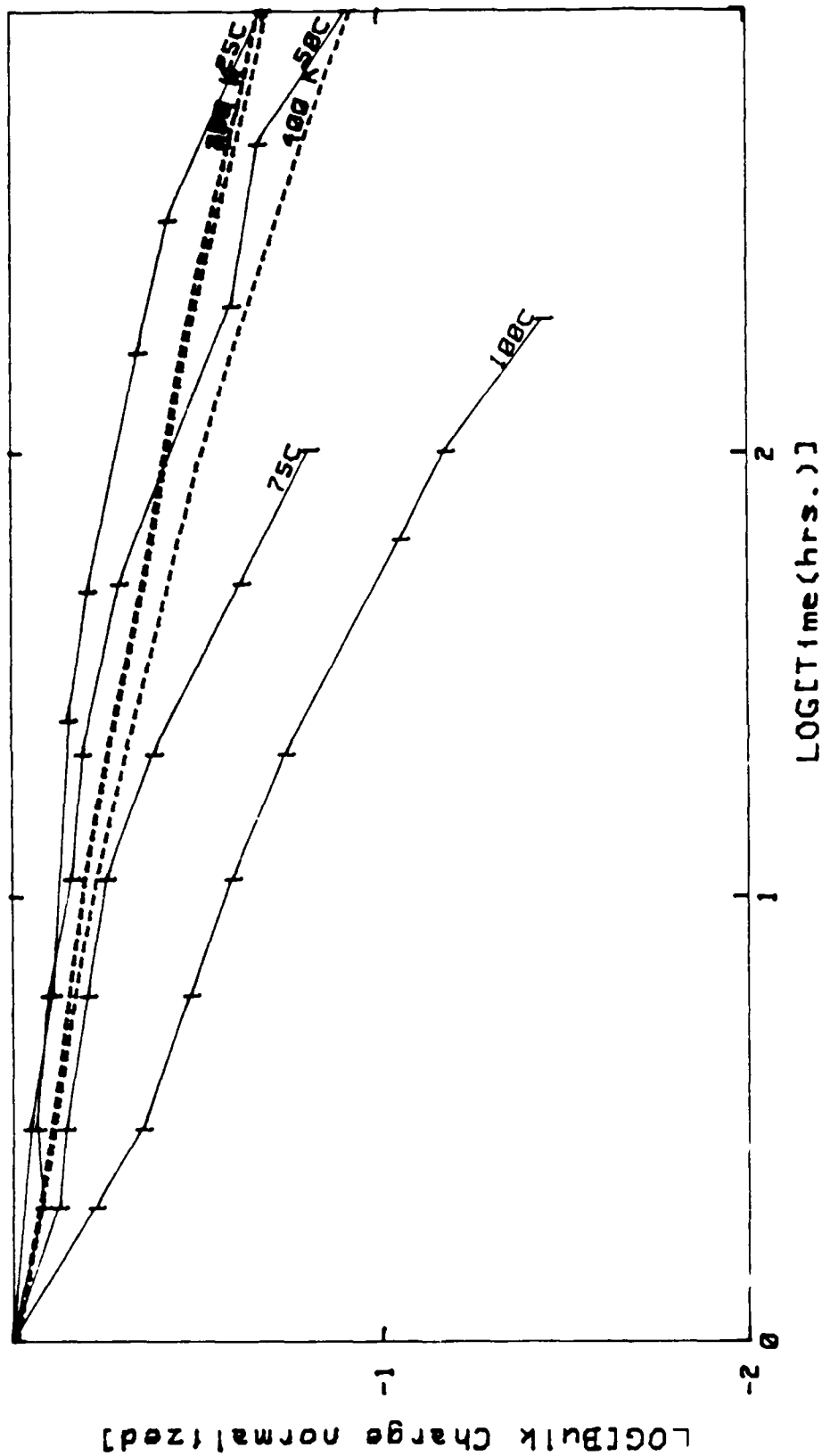


Figure 36. A comparison between the data from Schwank (Ref. 5) and computations using the spherical well model, radius 2 A and cross section 1E-16, model, made for a trap depth parameter of  $1E7 \text{ cm}^{-1}$ , using trap energy distribution #2, and an electric field of  $2E6 \text{ V/cm}$  vs.  $10 \text{ V}$  across  $450 \text{ \AA}$ .

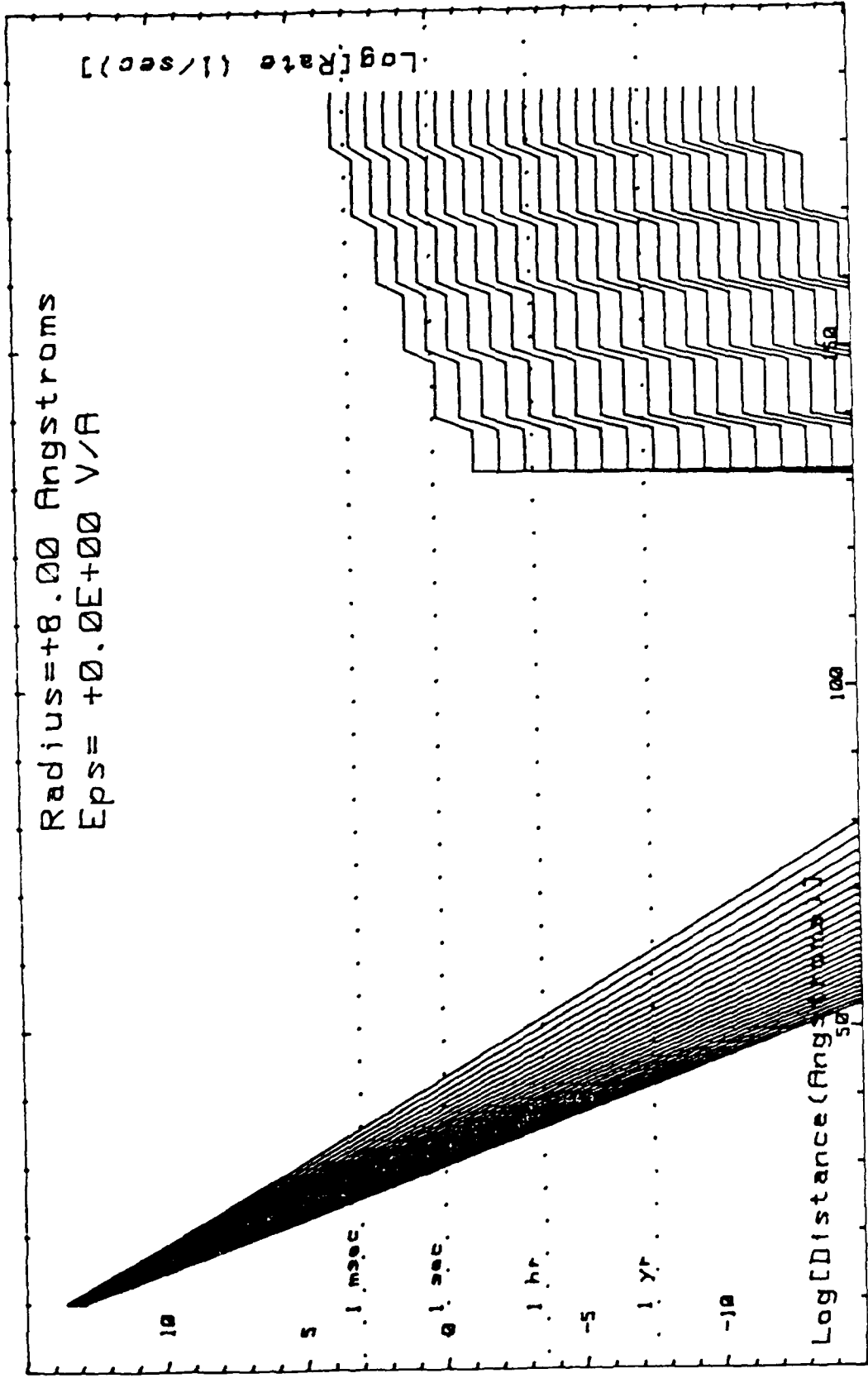


Figure 37. Partial detrapping rates for zero field.

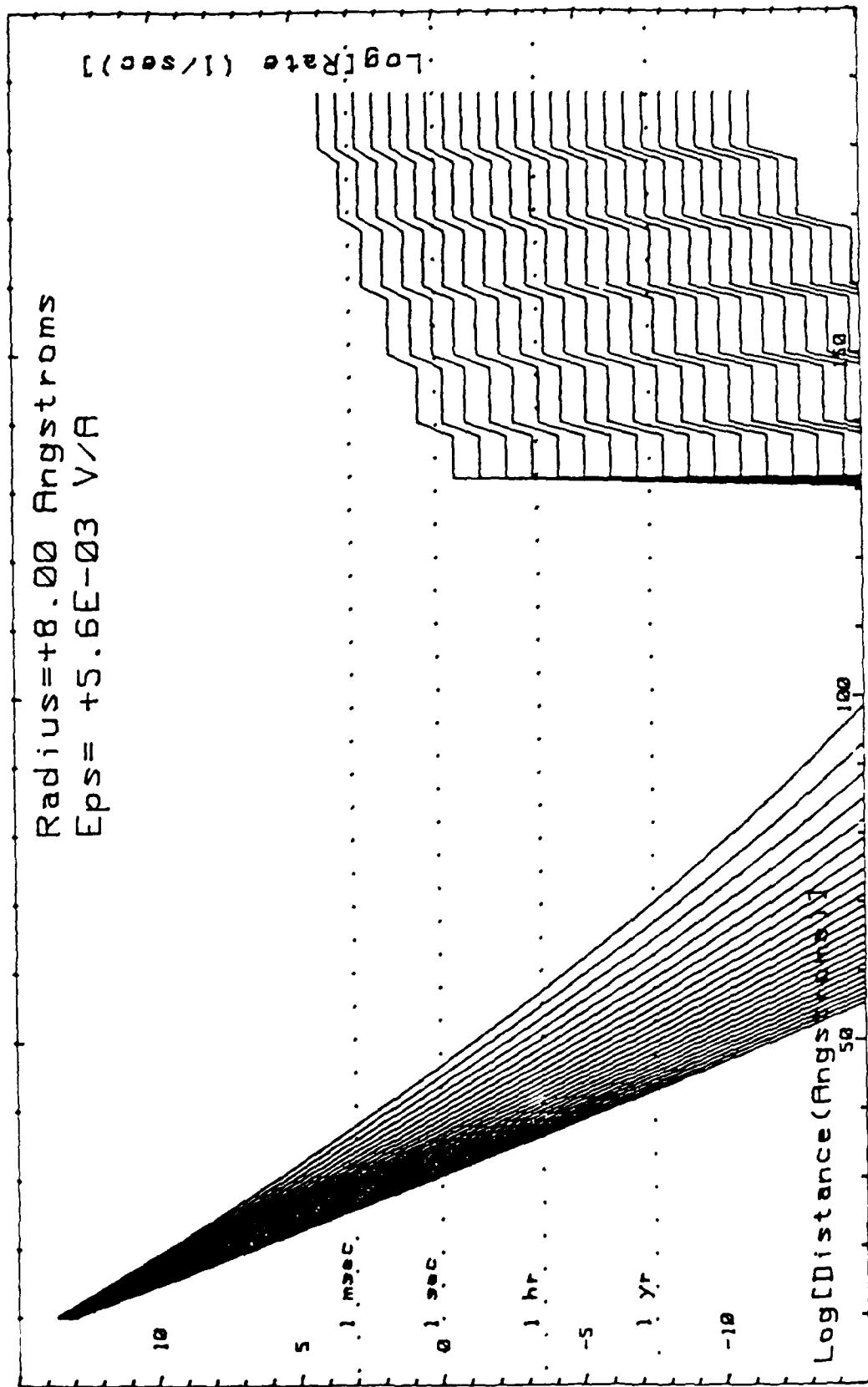


Figure 38. Partial detrapping rates for 2.5 V across 450 Å.

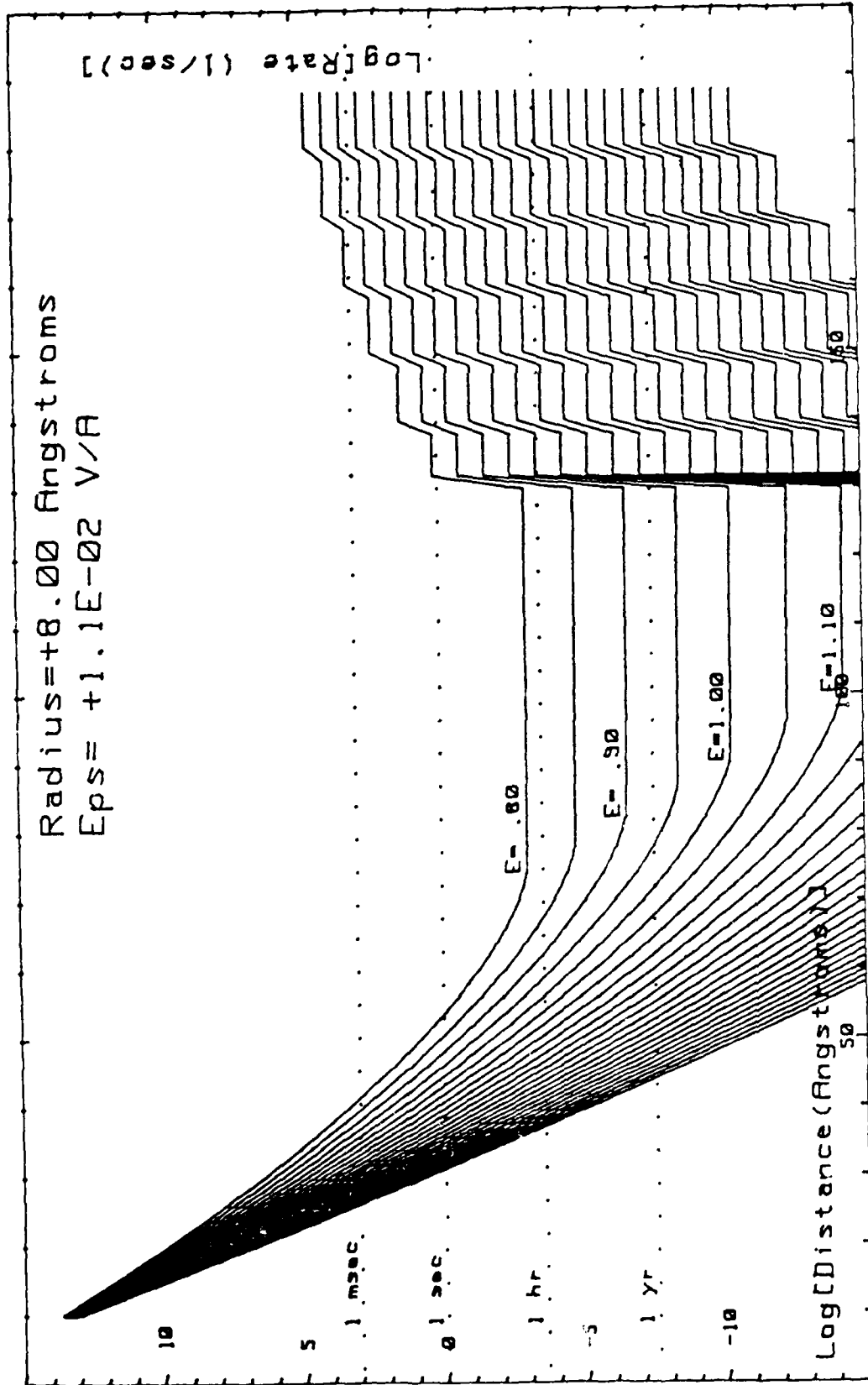


Figure 39. Partial detrapping rates for 5 V across 450 Å.

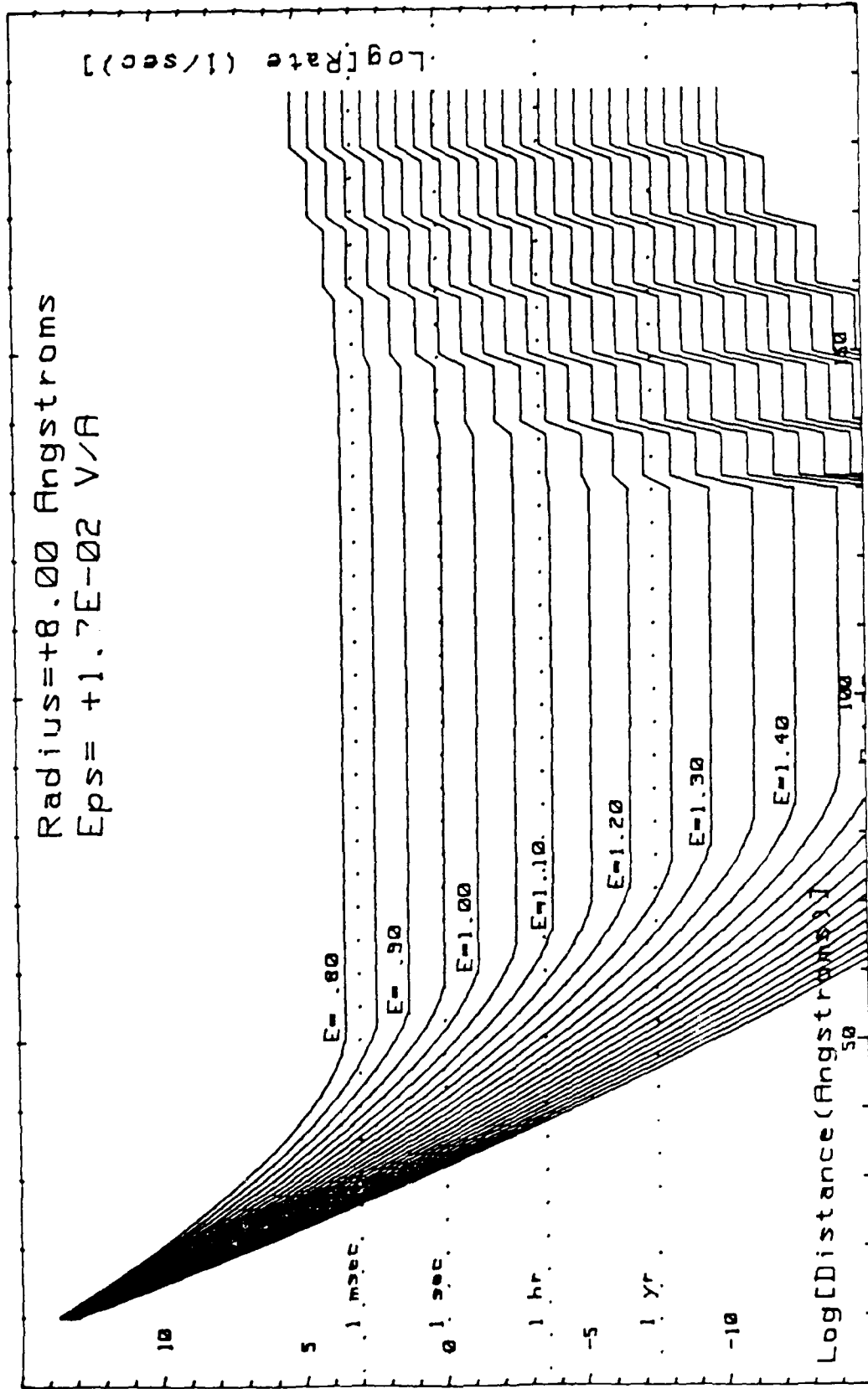


Figure 40. Partial detrapping rates for 7.5 V across 450 Å.

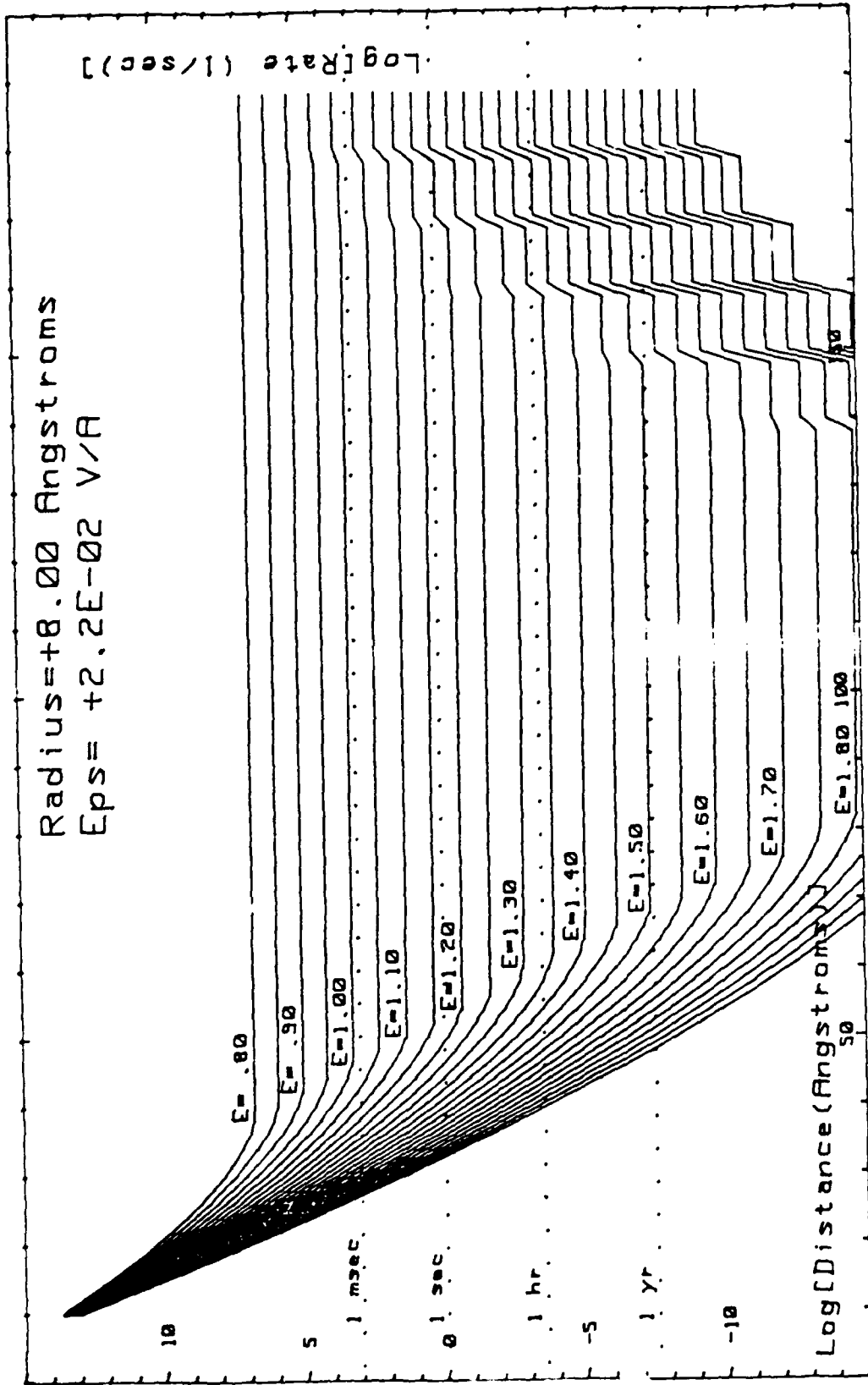


Figure 41. Partial detrapping rates for 10 V across 450 Å.

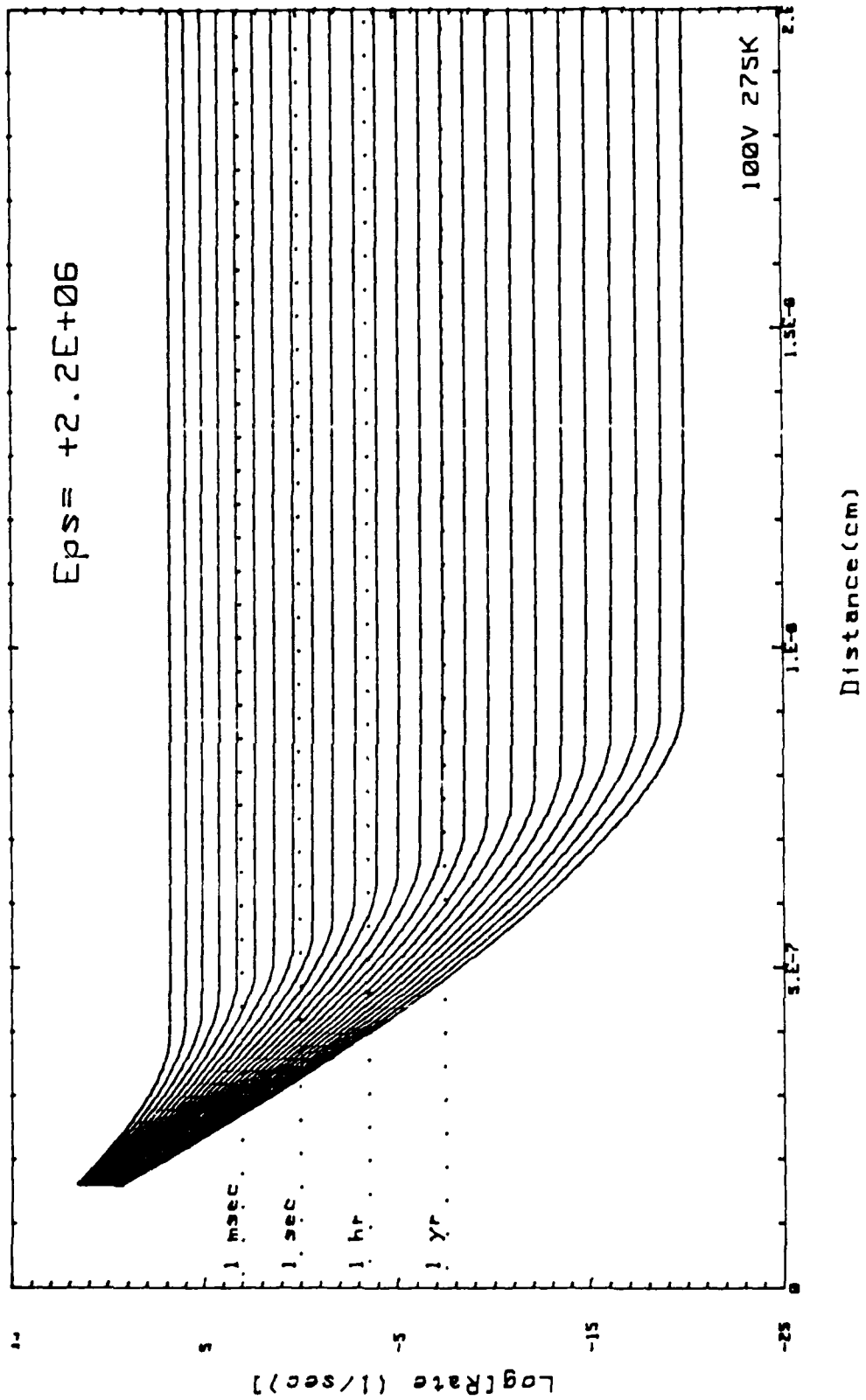


Figure 42. Detrapping rates for 10 V across  $450 \text{ \AA}$  at 275 K.

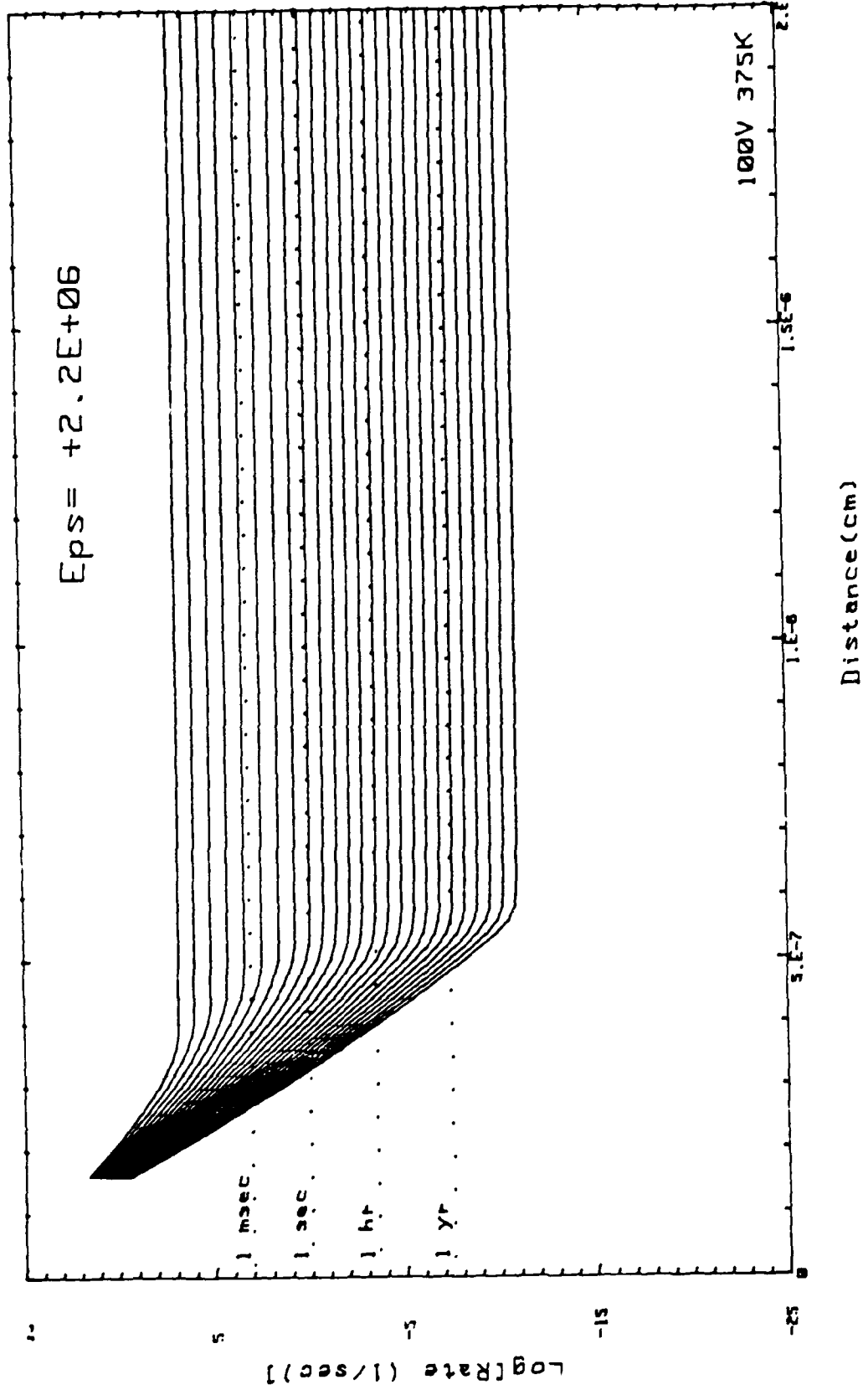


Figure 43. Detrapping rates for 10 V across 450 Å at 375 K.

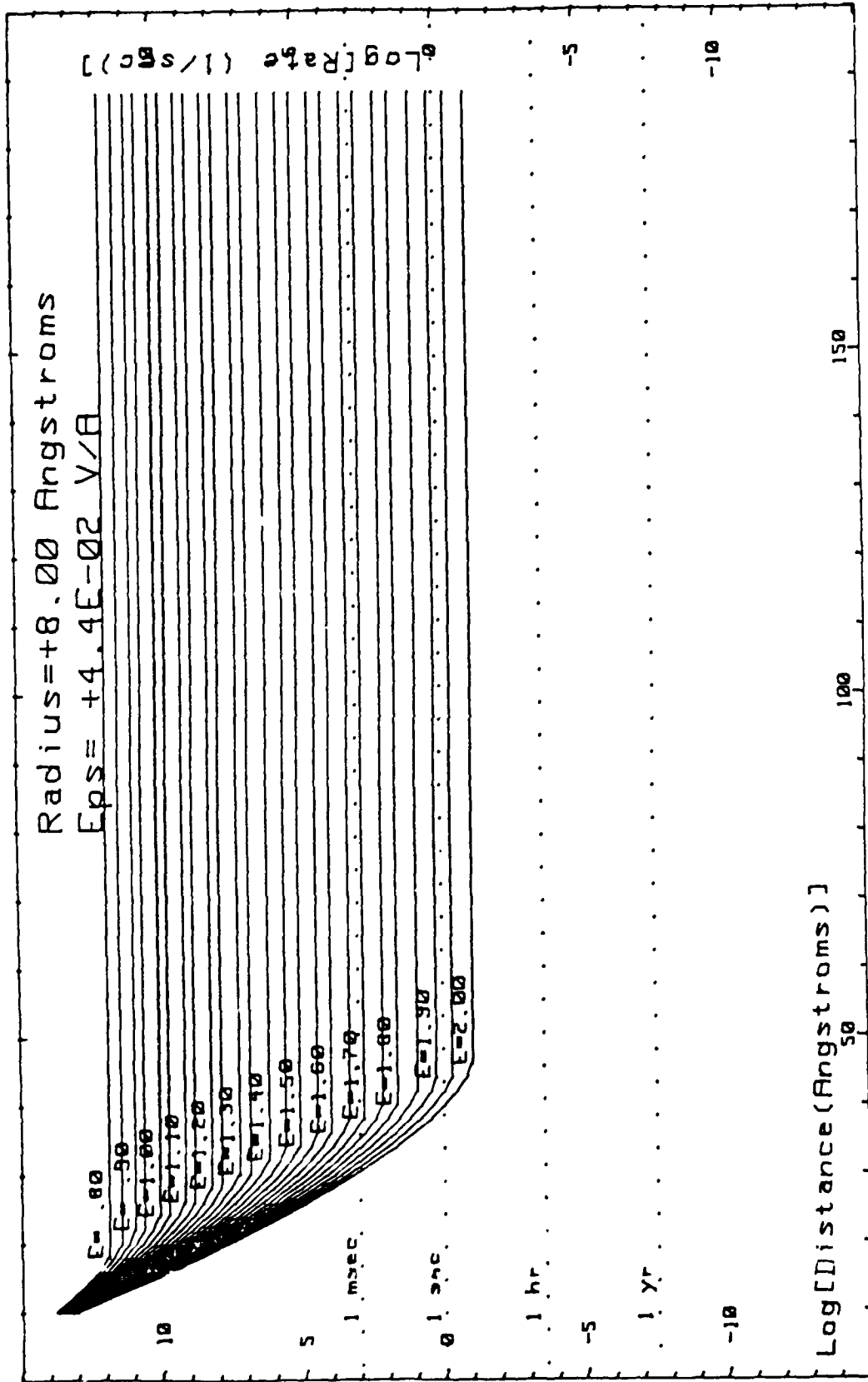


Figure 44. Detrapping rates for 20 V across 450 Å.

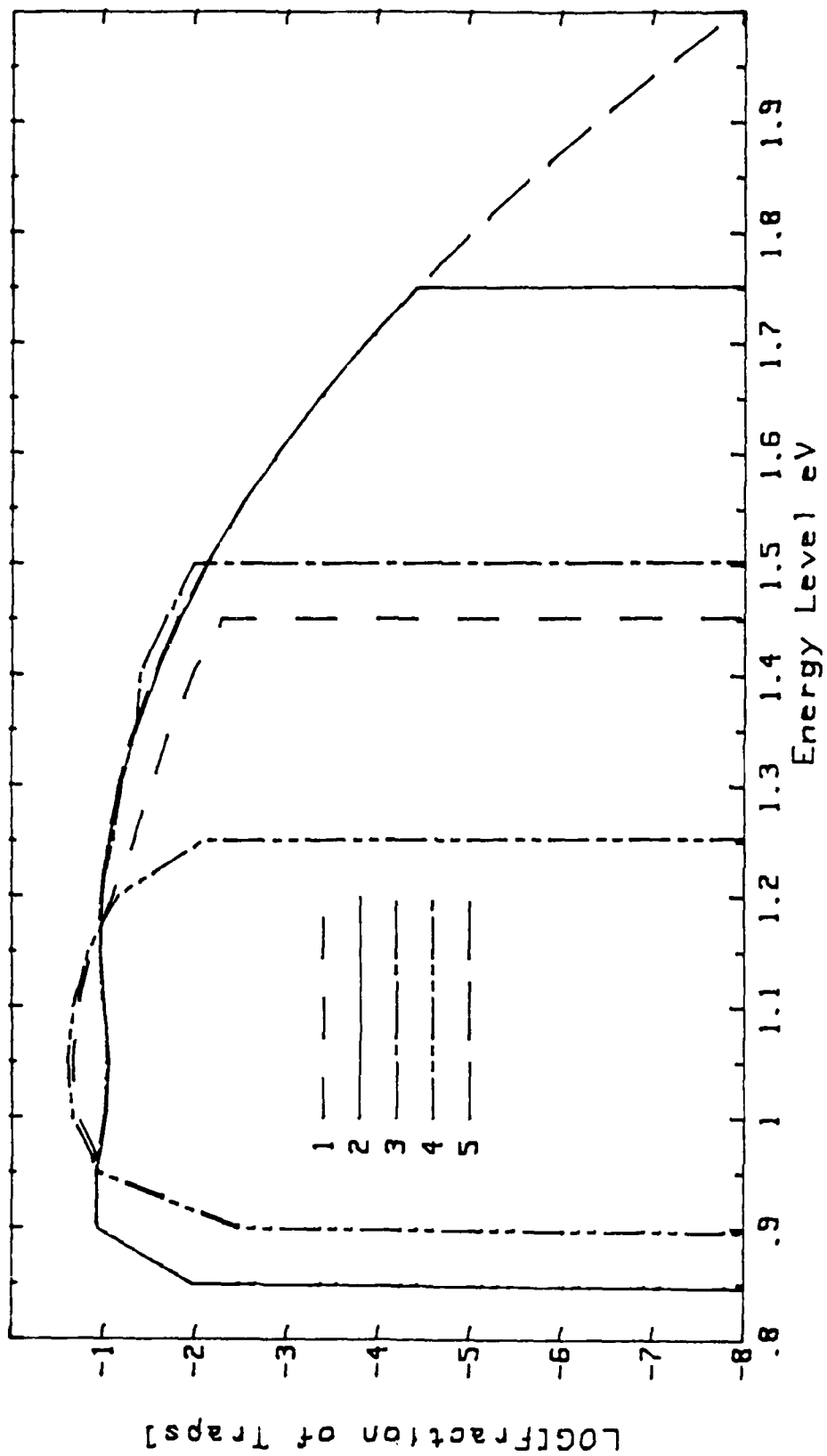


Figure 45. The energy distributions of the traps, on a log scale.

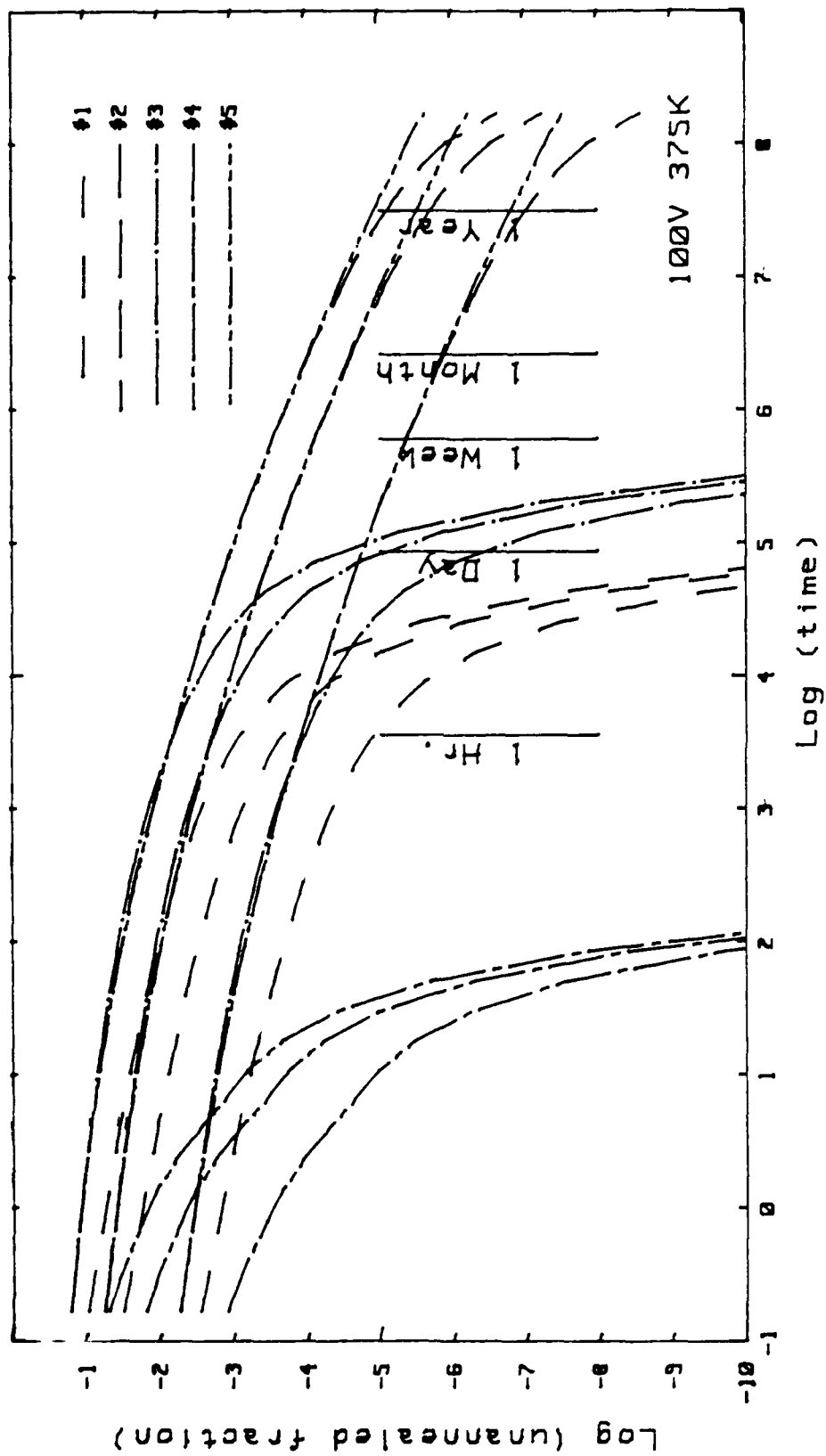


Figure 46. Spherical well annealing curves for: tunneling depth parameters,  $2E_6$ ,  $4.5E_6$  and  $1E7$ , the five trap energy distributions, 10 V across 450 A, and 375 K.

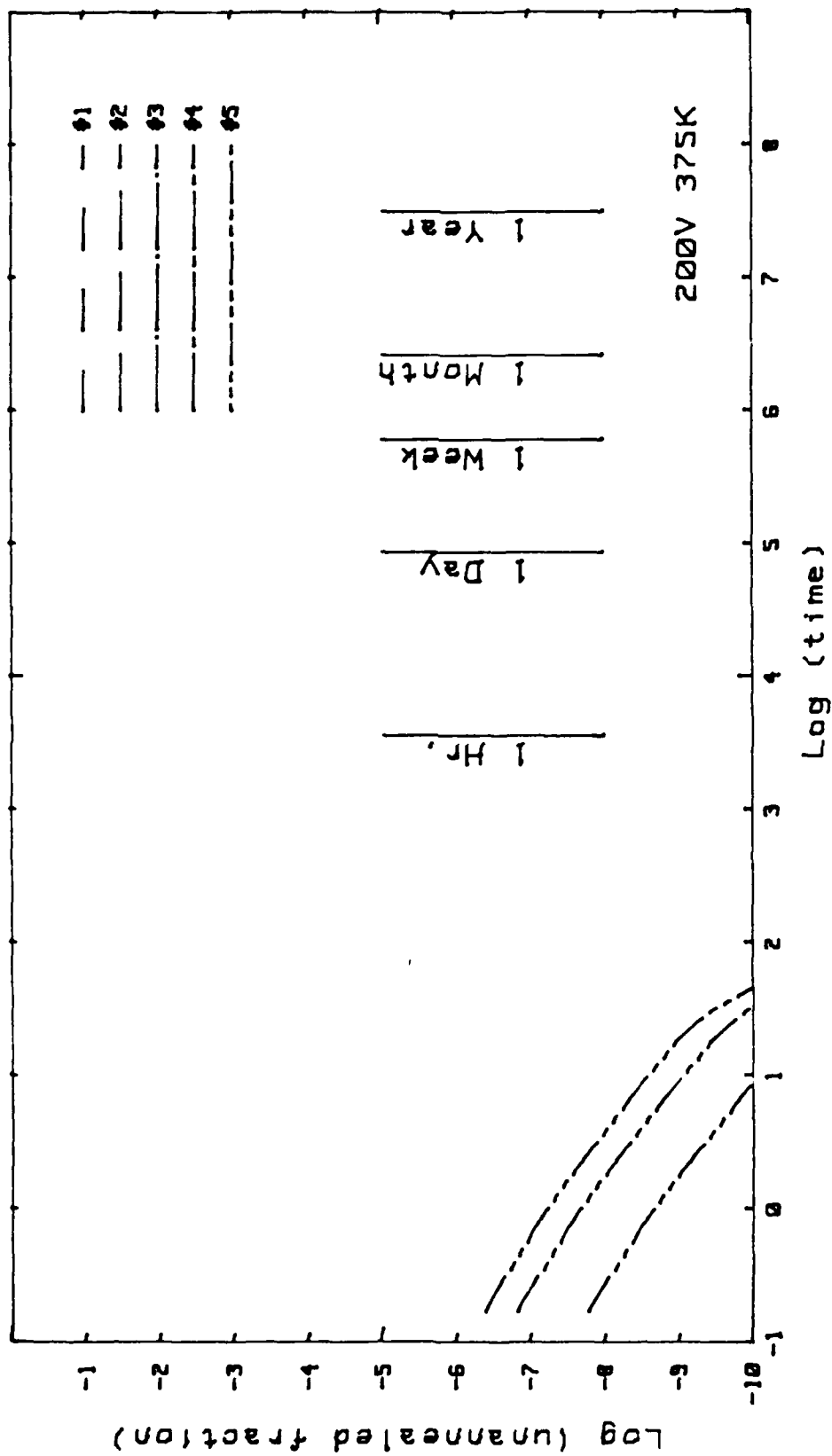


Figure 47. Spherical well annealing curves for: tunneling depth parameters, 2E6, 4.5E6 and 1E7, the five trap energy distributions, 20 V across 450 A, and 375 K.

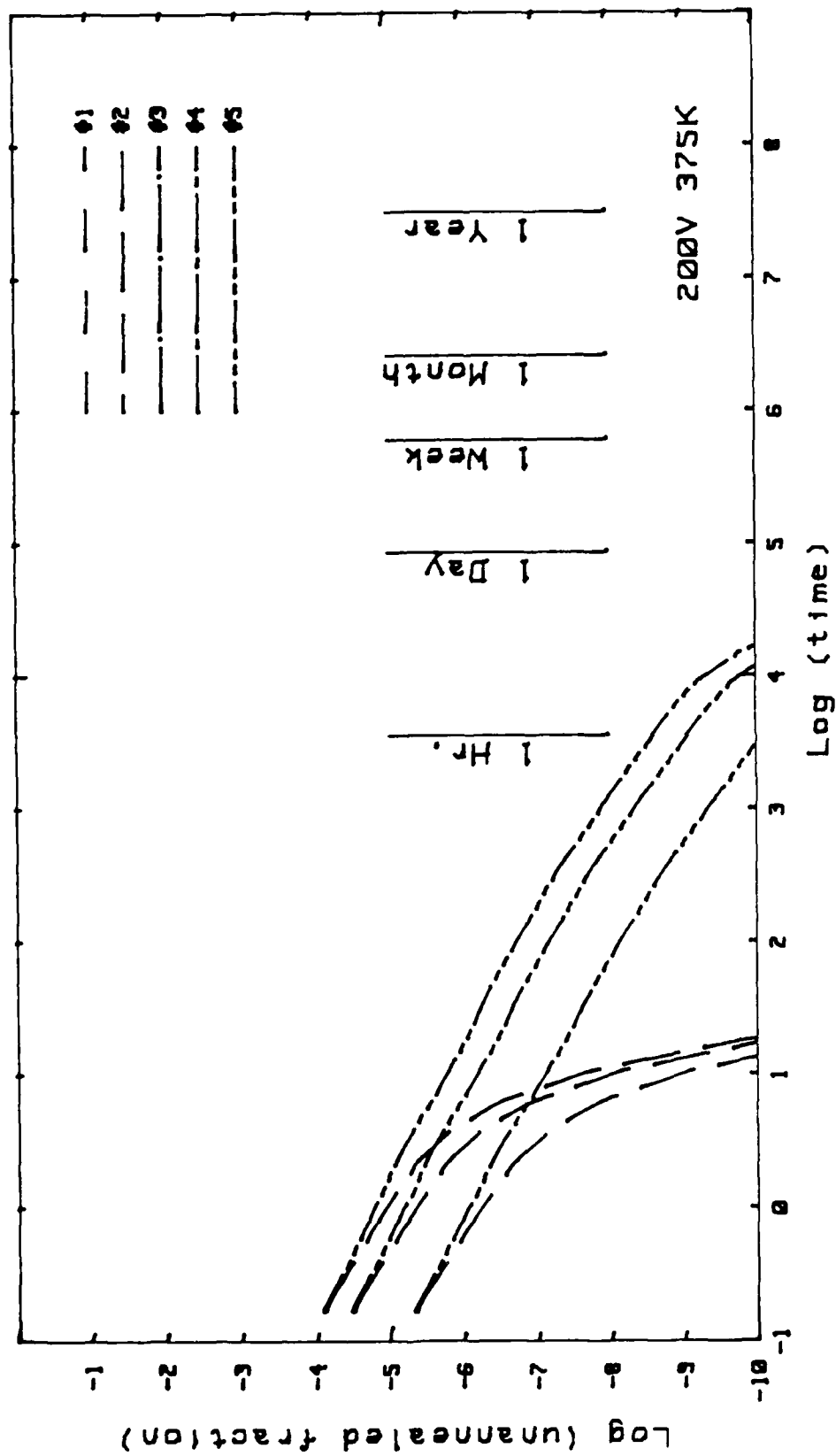


Figure 48. Spherical well annealing curves for: tunneling depth parameters, 2E6, 4.5E6 and 1E7, the five trap energy distributions, 20 V across 450 A, and 375 K but at radius 2 A and capture cross section 1E-16.

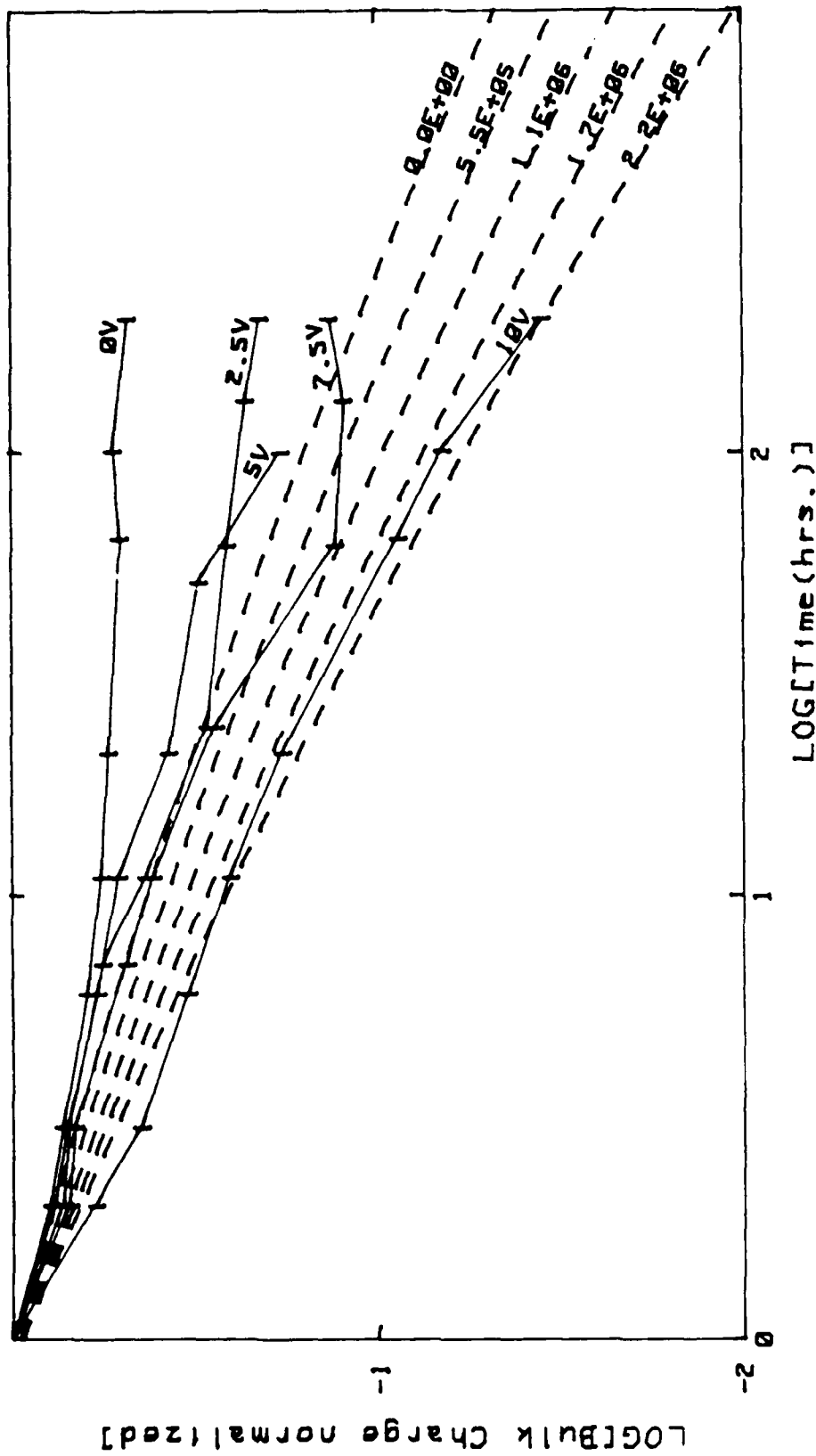


Figure 49. A comparison between the data from Schwank (Ref. 5) and computations using the spherical well model, radius 8 A and cross section  $7E-14$ , made for a trap depth parameter of  $1E7 \text{ cm}^{-1}$ , using trap energy distribution #5, and temperature 375 K vs.  $100^\circ\text{C}$ .

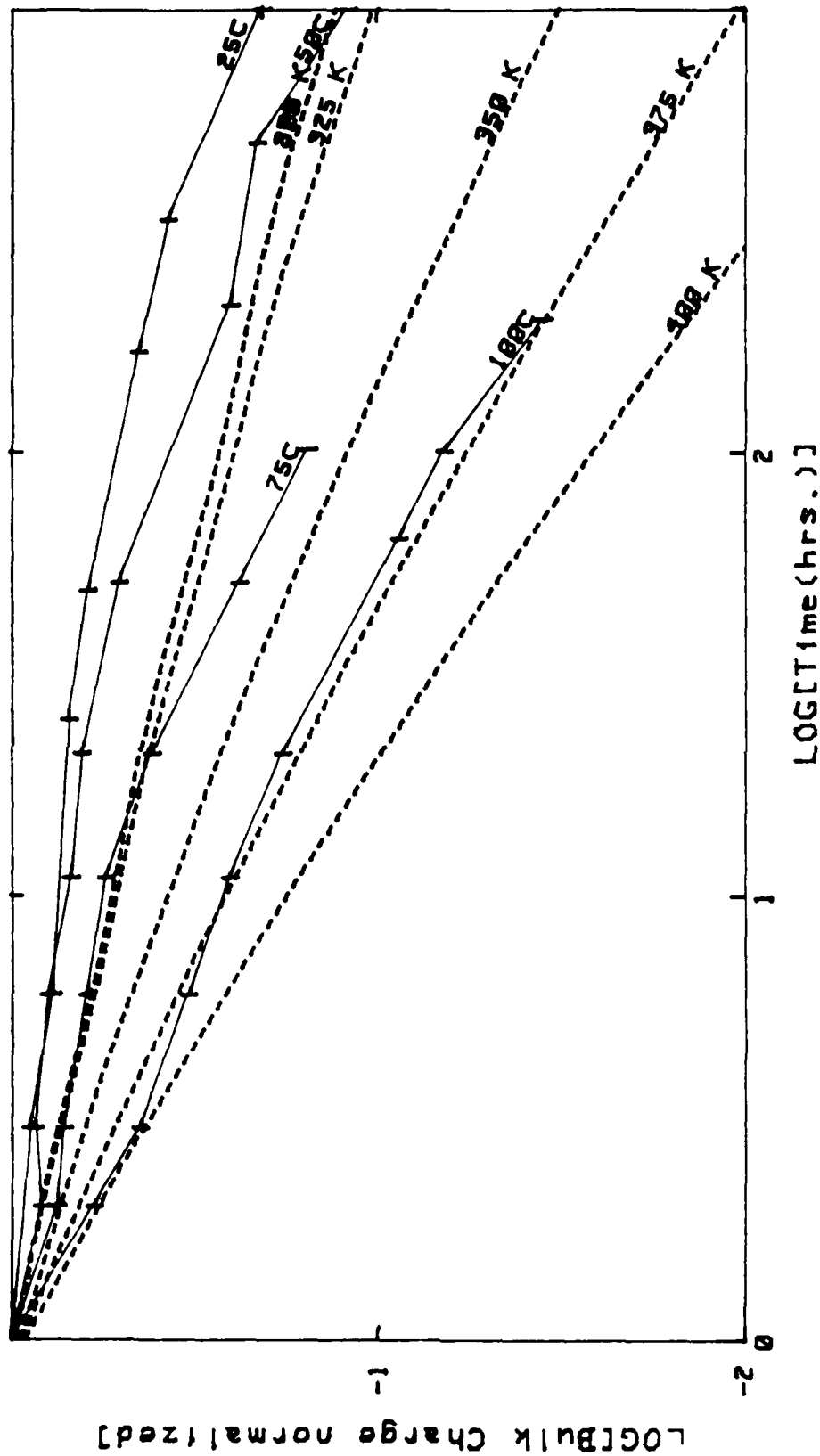


Figure 50. A comparison between the data from Schwank (Ref. 5) and computations using the spherical well model, radius 2 A and cross section IE-16, model, made for a trap depth parameter of  $1E7 \text{ cm}^{-1}$ , using trap energy distribution #5, and an electric field of 10 V across 450 Å.

## REFERENCES

1. M. Simons, H. L. Hughes "Determine the Energy Distribution of Pulse-Radiation-Induced Charge in MOS Structures from Rapid Annealing" Summaries of Papers, IEEE Annual Conference on Nuclear and Space Radiation Effects, Seattle, July 24-27, 1972; pp211-214
2. R. J. Maier "A Model for the Discharge of Radiation Induced Space charge" Summaries of Papers, IEEE Annual Conference on Nuclear and Space Radiation Effects, Seattle, July 24-27, 1972; pp215-218
3. H. E. Boesch Jr., F. B. McLean, J. M. McGarrity, and G. A. Ausman Jr. "Hole Transport and Charge Relaxation in Irradiated SiO<sub>2</sub> MOS Capacitors" IEEE Trans. NS-22, pp2163
4. H. H. Sander and B. L. Gregory "Unified Model of Damage Annealing in CMOS, from Freeze-In to Transient Annealing" IEEE Trans. NS-22, pp2157
5. J. R. Schwank et. al. "Physical Mechanisms Contributing to Device 'Rebound'" IEEE Trans. NS-31, pp1434
6. F. B. McLean and G. A. Ausman Jr. "Simple Approximate Solutions to Continuous-Time Random-Walk Transport" Phys. Rev. B. vol.15 pp1052
7. H. Scher and E. W. Montroll "Anomalous Transit-Time Dispersion in Amorphous Solids" Phys. Rev. B. Vol.12 pp2455

8. A. K. Jonscher Dielectric Relaxation in Solids Chelsa Dielectrics Press, London 1983
9. F. Vivaldi, G. Casati, and I. Guarneri "Origin of Long-Time Tails in Strongly Chaotic Systems" Phys. Rev. Let. Vol.51 pp.727
10. H. van Beijeren " Transport Properties of Stochastic Lorentz Models" Rev. Mod. Phys. Vol.54,pp195
11. V. Danchenko, P. H. Fang, and S. S. Brashears "Activation Energies of Thermal Annealing of Radiation-Induced Damage in n- and p-Channels of CMOS Integrated Circuits" IEEE Trans. NS-27, pp 1658.
12. Neamen, D. A. Modeling of MOS radiation and post irradiation effects" IEEE Trans NS-31 Dec 84 1439-1443.
13. P. S. Winokur, K. G. Kerris, and L. Harper "Predicting CMOS Inverter Response in Nuclear and Space Environments" IEEE Trans. NS-30 (Dec.1983) pp4326
14. P. M. Lenahan and P. V. Dressendorfer "Hole Traps and Trivalent Silicon Centers in Metal/Oxide/Silicon Devices" J. Appl. Phys. Vol. 55 pp3495
15. R. C. Hughes and D. Emin "Small Polaron Formation and Motion of Holes in  $\alpha$ -SiO<sub>2</sub>" The physics of SiO<sub>2</sub> and its Interfaces Pergamon Press (1978) pp14

16. K. H. Zaininger "Irradiation of MIS Capacitors with High Energy Electrons" IEEE Trans. NS-13 pp237 (Dec.1966)
17. R.J. Maier "Silicon Lattice Constraints on The Structure of Interface-States" IEEE Trans. NS-23, pp1558 (Dec.1976)
18. T. R. Oldham, A. J. Lelis, and F. B. McLean "Spatial Dependence of Trapped Holes Determined from Tunneling Analysis and Measured Annealing" IEEE Trans. NS-33 pp1203 (Dec.1986)
19. F. B. McLean "A Direct Tunneling Model of Charge Transfer at the Insulator-Semiconductor Interface in MIS Devices" HDL-TR-1765 available DTIC ADA034436
20. C. Kittel Solid State Physics John Wiley & Son 2nd Edition 1960 see pp 355-356
21. L. D. Landau and E. M. Lifshitz Quantum Mechanics Pergamon Press 3rd revised edition 1977
22. D. Bohm Quantum Theory Prentice-Hall New York 1951
23. J. R. Schwank private communication
24. P. H. Fang; private communication

25. D. V. Lang, "Deep Level Transient Spectroscopy: A New Method to Characterize Traps in Semiconductors" J. Appl. Phys., vol. 47 pp1131-1135 1974